SPECTROSCOPIC CHARACTERIZATION OF MBE GROWN AlGaN/GaN HETEROSTRUCTURES

By

DIPANKAR JANA

Enrolment No: PHYS03201104011

Raja Ramanna Centre for Advanced Technology

Indore-452013, India

A thesis submitted to the

Board of Studies in Physical Sciences

In partial fulfillment of requirements

for the Degree of

DOCTOR OF PHILOSOPHY

of

HOMI BHABHA NATIONAL INSTITUTE

August, 2017

Homi Bhabha National Institute[1]

Recommendations of the Viva Voce Committee

As members of the Viva Voce Committee, we certify that we have read the dissertation prepared by Dipankar Jana entitled "Spectroscopic Characterization of MBE grown AlGaN/GaN Heterostructures" and recommend that it may be accepted as fulfilling the thesis requirement for the award of Degree of Doctor of Philosophy.

Chairman – Prof. Rama Chari	**Date:** 23.3.18
Guide / Convener – Prof. T. K. Sharma	**Date:** 23.3.18
Examiner- Prof. V. Venkataraman	**Date:** 23.3.18
Member 1- Prof. S. M. Gupta	**Date:** 23.3.18
Member 2- Prof. Tapas Ganguli	**Date:** 23-3-2018
Member 3- Prof. M. H. Modi	**Date:** 23.3.18
Member 4- Prof. M. K. Chattopadhyay	**Date:** 23/03/2018
External Member - Prof. Sandip Ghosh	**Date:** 23/3/2018

Final approval and acceptance of this thesis is contingent upon the candidate's submission of the final copies of the thesis to HBNI.

I hereby certify that I have read this thesis prepared under my direction and recommend that it may be accepted as fulfilling the thesis requirement.

Date: 23/03/2018

Place: Indore

T. K. Sharma

[1] This page is to be included only for final submission after successful completion of viva voce.

STATEMENT BY AUTHOR

This dissertation has been submitted in partial fulfillment of requirements for an advanced degree at Homi Bhabha National Institute (HBNI) and is deposited in the Library to be made available to borrowers under rules of the HBNI.

Brief quotations from this dissertation are allowable without special permission, provided that accurate acknowledgement of source is made. Requests for permission for extended quotation from or reproduction of this manuscript in whole or in part may be granted by the Competent Authority of HBNI when in his or her judgment the proposed use of the material is in the interests of scholarship. In all other instances, however, permission must be obtained from the author.

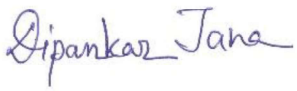

Dipankar Jana

DECLARATION

I, hereby declare that the investigation presented in the thesis has been carried out by me. The work is original and has not been submitted earlier as a whole or in part for a degree / diploma at this or any other Institution / University.

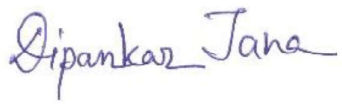

Dipankar Jana

List of Publications arising from the thesis

Published in International Journals

1. Identification of the spatial location of deep trap states in AlGaN/GaN heterostructures by Surface Photovoltage Spectroscopy.
   Dipankar Jana, S. Porwal, and T. K. Sharma
   Superlatt. and Microstruct. **(2017) 112**, 249 (1-8)

2. A correlation between the defect states and yellow luminescence in AlGaN/GaN heterostructures.
   Dipankar Jana and T. K. Sharma
   J. Appl. Phys., **(2017) 122**, 035101(1-9)

3. An unambiguous identification of 2D electron gas features in the photoluminescence spectrum of AlGaN/GaN heterostructures.
   Dipankar Jana and T. K. Sharma
   J. Phys. D: Appl. Phys., **(2016) 49**, 265107 (1-7)

4. Origin of fine oscillations in the photoluminescence spectrum of 2-dimensional electron gas formed in AlGaN/GaN high electron mobility transistor structures.
   Dipankar Jana, S. Porwal, Anubha Jain, S. M. Oak, and T. K. Sharma
   J. Appl. Phys., **(2015) 118**, 164502 (1-7)

5. Pump-probe surface photovoltage spectroscopy measurements on semiconductor epitaxial layers.
   Dipankar Jana, S. Porwal, T. K. Sharma, Shailendra Kumar, and S. M. Oak
   Rev. of Sci. Instrum., **(2014) 85**, 043909(1-9)

Communicated in International Journals

1. Attribution of blue luminescence band in heavily Mg doped GaN to an electronic transition from shallow donor to deep acceptor states
   Dipankar Jana, S. Porwal, Suparna Pal, and T. K. Sharma
   Journal of Applied Physics

2. Radiative recombination mechanisms in AlGaN/GaN high electron mobility transistor structures.
   Dipankar Jana, and T. K. Sharma
   (to be resubmitted)

3. Compensation of unintentional donors in AlGaN/GaN HEMT structures by Mg-doping during initial growth of GaN buffer layer.
   Dipankar Jana, S. Porwal, Abhishek Chatterjee, Ravi Kumar, and T. K. Sharma
   (to be submitted)

Presented in Conferences/ Symposia

1. Laser Assisted Surface Photovoltage Spectroscopy: A New Tool for an Accurate Determination of the Bandgap of Semiconductor Epitaxial Layers.
   Dipankar Jana, S. Porwal, T. K. Sharma, Shailendra Kumar, and S. M. Oak
   17th Int. Workshop on the Physics of Semiconductor Devices 2013, edited by V. K. Jain and A. Verma (Springer International Publishing, 2014), p. 787

2. Pump-Probe Photoluminescence Spectroscopy Measurements for the Identification of 2DEG formed in AlGaN/GaN Heterostructure.
   Dipankar Jana, S. Porwal, Anubha Jain, S. M. Oak, and T. K. Sharma
   18th Int. Workshop on the Physics of Semiconductor Devices, 7-9 Dec. 2015, Bangalore, India

3. A Fast and Non-destructive Probing of 2-dimentional Electron Gas in AlGaN/GaN Heterostructures.
   Dipankar Jana and T. K. Sharma
   Int. Workshop on Nitride Semiconductors, 2-8 October, 2016, Orlando, USA

4. Spectroscopic Characterization of Defects in AlGaN/GaN Heterostructures.
   Dipankar Jana and T. K. Sharma
   Int. Symposium on Semiconductor Material and Devices (ISSMD-4), 8-10 March, 2017, Jadavpur University, Kolkata, India

5. Compensation of Unintentional Donors in AlGaN/GaN HEMT Structures by Mg-doping During Initial Growth of GaN Buffer Layer.
   Dipankar Jana and T. K. Sharma
   19th Int. Workshop on the Physics of Semiconductor Devices, 11-15 Dec. 2017, Delhi, India

Dipankar Jana

Dipankar Jana

This Thesis is dedicated to my parents

ACKNOWLEDGEMENTS

First and foremost, I offer my sincere gratitude to my supervisor professor Tarun Kumar Sharma for his guidance, support and encouragement during the course. He has inspired me to become an independent researcher and helped me realize the power of critical thinking. His frequent response 'you don't know it? Ok. We will teach you' to my random queries encouraged me to learn a lot from him.

My sincere thanks also go to the members of my doctoral committee: Dr. S. M. Oak, Dr. S. K. Deb, Dr. G. S. Lodha, Dr. Aparna Chakrobarty, Dr. K. S. Bindra, Dr. P. A. Naik, Dr. H. S. Rawat, Dr. S. K. Dixit, Dr. S. M. Gupta, Dr. Sandip Ghosh, Dr. Tapas Ganguli, Dr. Maulindu Kumar Chattopadhyay, Dr. M. H. Modi, and Dr. Rama Chari. They generously gave their time to offer me valuable comments toward improving my work.

I would also like to thank all members of semiconductor section, Dr. V. K. Dixit, Dr. Shailendra Kumar, Mr. Shailesh K. Khamari, Dr. Suparna Pal, Dr. S. D. Singh, Mr. Abhishek Chatterjee, Mr. Ravi Kumar, Mr. Subhomoy Halder, Miss. Geetanjali for fruitful discussions regarding my project; Mr. Sanjay Porwal, Mr. Alexander Khakha, Mr. Vishal Agnihotri, Mr. U. K. Ghosh, Mr. G. Jayaprakash, and Mr. A. K. Jaiswal for their valuable help in performing experiments.

I would like to thank Dr. A. Jain and Dr. S. Lamba for providing nitride samples, Mr Anirudhha Bose, Dr. D. Alamelu for SIMS measurements.

A very special gratitude goes to HBNI, RRCAT and DST for providing the financial assistance for the work and international travel.

I am grateful to my family who have provided me through moral and emotional support in my life.

I would also like to extend warm thanks to my awesome friends, Smriti, Paro, Gopal, Yash, Ganga, Disha, Ani, Sahiba, Sukli, Naba, Annu, Sappu, Deba, Arijit, KK, Chiru, Arup, and Suman for being with me in good and bad time, tolerating my craziness, mental support, and encouragement.

CONTENTS

Synopsis i

List of Figures xii

List of Tables xxvii

Chapter 1. Introduction 1

1.1 A Brief History of III-Nitride HEMT 3

1.2 Crystal Structure and Polarization 4

1.3 Polarization in AlGaN/GaN Heterostructures 6

1.4 Formation of Two Dimensional Electron Gas in AlGaN/GaN Heterostructures 7

1.5 Ideal HEMT Characteristics 9

1.6 Non-idealities of GaN HEMT 10

1.7 Imperfections in GaN 12

1.8 Optical Transitions in GaN and AlGaN/GaN Heterostructures 14

1.9 Literature Survey and Scope of Present Work 17

Chapter 2. Experimental Techniques 27

2.1 Introduction 27

2.2 Reflectance Spectroscopy..... 28

2.3 Photoluminescence Spectroscopy 32

2.4 Photoluminescence Excitation Spectroscopy 35

2.5 Surface Photovoltage Spectroscopy..... 37

2.5.1 Experimental configuration of SPS measurements 41

2.5.1.1 Kelvin Probe Method …….. 42

2.5.1.2 Metal Insulator Semiconductor Configuration of SPS…… 43

2.6 Pump-probe SPS Measurements: A New Configuration for Probing Heterointerface …… 46

2.7 Conclusion ……..... 54

Chapter 3. Optical Characterization of Defects in GaN and AlGaN/AlN/GaN Heterostructures …… 55

3.1 Introduction ……... 55

3.2 Sample Detail …… 56

3.3 Characterization of Blue Luminescence Band in Heavily Mg Doped GaN ……... 57

3.3.1 PL Characterization …….. 57

3.3.2 SPS Characterization …… 62

3.4 Characterization of Yellow Luminescence Related Defect States in AlGaN/GaN Heterostructure ……. 67

3.4.1 SPS Characterization …… 68

3.4.1.1 Identification of Spatial Location of Defects …….. 71

3.4.1.2 Identification of Spectral Origin of Defects …… 73

3.4.1.3 Temperature Dependence of Defect Related SPS Features. 76

3.4.2 PL and PLE Characterization ……... 80

3.4.2.1 Recombination model ……. 83

3.5 Conclusion ……..... 90

Chapter 4. Identification of 2-dimentional Electron Gas Present in AlGaN/AlN/GaN Heterostructure by Spectroscopic Techniques 93

5.1 Introduction 93

5.2 Sample Details 95

5.3 Origin of Fine Oscillation in 2DEG PL Spectrum 96

5.3.1 Temperature Dependence of Fine Oscillations 100

5.3.2 Excitation Intensity Dependence of Fine Oscillations 102

5.4 Identification of 2DEG PL Feature 107

5.5 Characterization of 2DEG PL Feature 111

5.5.1 Temperature Dependence of 2DEG PL Feature 112

5.5.2 Excitation Intensity Dependence of 2DEG PL Feature 115

5.5.3 Dominance of Interference Oscillations 118

5.6 Radiative Recombination Mechanism of 2DEG with Photo-excited Holes 121

5.7 Conclusion 128

Chapter 5. Impact of Mg-doped GaN Buffer on the optoelectronic properties of AlGaN/GaN High Electron Mobility Transistors 131

5.1 Introduction 131

5.2 Sample Details 133

5.3 Effect of Mg Doping on Compensation of Defects 134

5.4 Impact of Mg Doping on 2DEG Confinement 138

5.5 Conclusion 140

Chapter 6. Summary and Future Scope 141

6.1 Summary of the Thesis and Conclusion 141

6.2 Scope for Future Work 146

Appendix 147

Appendix A 147

Appendix B 148

Appendix C 149

Bibliography 155

List of Figures

Figure 1.1 (a) Stacking of Ga and N atoms in (a) unit cell of wurtzite GaN and (b) along [0 0 0 1] direction in N-polar and (c) Ga-polar direction…… 5

Figure 1.2 Polarization components in AlGaN/GaN heterostructure with different polarity. PSP and PPE stands for spontaneous and piezoelectric polarization respectively…… 7

Figure 1.3 Schematic band diagram of AlGaN/GaN heterostructure. E_C, E_V and E_F corresponds to conduction band, valence band and Fermi level respectively... 8

Figure 1.4 Schematic of an ideal AlGaN/GaN HEMT structure in (a) normal and (b) pinch off condition. S and D corresponds to source and drain respectively. Pinch off condition is obtained by applying bias which is not shown. (c) Schematic I-V characteristics of an ideal HEMT. I_{DS}, V_{DS}, V_{knee} and V_{br} corresponds to drain current source to drain voltage knee voltage and breakdown voltage respectively…… 10

Figure 1.5 Schematic of a non-ideal AlGaN/GaN HEMT structure in (a) normal and (b) pinch off condition. S and D corresponds to source and drain respectively. (c) Schematic I-V characteristics of a non-ideal HEMT. I_{DS}, and V_{DS} correspond to drain-source current and drain-source voltage respectively. The ideal (non-ideal) curves are shown by black (blue) lines respectively along with the leakage current…….. 11

Figure 1.6 Schematic of (a) E-k diagram of GaN, (b) defect states and corresponding optical transitions in GaN, and (c) AlGaN/AlN/GaN heterostructure with optical transitions. A, B and C corresponds to three valence bands of GaN. E_g and FX_A correspond to bandgap of GaN and free exciton recombination energy respectively. E_C, E_V, E_F, E_{SD}, E_{DD}, E_{DA}, E_{SA}, and E_{DS} correspond to conduction band, valence band, Fermi level, shallow donor, deep donor, deep acceptor, shallow acceptor and deep state respectively. G, DAP, BL and YL corresponds optical generation, donor-acceptor pair recombination, blue luminescence and yellow luminescence respectively……. 15

Figure 1.7 (a) Configuration coordinate diagram and corresponding optical transitions in C_N-O_N defect complex, (b) Schematic location of deep levels formed by different charge states of C_N-O_N and C_N deep defects within the bandgap of GaN…….…. 19

Figure 1.8 (a) 40 K PL spectra of AlGaN/GaN heterostructure, (b) temperature dependence of energy separation (ΔE) between 2DEG peak (E_0) from GaN free exciton (FX_A) emission, and (c) Excitation intensity dependence of E_0 at 10 K. LO_{FXA} corresponds to the 1st longitudinal phonon replica of free exciton-A……. 24

Figure 2.1 Schematic ray diagram to illustrate the multiple reflections and transmission within a transparent sample where d and E_0 correspond to the thickness of layer and amplitude of incident light respectively. r_1 (r_1'), and t_1 (t_1') correspond to reflection and transmission coefficients of air/layer surface when light is propagating from air to material (material to air) respectively. r_2'

corresponds to reflection coefficient of layer/substrate interface…….. 29

Figure 2.2 Schematic diagram of the reflectivity spectroscopy setup. Symbols M, F, L, C, BS, S and D corresponds to monochromator, long pass filter, lens, chopper, beam splitter sample and detector respectively…….. 31

Figure 2.3 Schematic diagram showing various electronic transitions that are possible in a PL process. Symbols G, E_c, E_v, E_{SD}, E_{DS}, E_{SA} stand for excitation process, conduction band, valence band, shallow donor, deep traps, and shallow acceptor respectively…….…. 33

Figure 2.4 Schematic diagram of a photoluminescence spectroscopy setup where symbols C, F, m, L, D, M and S stand for mechanical chopper, optical filter, mirror, lens, detector, monochromator and sample respectively……. 34

Figure 2.5 Schematic diagram of a PLE setup where symbols C, F, M, L, D, S, and Xe/QTH stand for mechanical chopper, optical filter, mirror, lens, detector, sample, and Xenon/quartz tungsten halogen lamp respectively……. 36

Figure 2.6 Schematic band diagram of (a) n-type semiconductors, (b) semi-insulating semiconductor, and (c) a p-n junction under dark (solid lines) and light illumination (short dashed lines) condition. Symbols Vs, E_c, E_F, and E_V E_{DS}, E_{SA} stand for surface potential (bend bending), conduction band, Fermi level and valence band respectively…….. 39

Figure 2.7 Schematic diagram of n-type semiconductor showing (a) valence band to trap and (b) trap to conduction band transition. The symbols E_C, E_F, and E_V corresponds to conduction band, Fermi level and valence band respectively.. 41

Figure 2.8 Schematic diagram to describe the mechanism of generation of SPV signal in Kelvin probe method, a) short circuit, b) under dark, and c) under illumination. The symbols Φ_M, Φ_S, V_{CPD}, E_{vac}, E_C, E_F, and E_V corresponds to work function of metal, work function of semiconductor, contact potential difference, vacuum level, conduction band, Fermi level and valence band respectively……. 43

Figure 2.9 Schematic diagram of the SPS measurement setup. L, F, TCG, and S stand for the focusing Lens, order sorting Filter, Transparent Conducting Glass, and Sample, respectively. Pump beam is either a laser or an assembly of Xenon arc-lamp and a monochromator…….…. 46

Figure 2.10 Schematic diagram of the pump-probe SPS measurement setup. Symbol TCG and C stand for transparent conducting glass and chopper respectively. Pump beam is either a laser or an assembly of Xenon arc-lamp and a monochromator…… 48

Figure 2.11 SPS magnitude spectra and (b) pp-SPS magnitude with 1064 nm laser spectra of p-GaAs/SI-GaAs at 28 Hz chopping frequency. Inset shows the comparison of pp-SPS and absorption spectra of GaAs over the same spectral range. The pp-SPS spectra is normalized with the value of α at 1.45 eV for comparison purpose…… 48

Figure 2.12 Room temperature SPS and pump-probe SPS (a) amplitude and (b) phase spectra of p-GaN sample recorded at 166 Hz modulation frequency. BGE and AGE corresponds to below bandgap pump excitation at 3.02 eV from lamp-monochromator assembly and above bandgap pump excitation at 3.81 eV from CW 325 nm laser respectively……..... 50

Figure 2.13 Schematic band diagram of p-GaN sample. Symbols E_C, E_V, E_F and E_{DA} corresponds to conduction band, valence band, Fermi level and deep acceptor state respectively…….……. 52

Figure 3.1 Room temperature PL spectra of p-GaN and n-GaN epitaxial layers where labels FX_A, BL and YL corresponds to Free exciton-A, blue luminescence and yellow luminescence respectively……. 58

Figure 3.2 (a) Temperature dependent PL spectra of p-GaN sample recorded at 0.8 W/cm^2 excitation intensity. (b) Temperature dependence of the integrated BL intensity of p-GaN sample. YL, BL and FX_A corresponds to yellow luminescence band, blue luminescence band and free exciton-A respectively.…. 58

Figure 3.3 Room temperature SPS (a) magnitude and (b) phase spectra of p-GaN and n-GaN samples recorded at 28 Hz modulation frequency. Schematic band diagram of p-GaN sample showing upward transitions according to (c) model-1 and (d) model-2. E_C, E_V, E_{DD}, E_{SA}, E_{DA}, E_{DS} corresponds to conduction band, valence band, deep donor, shallow acceptor, deep acceptor and deep state respectively……..... 63

Figure 3.4 Temperature dependent SPS magnitude spectra of p-GaN sample recorded at 1 kHz modulation frequency…….. 65

Figure 3.5 Room temperature SPS and Pump-Probe SPS (a) magnitude, and (b) phase spectra of AlGaN/GaN heterostructures recorded at 28 Hz chopping frequency…….... 69

Figure 3.6 Schematic band diagram of the AlGaN/GaN heterostructure (sample-A) where symbols 2DEG, E_C, E_V, E_F, E_{SD}, and E_{DS} stand for 2-dimensional electron gas, conduction band, valence band, Fermi level, shallow donor and deep trap states respectively. Note that the band profile is drawn not to scale and is enlarged in certain locations to illustrate the field driven regions for the purpose of clarity. Inset shows the geometry of SPS measurements performed under front and back illumination schemes……. 70

Figure 3.7 (a) Normalized pump-probe SPS magnitude corresponding to feature-4 and feature-5 are plotted as a function of pump beam intensity where solid lines are only a guide to eye. The schematic band diagram of AlGaN/AlN/GaN heterostructure near GaN/Fe-GaN interface in (b) absence and (c) presence of 1064 nm pump laser. The symbols E_C, E_V, E_F and E_{DS} correspond to conduction band, valence band, Fermi level and deep state respectively. Probe beam is shown by red vertical arrow with chopper symbol while the pump beam is shown by blue vertical arrow……. 75

Figure 3.8 Temperature dependent SPS (a) magnitude and (b) phase spectra of Sample-A recorded at 28 Hz modulation frequency. Modulation frequency dependence of room temperature (c)SPS magnitude at 3.39 eV (feature-3) and 10 K SPS magnitude at 3.35 eV (feature-7)……... 77

Figure 3.9 10 K SPS and pump-probe SPS spectra of AlGaN/GaN heterostructure recorded at 28 Hz chopping frequency…….…. 79

Figure 3.10 (a) Room temperature PL spectra of Sample-A which is recorded with 325 nm laser as an excitation source; (b) room temperature PLE and pump-probe PLE spectra corresponding to yellow luminescence of Sample-A sample. The symbols FX_A and YL corresponds to free exciton-A and yellow luminescence respectively. pump-probe PLE measurements are performed from front surface…… 81

Figure 3.11 (a) A schematic diagram to illustrate the absorption and emission processes in undoped GaN layer. E_C, E_V, E_{DS}, N_{DS}, f_{DS}, G_1, G_2, n, p, B, and C_{pD} corresponds to conduction band, valence band, deep trap state, density of deep trap state, occupation function of deep trap state, generation rate by probe beam, generation rate by sub-bandgap pump beam, density of electron in E_C, density of holes in E_V, radiative recombination coefficient and hole capture coefficient of E_{DS} respectively; (b) Numerically simulated values of the normalized intensity (I_N) of YL feature and occupation probability of deep trap states (f_{DS}) plotted as a function of the intensity of probe beam (G_1) at a given value of intensity of sub bandgap pump beam (G_2). Similarly, the variation of I_N and f_{DS}

is also shown as a function of G_2 for a given value of G_1…….. 84

Figure 3.12 (a) Normalized PL intensity (I_N) of YL feature plotted as a function of probe beam intensity at two excitation energies under pump-probe PLE configuration. The G_1 corresponding to the excitation intensity of 3.82 eV excitation is shown in upper x-axis. (b) Normalized PL intensity (I_N) of YL feature plotted as a function of pump beam (1064 nm laser) intensity at two excitation energies under pump-probe PLE configuration. Numerically simulated variation of I_N (black solid line) at 3.82 eV excitation energy is also shown…….. 88

Figure 4.1 (a) Temperature dependent PL spectra of AlGaN/AlN/GaN heterostructures (Sample-A) recorded at 0.02 W/cm^2 excitation intensity; (b) excitation intensity dependent PL spectra of Sample-A at 10 K where WL stands for the white light excitation sources tuned at 325 nm. The symbols D^0X, A^0X, FX_A, and $FX_A(n=2)$ stand for the donor bound exciton, acceptor bound exciton, free A-exciton, and the excited state of free A-exciton transitions of GaN while DAP stands for the Donor-acceptor pair (DAP) transition respectively. The phonon replicas of DAP and D^0X are labeled as LO_{DAP} and $LO_D{}^0{}_X$ respectively. Two broad features superimposed with several fine oscillations, labeled as E_0 and E_1, are related to the 2DEG at AlN/GaN heterointerface. Vertical dashed lines are drawn at a particular fine oscillation and at FX_A to visualize temperature and excitation intensity dependent shift….. 97

Figure 4.2 The conduction band profile and electron wave functions of Sample-A. The symbols E_C, Ψ_0, Ψ_1 corresponds to conduction band, ground state electron wave function and excited state wave function respectively. The wave functions are vertically shifted to the corresponding eigenenergies. The dotted line corresponds to Fermi level…….. 98

Figure 4.3 Schematic of angle dependent PL and edge PL measurements. I, S and θ corresponds to excitation, sample and collection angle respectively…….. 99

Figure 4.4 Angle dependent 10 K Photoluminescence spectra of sample-A where the viewing angle is measured from the surface normal. In case of edge PL, sample is excited from the front surface whereas the luminescence is collected from the edge (90°). The spectra are recorded with an excitation intensity of ~60 W/cm^2. D^0X, FX_A, and FX_A (n=2) stand for the donor bound exciton, free exciton-A, and the excited state of free exciton-A transitions of GaN respectively. The phonon replica of FX_A feature are labeled as LO_{FXA}. A broad feature (E_0) superimposed with several fine oscillations is related to the 2DEG at AlN/GaN heterointerface. The spectra are vertically shifted for clarity……..... 99

Figure 4.5 (a) Temperature dependent reflectivity spectra of Sample-A which is recorded under normal incidence condition. Vertical dashed line drawn at 3.495 eV and 3.36 eV marks the energy of free exciton-A (FX_A) and a particular oscillation peak (1) at 10 K respectively. The energy difference between FX_A and '1' is schematically marked as ΔE. The symbol FX_B corresponds to free

exciton-B. (b) Temperature dependences of ΔE as obtained from reflectivity and PL measurements……. 101

Figure 4.6 (a) The simulated excitation intensity dependent PL spectra which is obtained from the convolution of broad Gaussian peak with 10K reflectivity spectrum. The broad Gaussian peak for different excitation intensity is obtained by fitting E_0 PL peak in Fig. 4.1 (b). The symbol I stands for laser intensity. Excitation intensity dependence of peak energy of one of the fine oscillations, marked by a vertical dashed line, is also shown. (b) Excitation intensity dependence of fine oscillation peak which is obtained from simulation and experiment……..... 103

Figure 4.7 Refractive index dispersion of GaN at 10 K and room temperature. Solid lines are the fit with second order Sellmeier equation where the values of coefficients are summarized in Table 4.1. Refractive index dispersion of GaN at 300K which is taken from Ref. 189 is also plotted in the same graph for comparison purpose. Inset shows the experimental and numerically simulated reflectivity spectra for the transparent region of GaN…… 105

Figure 4.8 Fit of the interference oscillations observed in the PL spectra of AlGaN/GaN based HEMT structures where plots (i), (ii), (iii), and (iv) are made by taking the experimental data based on the low temperature PL spectra from [182]ref. 182, [136]ref. 136, [135]ref. 135 and [134]ref. 134 respectively. Here, the slope of the curve is inversely proportional to the thickness of GaN layer. The estimated (reported) values of GaN layer thickness for the curves (i), (ii), (iii), and (iv) are

2.06 μm (2.03 μm), 3.27 μm (not given), 2.47 μm (2.69 μm), and 3.81 μm (3.28 μm) respectively……. 106

Figure 4.9 Schematic band diagram of (a) as grown AlGaN/AlN/GaN heterostructure (Sample-A) and (b) after etching top AlGaN barrier layer, AlN inter layer and a part of GaN Channel layer. The symbol E_C, E_V and E_F corresponds to conduction band, valence band and Fermi level respectively. G, D, E_0 and FX corresponds to optical excitation, carrier redistribution, 2DEG recombination and free exciton recombination respectively…….. 108

Figure 4.10 10 K PL spectra of Sample-A (unetched) and after etching top AlGaN barrier layer, AlN inter layer and a part of GaN Channel layer (etched). D^0X, FX_A, and FX_A (n=2) stand for the donor bound exciton, free A-exciton, and the excited state of FX_A of GaN while DAP, and eA stand for the donor acceptor pair and conduction band to acceptor transition respectively. D^0X(2e) stands for the two electron replica of the D^0X feature while longitudinal phonon (LO) phonon replicas of DAP, FX_A and D^0X are also shown. Two broad features, labelled as E_0 and E_1, are related to the ground and excited states of 2DEG at the AlN/GaN heterointerface, respectively. The inset shows the 10 K PLE spectrum corresponding to the ground state (E_0) PL feature of 2DEG where FX_A, FX_B, and FX_C stand for free exciton features corresponding to the three valence bands of GaN…… 109

Figure 4.11 Temperature dependence of integrated PL intensity of E_0 feature and the energy separation (ΔE) between the ground state (E_0) feature of 2DEG and GaN free exciton peak (FX_A)……..… 112

Figure 4.12 (a) Temperature dependent PL spectra of Sample-A recorded at very low excitation intensity for observing the behavior of E_1 feature. (b) Excitation intensity dependent normalized PL spectra of the sample at 10 K where WL stands for the white light excitation sources tuned at 325 nm. The symbols D^0X, FX_A, FX_B A^0X, $FX_A(n=2)$ and $D^0X(2e)$ stand for the donor bound exciton, free A-exciton, free B-exciton, acceptor bound exciton, excited state of free A-exciton and two electron replica of D^0X transitions of GaN respectively. The phonon replica of FX_A is labeled as LO_{FXA}…….... 115

Figure 4.13 (a) Excitation intensity dependence of (a) the ground (E_0) and excited (E_1) state energy levels of 2DEG, (b) the screened polarization induced electric field, and (c) the normalized integrated PL intensity of E_0, band edge PL (E_g) for the as-grown Sample-A and DAP features for the top barrier layer etched Sample-A. (d) The conduction band profile, 2DEG eigenstates, and electric field of Sample-A, and (e) Excitation intensity dependent PL spectra of the etched Sample-A. The symbols D^0X, D^0X (2e), eA, and DAP corresponds to donor bound exciton, two electron replica of donor bound exciton, electron acceptor pair and donor-acceptor pair respectively. The phonon replicas are labeled as LO. 'I' corresponds to excitation intensity…… 116

Figure 4.14 (a) 10 K PL and reflectivity spectra of Sample-A recorded under normal incidence condition where D^0X, E_0, E_1, and BL stand for the donor bound exciton, 2DEG ground state, 2DEG excited state and blue luminescence PL features respectively; (b) shows the interference oscillations at different spectral position which is obtained from PL spectra…….. 119

Figure 4.15 (a) 10 K Excitation intensity dependent PL spectra of Sample-A where the normalized PL spectra at some intermediate excitation intensities are shown in (b). 10 K excitation intensity dependence of E_0 feature and feature-X (c) peak energy, (d) FWHM, and (e) Integrated intensity of Sample-A. The symbols D^0X, FX_A, FX_A (n=2), LO_{FXA}, and E_0 stand for donor bound exciton, free exciton-A, excited state of FX_A, optical phonon replica of FX_A, ground state of 2DEG respectively. 'I' stands for excitation intensity……... 124

Figure 4.16 (a) Potential profile, eigenstates and the transitions occurring at the triangular potential well for two values of electric field are plotted as a function of depth at a) 1 MV/cm and b) 0.25 MV/cm electric field respectively. The ground state (E_0) and 1st excited state (E_1) energy values are shown along with the Fermi level (E_f). 2DEG ground state PL transition is also marked by a downward arrow. (b) Distribution of 2D-electrons with the depth for AlGaN/AlN/GaN HEMT structure at a few excitation power where curves 1,2,3,4 and 5 stand for 0.012, 0.25, 5.7, 227 and 4281 mW/cm^2 exitation intensity respectively. The horizontal dash line mark the carrier density of $2x10^{18}cm^{-3}$ which corresponds to critical Mott carrier density. Inset shows the varitaion of critical Mott thickness as a function of excitation power……... 126

Figure 5.1 SIMS profile of Mg dopant concentration in AlGaN/GaN heterostructures where arrows mark the location of layer/template interface. Inset shows the (0002) HRXRD pattern of sample-A. The fitted data is also shown in the inset……..……. 134

Figure 5.2 Room temperature PLE spectra of AlGaN/AlN/GaN heterostructures where the detection wavelength is set to YL peak of PL spectra. Inset shows the PL spectra of Sample-A which is recorded with 325 nm excitation from a Xe lamp and monochromator assembly. The symbols FX_A, and YL corresponds to free exciton A and yellow band respectively. Valence band to shallow donor transition is marked by holes-to-donor (h-D) while the vertical dashed line is a guide to band edge of GaN. ……..... 136

Figure 5.3 (a) Room temperature and (b) 10 K SPS spectra of AlGaN/AlN/GaN heterostructures which are recorded at 28 Hz modulation frequency. The symbols FX, h-D, and DS-e corresponds to free exciton transitions, valence band to shallow donor transition, and resonant transition in YL related deep defect complex respectively. Dotted line shows the background signal in SPS measurements……. 137

Figure 5.4 (a) 10 K PL spectra of AlGaN/AlN/GaN heterostructures recorded with a moderate optical excitation intensity and (b) schematic band diagram of the two heterostructures and corresponding transition energies. FX_A, D^0X, DAP and LO_{DAP} corresponds to free exciton-A, neutral donor bound exciton, donor-acceptor pair and longitudinal optical phonon replica of DAP respectively. E_0

corresponds to 2DEG-photoexcited hole recombination. E_C, E_V and E_F are conduction band, valence band and Fermi level respectively…… 139

Figure A1 (a) Schematic ray diagram to illustrate the multiple reflections of PL signal within the F-P cavity, b) Transmitted PL intensity versus energy for distributed (red) PL generation and confined (blue) PL generation along the depth of the sample……. 150

List of Tables

Table 1.1 A comparison of Material properties of various semiconductors. Johnson Figure of Merit (JFOM) is a measure of the ultimate high frequency capability of the material where as Baliga's figure of merit (BFM) is a measure of the specific on-resistance of the drift region of a vertical FET…….. 2

Table 4.1 Coefficients of the second order Sellmeier equation given by,

$$n(\lambda)=\sqrt{A_0+\frac{A_1\lambda^2}{\lambda^2-B_1^2}+\frac{A_2\lambda^2}{\lambda^2-B_2^2}}$$ ……. 107

SYNOPSIS

Technological breakthroughs in the epitaxial growth of III-Nitride materials and associated heterostructures have enabled the development of several advanced semiconductor devices like high power/frequency high electron mobility transistors (HEMT),[1,2] high efficiency light emitters[3] and solar/visible blind ultraviolet photodiodes.[4] It became possible due to the superior fundamental characteristics of nitride materials such as large direct bandgap, high electrical breakdown, high thermal conductivity and high saturation velocity of carriers. In case of HEMT structures, a large density of two-dimensional electron gas (2DEG) is formed at AlGaN/GaN heterointerface due to the presence of a large polarization field discontinuity.[5] Since the 2DEG is spatially separated from ions, it exhibits a large electron mobility and also a high saturation velocity which is essential for the realization of high frequency switching devices. Whether it be the development of high power HEMT or high efficiency blue-green light emitting diodes (LEDs), nitride materials have revolutionized the world of semiconductor devices. In particular, the development of high efficiency blue LEDs has proven to be a wonderful gift to mankind in the form of "LED bulb".

In spite of many noteworthy developments, nitrides still have a few hurdles to overcome which currently restricts further improvements of device characteristics. One inherent problem is related to the presence of a huge density of defects and dislocations in nitride heterostructures. It occurs due to the large lattice and thermal mismatch that is generally present in nitride epitaxial architecture since native GaN substrates are not yet easily available. A major consequence of this appears in terms of a large n-type conductivity of GaN epilayers due to the unintentional doping by residual impurities

such as silicon and oxygen. It leads to high buffer leakage current, low breakdown voltage, and parasitic losses in GaN based HEMT devices.[6,7] Though the formation of defects/dislocations is inevitable in nitride epitaxial layers, an unambiguous identification of defects can greatly help in improving the crystalline quality of nitride epitaxial layers. Spectroscopic techniques can provide vital information related to such defects. These are usually preferred over other characterization methods due to their non-destructive nature. However, key information related to the layer properties is sometimes hindered by the features associated with defects in spectroscopy measurements. New methodologies of spectroscopic experiments for the characterization of nitride epitaxial layers are thus desirable. Another critical issue is related to compensation of native defects where the concept of p-type doping of GaN buffer layer have been suggested for suppressing the problem of parallel conduction in nitride HEMT grown on Iron doped GaN templates.[8,9] However, acceptors in GaN are known to introduce mid gap states of complex nature. Understanding of the defect states associated with p-type dopants is therefore of paramount importance for the realization of novel nitride devices. Further, a firm confirmation of the presence of 2DEG in AlGaN/GaN HEMT structures prior to device fabrication is essential. Here, a non-destructive characterization of 2DEG states is very attractive. However, spectroscopic characterization of 2DEG states in AlGaN/GaN HEMT structures is challenging since one finds a considerable overlap between the 2DEG features and interference oscillations/defect features that are generally observed in the sub bandgap region of GaN. New methodologies for the spectroscopic characterization of AlGaN/GaN HEMT structures are thus essential.

This thesis deals with the development of novel methodologies for spectroscopic characterization of nitride epitaxial layers. Spectroscopic features associated with epilayers, defects and other subsidiary phenomena in AlGaN/GaN HEMT structures are carefully recorded and analyzed. Fundamental mechanisms associated with various electronic transitions seen in the spectroscopic measurements are discussed. In particular, origin of yellow luminescence (YL) band in AlGaN/GaN, and blue luminescence (BL) band in heavily dopes p-GaN are discussed. In a later part, spectroscopic measurements are presented for an unambiguous identification of 2DEG features in AlGaN/GaN HEMT structures. The thesis is organized as follows:

In **Chapter 1**, an introduction to III-nitrides is provided by highlighting the key properties of these materials that differ from other III-V semiconductors. Literature survey on the advancements in III-nitride semiconductor materials, various applications and bottlenecks are given in this chapter. Dominant defects that are present in GaN based heterostructures, various tools to identify and characterize such defects and the associated mechanism are also discussed in brief. Importance of the presence of 2DEG in AlGaN/GaN heterostructures and the challenges which are associated with an unambiguous identification of the true signatures of 2DEG by spectroscopic techniques are also briefly mentioned.

Chapter 2 contains a description of experimental techniques that are used in course of this thesis work. Basic principles of the spectroscopy techniques like reflectivity, photoluminescence (PL), photoluminescence excitation (PLE) and surface photovoltage spectroscopy (SPS) are briefly described in this chapter. Sample preparation of GaN epitaxial layers and AlGaN/GaN heterostructures is also

mentioned. Advantages and limitations of various spectroscopic techniques are also compared in this chapter.

New methodologies for performing SPS measurements under pump-probe configurations are introduced in this chapter. It is already known that the involvement of surface states, interface states and bulk trap states significantly affects the usefulness of SPS in determining the optical bandgap. By choosing an appropriate power of the apparent pump beam, the contribution of sub-bandgap states can be effectively suppressed which otherwise swamp the bandgap related information. Bandgap of epilayers can be accurately measured even under the strong influence of localized states by conducting SPS experiments under the modified configuration. It is discussed that by changing the energy/intensity of pump beam and illumination configuration, one can pinpoint the spectral and spatial location of defect features in nitride epitaxial layers. Usefulness of the modified technique is proven by investigating several epilayers like p-GaAs/SI-GaAs, heavily doped GaN: Mg and AlGaN/GaN heterostructures.

Performance of AlGaN/GaN HEMT devices is considerably influenced by the crystalline quality of GaN channel layer. In view of this, study of defects lying in GaN buffer layer is essential. Spectroscopic characterization of defects in GaN epitaxial layers and AlGaN/GaN heterostructures is discussed in **Chapter 3**. Two major issues related to the presence of blue luminescence (BL) and yellow luminescence (YL) bands in PL spectra are discussed in detail. Fundamental origin of the two PL bands is not yet clear since conflicting reports keep appearing in literature. In order to nullify the problem of parallel conduction at GaN/Fe-GaN interface, p-type doping of a part of GaN buffer layer is considered to be a viable option for the development of AlGaN/GaN HEMT devices. However, a large incorporation of Magnesium (Mg) in

GaN might lead to unnecessary complications. Spectroscopic measurements can provide vital information here since a strong BL band always appears in heavily doped p-GaN samples.[10] In this chapter, complementary spectroscopic measurements such as PL and SPS are performed on heavily doped GaN:Mg epitaxial layers to identify shallow/deep levels which contributes to the BL band. Availability of this knowledge can help in the minimization of defects associated with heavy p-doping of GaN channel layer. During the course of this thesis work, signature of defects states associated with BL band are clearly seen in PL and SPS spectra. Further, activation energy of 24±2 meV and 396±132 meV are estimated from the temperature dependent PL measurements in the low and high temperature ranges respectively. The low activation energy is correlated with the activation of electrons from shallow donor states to conduction band while the high activation energy is associated with the excitation of holes from deep acceptor states to valence band. Systematic spectroscopic measurements confirm that the BL band originates from a conduction band/shallow donor level to deep acceptor state transition.

Next, the origin of YL band in the PL spectra of AlGaN/GaN HEMT structure is discussed in this chapter. In literature, intensity ratio corresponding to the band edge and YL band signals in GaN is often used to define the purity of epilayers. However, the exact attribution of YL band to specific defects and its spatial location in GaN is a matter of intense debate.[11] Here, SPS and photoluminescence excitation (PLE) measurements both in conventional and under pump-probe configurations are performed with an overall aim to identify the defect states along with their spatial location in AlGaN/GaN heterostructures. Features related to shallow donor state at ~30 meV below the conduction band and a deep trap state at ~1 eV above the valence band

maxima are clearly observed in room temperature SPS spectra. Further, a major contribution to these features arises from GaN/Fe-GaN interface. SPS and PLE measurements reveal that the deep trap states are related to C_N-O_N deep donor complex and are found to be responsible for generation of YL band in GaN. Further, a simple phenomenological model based on the electronic transitions involving a three-level system is proposed to explain the intensity dependence of YL feature under pump-probe configuration. Systematic spectroscopic measurements presented in this chapter therefore help in the solution of two challenging problems which have been lingering in nitrides for a long time.

In **Chapter 4,** attention is paid to an unambiguous identification of 2DEG features in the PL spectra of AlGaN/GaN HEMT structures. Contactless characterization of 2DEG PL features is specifically important for the optimization of the device characteristics of AlGaN/GaN HEMT. Due to spatially indirect recombination of 2-dimensional (2D) electrons with photo-excited holes, 2DEG related PL features are expected to appear in the sub-bandgap region of GaN. It is therefore difficult to distinguish the 2DEG related PL feature from the defect PL features of GaN buffer layer. Further, the sample acts like a Fabry-Perot cavity for the sub-bandgap luminescence signal leading to the appearance of strong interference oscillations which makes the identifications of 2DEG PL feature more challenging.

In literature, interference oscillations have been erroneously identified as either the sub-levels of 2DEG formed at AlGaN/GaN heterointerface or the donor-acceptor pair transitions in GaN buffer layer. During the course of this thesis work, the origin of oscillatory features is probed by performing the angle dependent PL and reflectivity measurements under identical conditions. Systematic variation of peak energy with

angle and a decent match between the simulated and experimental spectra confirms that the fine oscillations are not at all related to 2DEG sublevels. Further, peculiar temperature dependent redshift and excitation intensity dependent blueshift of the oscillatory features, which were interpreted as the main characteristics of 2DEG sub-levels in HEMT structures by other researchers, are understood by invoking the wavelength and temperature dependence of the refractive index of GaN within the framework of interference phenomenon.

After establishing the association of fine PL features with interference oscillations, the focus is next shifted to the identification of 2DEG features in PL spectra. In order to obtain a firm confirmation of 2DEG features, PL measurements are performed on a HEMT sample where top AlGaN barrier layer is removed by the dry etching process. Disappearance of a particular PL feature in case of etched sample confirms that the specific feature is indeed related to 2DEG. It is also seen that the 2DEG feature does not saturate at high excitation intensity which distinguishes it from the defect related PL features of AlGaN barrier layer as mentioned in the previous chapter. Although, one can identify 2DEG PL features in case of etched samples but such a method is undesirable due to its destructive nature. In this context, systematic temperature and excitation intensity dependent PL measurements are performed on AlGaN/GaN HEMT structures to find some unique properties of 2DEG features. Two broad PL features related to the ground and excited sates of 2DEG are observed below the GaN band edge feature at cryogenic temperatures. The ground (excited) state PL feature is observed only up to 90 K (30 K). The activation energy of the ground (excited) state of 2DEG sub-level is estimated from the Arrhenius plot which turns out to be 38 meV (6.6 meV). The value of activation energy is found to be rather low when

compared with the confinement energy of 2DEG states in AlGaN/GaN heterostructures. Schrödinger and Poisson equations are then solved in a self-consistent manner which also predict relatively large confinement energy for the 2DEG states. Thereafter, a low value of activation energy is explained by considering the thermal escape of the photo-excited holes from AlGaN/GaN heterointerface rather than the thermal escape of 2D-electrons from triangular potential well. Temperature and excitation intensity dependencies of 2DEG PL features are explained by considering the temperature dependent bandgap shrinkage, polarization field screening by thermally/photo generated carriers and thermal escape of holes away from the AlGaN/GaN hetero-interface. The value of built-in electric field at the hetero-interface is estimated from the PL peak energy of 2DEG sub-levels which turns out to be 1 MV/cm. It is found to be in good agreement with the theoretically predicted value from a self-consistent solution of Schrödinger and Poisson equations. It therefore certifies that one can attain an unambiguous identification of 2DEG states in the PL spectra of AlGaN/GaN HEMT sample in a completely non-destructive manner.

At the end of this chapter, the recombination mechanisms of 2DEG in AlGaN/GaN heterostructures with photo-excited holes are investigated by performing excitation intensity dependent PL measurements at 10 K. Excitation intensity is varied over 6 orders of magnitude. In low excitation regime, 2DEG PL transition is found to be excitonic where integrated PL intensity increases linearly with the excitation intensity. Beyond a certain excitation intensity, a sharp PL feature appears whose integrated intensity increases super-linearly with the excitation intensity. Several possibilities such as non-k conserving transitions, recombination of the excited state of 2DEG, Fermi edge singularity and free carrier recombination of 2D electrons with

photo-excited holes are considered to understand the origin of new PL feature. Out of all these possibilities, free carrier recombination of 2D electrons with holes in the quasi-flat band region of valence band is found to be the most appropriate mechanisms. Note that a Mott like transition is inevitable whenever the net carrier density exceeds the critical Mott density in a particular region of sample. Either the spreading of 2DEG carriers towards the substrate or the enhancement of the density of photo-excited holes at AlGaN/GaN heterointerface or both are considered to explain the origin of a Mott like transition. Numerical simulations are also carried out to understand the generation of a Mott like transition in AlGaN/GaN heterostructures.

In **Chapter 5**, impact of Mg doping of GaN buffer layer on the optical properties of AlGaN/GaN HEMT structures is discussed by performing PL and SPS measurements on two samples. In these samples, initial 200 nm of GaN buffer layer is doped with different Mg concentration. Spectroscopic measurements are in perfect agreement with the growth changes made in the layer structures where Mg is seen to compensate the defects in GaN. Further, it is found that Mg doping of GaN buffer layer enhances the confinement of 2DEG in the triangular potential well at AlGaN/GaN heterointerface. Thus the spectroscopic methods discussed in this thesis are of special importance since the key properties of AlGaN/GaN HEMT structures can now be evaluated before the sample is transferred to the processing lab for device fabrication purpose.

Finally in **Chapter 6**, we conclude by summarizing the main results of the thesis with a brief discussions about the scope of future work. A new spectroscopic configuration of SPS technique is presented where measurements are performed under pump-probe geometry. The modified method is found to be very useful for measuring

the bandgap of semiconductor epitaxial layers which was otherwise difficult due to the dominance of sub bandgap features. It also helps in understanding the fundamental origin of defects in GaN epitaxial layers and AlGaN/GaN HEMT structures. Spectroscopic measurements reveal that Magnesium creates deep acceptor levels in heavily doped p-GaN layers which is associated with the observation of BL band in p-GaN. Similarly, formation of C_N-O_N defect complex in AlGaN/GaN HEMT structures is found to be the main mechanism for the observation of YL band. It is also observed that a large fraction of such defect states lie at undoped GaN/Fe-GaN interface. Next, an anomaly related to the association of some fine oscillations in PL spectra with the sub levels of 2DEG in AlGaN/GaN HEMT structures is resolved. It is found that the fine oscillatory features are governed by the interference phenomenon. Thereafter, a contactless method for finding an unambiguous signature of 2DEG in AlGaN/GaN HEMT structures is demonstrated. The proposed method is used to study the effect of Mg incorporation on the optical properties of AlGaN/GaN HEMT structures where Mg doping is found to compensate the native defects. Complimentary electronic transport measurements or the operational characteristics of HEMT devices made from AlGaN/GaN structures with variation in Mg content of GaN buffer layer are required to corroborate the spectroscopic results. Availability of this knowledge shall be highly beneficial in the development of next generation nitride devices.

References:

1. B. J. Baliga, Semiconductor Science and Technology **28** (7), 074011 (2013).
2. U. K. Mishra, L. Shen, T. E. Kazior and Y. F. Wu, Proceedings of the IEEE **96** (2), 287-305 (2008).
3. S. Nakamura, Semiconductor Science and Technology **14** (6), R27 (1999).

4. M. S. Shur and M. A. Khan, MRS Bulletin **22** (02), 44-50 (1997).
5. O. Ambacher, J. Smart, J. R. Shealy, N. G. Weimann, K. Chu, M. Murphy, W. J. Schaff, L. F. Eastman, R. Dimitrov, L. Wittmer, M. Stutzmann, W. Rieger and J. Hilsenbeck, Journal of Applied Physics **85** (6), 3222-3233 (1999).
6. M. A. Khan, M. S. Shur, Q. Chen and J. Kuznia, Electronics Letters **30** (25), 2175-2176 (1994).
7. M. Azize, Z. Bougrioua and P. Gibart, Journal of crystal growth **299** (1), 103-108 (2007).
8. Y. Cordier, M. Azize, N. Baron, Z. Bougrioua, S. Chenot, O. Tottereau, J. Massies and P. Gibart, Journal of Crystal Growth **310** (5), 948-954 (2008).
9. Y.-J. Lee, Y.-C. Yao, C.-Y. Huang, T.-Y. Lin, L.-L. Cheng, C.-Y. Liu, M.-T. Wang and J.-M. Hwang, Nanoscale Research Letters **9** (1), 433 (2014).
10. M. A. Reshchikov and H. Morkoç, Journal of Applied Physics **97** (6), 061301 (2005).
11. D. Demchenko, I. Diallo and M. Reshchikov, Physical review letters **110** (8), 087404 (2013).

Chapter 1

Introduction

Recent advancements in nitride semiconductor research have facilitated the development of wide range of power electronic devices, high efficiency white light emitters and solar/visible blind ultraviolet photodetectors.[1-11] One of the most important nitride device is high electron mobility transistor (HEMT).[12, 13] HEMT is a heterojunction based unipolar field effect transistor which utilizes the advantages of 2-dimensional electron gas (2DEG) to produce high gain at high frequencies along with low noise values. Since 2DEG is spatially separated from ionized donors/impurities, it experiences less ionized impurity scattering and therefore exhibit a high mobility.[14] A combination of high 2DEG density and high electron mobility results in high current density and low channel resistance, which are especially important for high frequency operation and power switching applications. In view of this, III-nitride heterostructures are capable of possess high 2DEG density along high electron mobility when compared with other semiconductor heterostructures. In addition to this, key material properties of nitride semiconductors are highly promising for the realization of high frequency, high temperature, and high power HEMT devices. Material properties of GaN are compared with other semiconducting materials in Table 1.1. High bandgap of GaN allows high breakdown field and high operating temperature which is beneficial over Si or GaAs in high power and high temperature applications.[15] High electron saturation velocity leads

to high saturation current density which in combination with high mobility makes GaN HEMT suitable for high frequency switching amplifiers. Though the breakdown field, saturation velocity and Johnson Figure of Merit (JFOM) are similar, the ability of GaN to form heterojunctions makes it superior to SiC. Nitride based HEMTs are now commonly used in military radar, satellite communication, wireless mobile communication, imaging and microwave oven which require high performance at high frequency levels.

Material / **Parameter**	**Si**	**GaAs**	**SiC**	**GaN**
Bandgap (eV)	1.1	1.42	3.25	3.49
Electron mobility(cm^2/V s)	1500	8500	700	1000
Saturation velocity (x 10^7 cm/s)	1	2	2	2.5
Breakdown field (MV/cm)	0.3	0.4	3	3.3
T_{max} (^oC)	300	300	600	700
JFOM	1	2.7	20	27.5
BFM	1	14.8	125.3	186.7

Table 1.1 A comparison of Material properties of various semiconductors [2, 13, 16, 17] Johnson Figure of Merit (JFOM) is a measure of the ultimate high frequency capability of the material where as Baliga's figure of merit (BFM) is a measure of the specific on-resistance of the drift region of a vertical FET.

1.1 A Brief History of III-Nitride HEMT

The first observation of 2DEG in AlGaN/GaN heterostructure was reported in 1992 by Khan *et al*.[18] The formation of 2DEG density of $10^{11}/cm^2$ due to strain induced polarization field in nitride heterostructure was shown by Bykhovski *et al.* in 1993.[19] At the same time, fabrication of AlGaN/GaN HEMT and its DC characteristics were reported by Khan *et al*.[6] whereas nitride HEMT were demonstrated in RF power amplification.[20, 21] However, in the initial stage, AlGaN/GaN HEMT devices suffered a high loss in output power at high frequency due to DC-to-RF dispersion. It is believed to be because of the trap assisted phenomenon where both the surface and bulk trap states contributes to current collapse.[22-24] Researchers had tried to overcome these limitations by incorporating several innovative ways. First, the passivation of surface states by SiN was introduced in 2000 which is found to effectively reduce DC-to RF dispersion to a certain extent.[25, 26] Second, field plate was adopted in AlGaN/GaN HEMTs which was found to increases the breakdown voltage of the device through modulating the electric field locally and also in reducing the dispersion.[27, 28] Third, insertion of a thin AlN layer before AlGaN growth was found to suppress current collapse by preventing 2DEG transfer to surface and bulk trap states.[29] It further reduced the alloy disorder scattering which affects the mobility of 2DEG. Efforts are made to achieve low leakage current and better pinch off condition by introducing a back barrier layer for 2DEG or by making the buffer layer semi-insulating.[30, 31] A better buffer isolation and high cut off frequency of the device is obtained using back barrier configuration. Since then, the output power density has further improved by optimizing growth techniques, material qualities, and device designs.[32-38]

1.2 Crystal Structure and Polarization

III-nitride usually crystalize in hexagonal wurtzite (WZ) type where the atoms are in tetrahedral atomic coordination with theoretical sp3-hybridization.[39] Stacking sequence of atoms in a GaN unit cell is shown in Fig. 1.1 (a). A large difference in electronegativity between Ga (1.81 Pauling unit) and N (3.04 Pauling unit) atoms leads to high ionicity in GaN.[40] It leads to the situation where centre of positive and negative charge of wurtzite nitride materials no longer coincides. Thus, both the bond angles and lengths are minutely distorted as the crystal relaxes into a new point of equilibrium and therefore tetrahedral symmetry breaks down. Such structural deformations induce spontaneous polarization (P_{SP}) along [0 0 0 1] direction.[41] In addition, GaN crystal is non-centrosymmetric along [0 0 0 1] direction. It therefore exhibits two different sequences of atomic layering in the two opposite directions: [0 0 0 1] and [0 0 0 -1]. As a consequence, two crystallographic polarities are observed in GaN as shown in Fig. 1.1 (b) and (c).[41, 42] In a crystal of finite dimension, all the dipoles are neutralized except those lying at the two surfaces. A free Ga-polar surface develops negative sheet charge while a N-polar surface develops a positive sheet charge. Thus a non-zero net electric field of the order of MV/cm exists in bulk nitride semiconductors. Such an electric field is naturally present in all the nitride epitaxial layers grown [0 0 0 1] direction. Another polarization appears in nitrides due to residual strain in the epilayer. Traditional bulk GaN growth techniques are extremely difficult due to the requirement of high temperature ~ 2500 K and high equilibrium N_2 pressure ~ 10,000 bar.[43] Due to unavailability of bulk GaN substrate, nitride semiconductor epilayers are generally grown on foreign substrates such as sapphire, Si or SiC which have a very different lattice

parameter and thermal expansion coefficient when compared with nitride semiconductors. Lattice and thermal expansion coefficient mismatch between the substrate and epitaxial layer introduces a certain amount of in-plane biaxial strain in

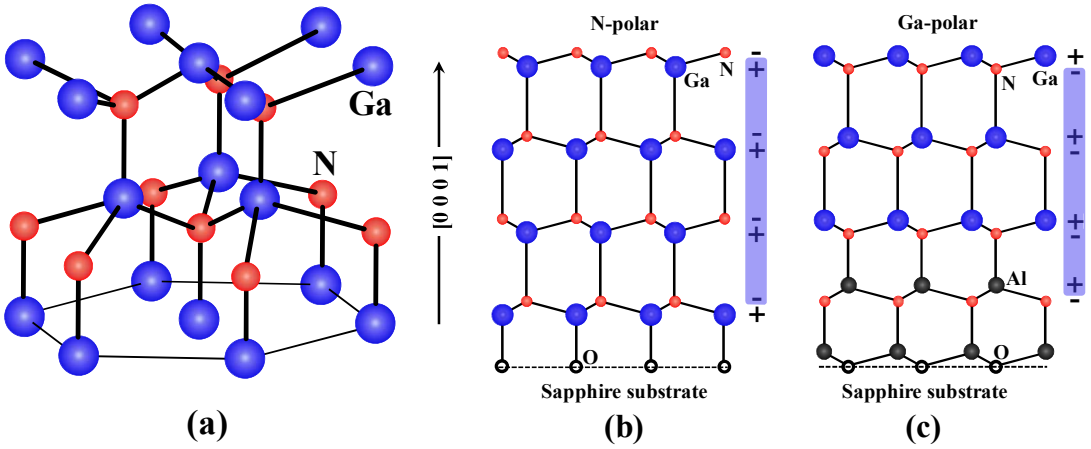

Figure 1.1 (a) Stacking of Ga and N atoms in (a) unit cell of wurtzite GaN and (b) along [0 0 0 1] direction in N-polar and (c) Ga-polar direction.

epilayer which results in a piezoelectric contribution to the polarization (P_{PZ}). Thus the resultant polarization in the material is given by;

$$\vec{P}_{tot} = \vec{P}_{SP} + \vec{P}_{PZ} \tag{1.1}$$

The direction of piezoelectric polarization depends on the type of stress that is present in epitaxial layer whereas the direction of spontaneous polarization depends on the polarity of epilayer. The polarity of epitaxial layer depends on the growth method, substrate preparation and also on the nature of buffer layer.[44] For example, both Ga-polar and N-polar GaN can be grown on sapphire substrate by molecular beam epitaxy technique. Sapphire substrate is oxygen terminated. The termination is found to be stable against nitridation for a considerable amount of time. Therefore, the first monolayer of deposited epitaxial film is Ga-monolayer. Since Ga-N bond is stronger than Ga-O bond, the first

Ga-monolayer belongs to GaN epitaxial layer. The epilayer therefore shows N-polarity as shown in Fig. 1.1(b). However, Ga-polar GaN is generally preferred because it favours two dimensional growth and displays better surface morphology. To get Ga-polar GaN, initially a thin layer of AlN is grown on sapphire substrate. The first deposited monolayer is Al-monolayer. Since Al-O bond is stronger than Al-N bond, the first Al-monolayer belongs to substrate. Thus the first grown N-monolayer belongs to the epitaxial layer. Thin AlN epitaxial layer therefore shows Al-polarity. GaN epitaxial layer grown on AlN layer shows Ga-polarity as shown in Fig. 1.1 (c). A selective polarity and corresponding polarization fields have very important implications in AlGaN/GaN HEMT structures and devices.

1.3 Polarization in AlGaN/GaN Heterostructures

A variation in structural parameters leads to different spontaneous polarization for AlN (-0.081 C/m^2), GaN (-0.029 C/m^2) and InN (-0.032 C/m^2).[42] In case of AlGaN/GaN heterostructure, the direction of spontaneous polarization is same however the magnitude is different in AlGaN and GaN epilayer. Further, AlGaN has a smaller lattice constant than GaN. Thus it results in a tensile strain in AlGaN layer which leads to piezoelectric polarization within AlGaN layer. The direction of spontaneous and piezoelectric polarization components in Ga-polar and N-polar AlGaN/GaN heterostructures is shown schematically in Fig. 1.2. GaN layer is considered to be relaxed due to which piezoelectric polarization in GaN layer is taken as zero. The net polarization discontinuity leads to large polarization sheet charge density which is defined by,[41]

$$\sigma = P_{SP}(AlGaN) + P_{PE}(AlGaN) - P_{SP}(GaN) \quad (1.2)$$

It is clear from the figure that both the spontaneous and piezoelectric polarizations are in same (opposite) direction in case of Ga-polar (N-polar) heterostructure. This leads to larger sheet charge density in case of Ga-polar heterostructure compared to N-polar heterostructure. The presence of polarization sheet charge is advantageous for the formation of 2-dimensional electron gas in case of AlGaN/GaN heterostructures.

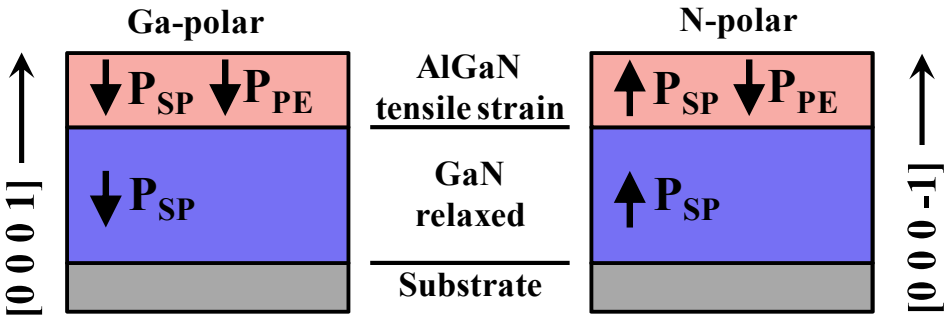

Figure 1.2 Polarization components in AlGaN/GaN heterostructure with different polarity. PSP and PPE stands for spontaneous and piezoelectric polarization respectively.

1.4 Formation of Two Dimensional Electron Gas in AlGaN/GaN Heterostructures

As mentioned earlier, key part of a HEMT devices is two-dimensional electron gas (2DEG) which is formed due to redistribution of charge carriers in a heterostructure.[14, 45] When a heterojunction is formed, redistribution of charge carriers occurs between the two materials until an equilibrium between the two Fermi levels is reached. The redistribution of charge carriers form depletion or accumulation region

within the heterostructure. Significant accumulation of free carriers leads to formation of a quasi-two dimensional triangular potential well. The quantum confined electrons are referred as 2DEG. A renowned advantage of AlGaN/GaN HEMT structure is that a large density of 2DEG (~10^{13}/cm^2) is formed at the heterointerface compared to ~10^{12}/cm^2 for modulation doped AlGaAs/GaAs HEMT structure.[14, 46, 47] Unlike AlGaAs/GaAs HEMT structure, the high 2DEG density is obtained even in case of unintentionally doped AlGaN/GaN HEMT structure. In fact, the 2DEG density doesn't follow the density of intentional dopants in AlGaN layer. Major reasons for the formation of 2DEG are

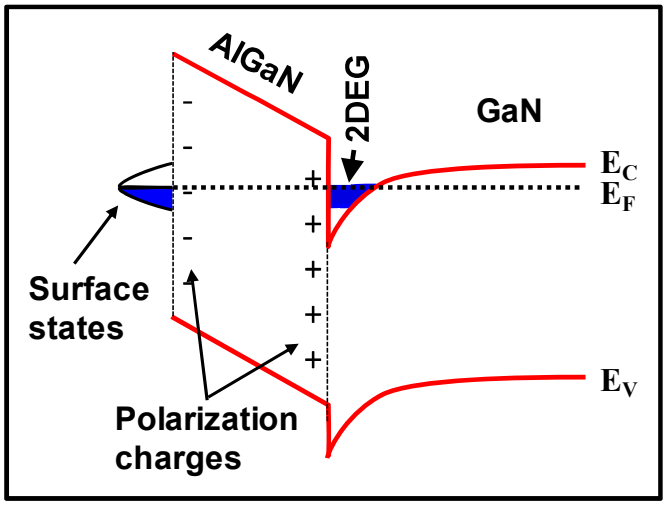

Figure 1.3 Schematic band diagram of AlGaN/GaN heterostructure. E_C, E_V and E_F corresponds to conduction band, valence band and Fermi level respectively.

associated with the presence of surface donor states and polarization induced charge sheet at the two faces of AlGaN layer as schematically shown in Fig. 1.3.[48, 49] A constant electric field exists in AlGaN layer due to the presence of polarization sheet charge at the top and bottom of AlGaN layer. This electric field increases the surface potential with increasing the thickness of AlGaN layer. On the other hand, there is a large density of donor states at AlGaN surface. For a small thickness of AlGaN layer, the surface donors

are well below the Fermi level and are expected to be filled. 2DEG also doesn't form because of no net charge transfer. With increasing thickness of AlGaN layer, the surface potential increases which moves surface donor states above the Fermi level as shown in Fig. 1.3. It leads to a large density of electrons transfer from AlGaN surface states to GaN which forms 2DEG at AlGaN/GaN heterointerface.[50] A partial screening of polarization field in AlGaN layer due to the charge transfer prohibits further rise of surface potential with increasing thickness of AlGaN layer. The advantage of nitride over arsenide HEMTs is that the modulation doping or large barrier width are not essential to form 2DEG. Further, a high band offset provides better confinement of 2DEG.

1.5 Ideal HEMT Characteristics

For an ideal HEMT, 2DEG is sharply confined at the heterointerface. The buffer layer is semi-insulating so that no current flows from source to drain in pinch off condition. Further, there are no traps present in the heterostructure which can capture 2DEG. The normal and pinch off condition of a HEMT are shown schematically in Fig. 1.4 (a) and (b) respectively whereas the schematic drain current (I_D)-source to drain voltage (V_{DS}) characteristics for different gate voltages (V_G) are shown in Fig 1.4 (c). Maximum drain current in normally on condition and zero current in pinch off condition provides maximum swing of drain current (I_{max}). The maximum swing of drain current (I_{max}) provides the maximum output power (P_{max}) which is given by,

$$P_{\max} = \frac{(V_{br} - V_{knee})I_{\max}}{8} \tag{1.3}$$

where, V_{br} and V_{knee} correspond to the breakdown voltage and knee voltage respectively. Drain current (I_{DS}) can be maximized by maximizing the density and mobility of 2DEG. 2DEG density can be maximized my increasing the total polarization discontinuity at the heterointerface whereas mobility can be maximized by improving the interface abruptness. Breakdown voltage (V_{br}) of GaN is high enough whereas V_{knee} can be reduced by reducing the channel resistance. Thus, an ideal AlGaN/GaN HEMT can produce high gain, which makes the transistor very useful for high power devices.

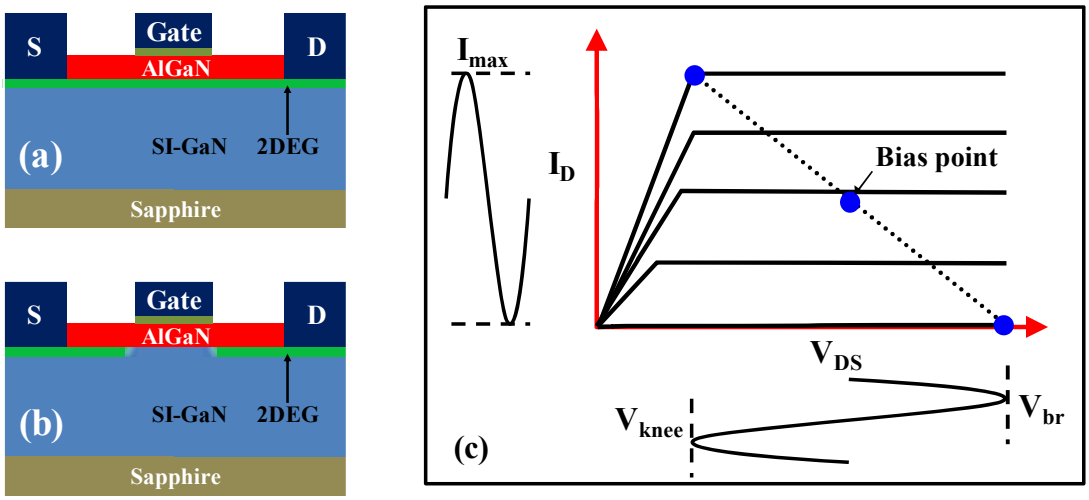

Figure 1.4 Schematic of an ideal AlGaN/GaN HEMT structure in (a) normal and (b) pinch off condition. S and D corresponds to source and drain respectively. Pinch off condition is obtained by applying bias which is not shown. (c) Schematic I-V characteristics of an ideal HEMT. I_{DS}, V_{DS}, V_{knee} and V_{br} corresponds to drain current source to drain voltage knee voltage and breakdown voltage respectively.

1.6 Non-idealities of GaN HEMT

Despite of several advantages, there are several limitations of AlGaN/GAN HEMT. In practical HEMT, 2DEG density is distributed in the buffer layer due to low

barrier height. Further, there are large number of traps lying near 2DEG channel, a reasonable background electron density in bulk GaN and charged dislocations lying at the substrate-epilayers interface as schematically shown in Fig. 1.5 (a) and (b). Presence

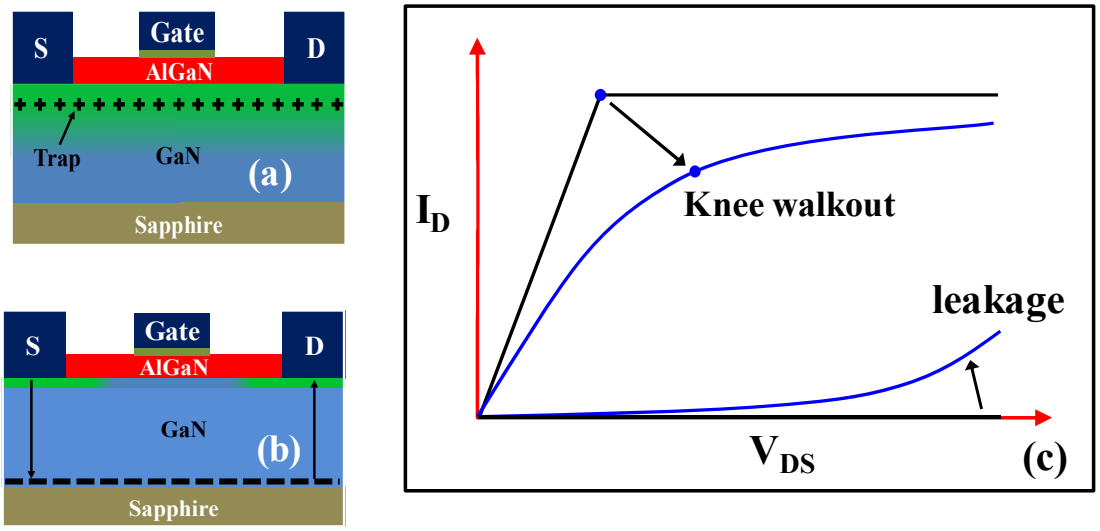

Figure 1.5 Schematic of a non-ideal AlGaN/GaN HEMT structure in (a) normal and (b) pinch off condition. S and D corresponds to source and drain respectively. (c) Schematic I-V characteristics of a non-ideal HEMT. I_{DS}, and V_{DS} correspond to drain-source current and drain-source voltage respectively. The ideal (non-ideal) curves are shown by black (blue) lines respectively along with the leakage current.[48, 51]

of traps and background carrier density degrade the performance of HEMTs in several ways. First, the spillover of 2DEG towards the substrate during HEMT operation leads to capture of hot electrons by the traps present near the channel region. It therefore reduces the effective density of 2DEG which leads to low drain current as schematically shown in Fig. 1.5 (c).[24, 51, 52] The effect is known as current collapse. In addition to this, the channel resistance also increases which leads to increase in knee voltage to higher value.[53] Second, in pinched off condition, a considerable amount of current conduction occurs through background carrier and interface charged dislocations as shown

schematically in Fig. 1.5 (b). It leads to an increase of the leakage current in off state condition as shown in Fig. 1.5 (c). Third, the frequency response of traps states is comparatively slow which lags the output response behind gate signal and also leads to large noise in the device.[52, 54-56] Thus in case of very high frequency swing of the gate voltage, the drain-to source voltage/ drain current does not follow the gate voltage swing which leads to low drain current. All these effects lead to low output power of HEMT. In order to optimize the HEMT performance, one therefore needs to minimize the defect density in HEMT structures.

1.7 Imperfections in GaN

As mentioned before, GaN epitaxial layers are generally grown on foreign substrates due to unavailability of bulk GaN substrate. Sapphire and Silicon are the most common substrates for GaN growth due to easy availability.[57, 58] However, the large lattice mismatch (13.8 % for Sapphire and 17 % for Si) and the difference in thermal expansion coefficient between the substrate and epitaxial layer introduce a large density of dislocations ($> 10^{10}$ cm^{-2}) in epitaxial layer.[7] These dislocations behave like efficient recombination and scattering centers. One method to reduce the dislocation density in active region is to grow a thick GaN buffer layer. However, it introduces large bow which brings difficulty in processing such as sub-micron lithography, inhomogeneous etching and polishing. Further, nominally undoped GaN grown on sapphire or Si substrate shows n-type conductivity due to unintentional doping by residual Oxygen or Silicon impurities. The substrate itself acts like a source of such impurities in the initial stage of growth. These unintentional impurities create shallow donor states within the bandgap which

contributes to a large density of background electron density.[59] A lot of work have been aimed towards the minimization of dislocation density and background electron density in GaN growth. Optimization of the growth process can help in reducing the defect density. However, carrier concentration at intrinsic level is difficult to obtain from the growth point of view. Another way to minimize the electron density is the compensation of residual donors by shallow and deep acceptor impurities such as carbon (C), iron (Fe) and magnesium (Mg).[34, 36, 60-62] However, the process of manufacturing a semi-insulating buffer can introduces excess traps in GaN buffer layer which can enhance current collapse and DC to RF dispersion. Hence, an innovative way for the minimization of trap states is essential. Fundamental understanding of the origin of defects in GaN can surely help in this process. A prior knowledge of the characteristics of defects can be extremely helpful in optimizing the performance of HEMT devices.

In view of this, optical spectroscopy is very attractive due to its capability of probing the heterostructures in truly non-destructive manner. Various spectroscopic techniques including Photoluminescence (PL), Photoluminescence Excitation (PLE), and Surface Photovoltage Spectroscopy (SPS) are extensively used to acquire the required information related to the band structure of bulk semiconductors, quantum confined energy levels and also the defect information.[63, 64] In the next section, dominant optical transitions related to band edge and defects in GaN and related heterostructures are discussed in brief.

1.8 Optical Transitions in GaN and AlGaN/GaN Heterostructure

GaN is a direct bandgap semiconductor material as elaborated by energy (E)-momentum (k) diagram in Fig. 1.6 (a). The minima of conduction band and the maxima of valence band coincide at k=0 (Γ point). Due to spin-orbit coupling and crystal field splitting, the valence band splits into three sub-bands A, B and C respectively.[65, 66] The conduction band has s-like atomic character whereas the three valence bands have p-like atomic character. It is possible to have electric dipole transition from each of the valence band to conduction band and vice versa. Absorption of a photon via interband transition creates electron and hole in the respective bands. The photo-excited carriers then relax to the lowest energy state in the bands via emission of acoustic and optical phonons. Due to opposite polarity of electron and hole, they experience a Coulomb attraction. When the attractive potential energy is higher than the thermal and kinetic energy of the individual charged particle, a bound electron-hole pair forms which is called an exciton. It is quite similar to a hydrogenic system. Applying Bohr model to exciton, the quantized energy levels relative to the ionization limit are given by,[67]

$$E(n) = -\frac{\mu}{m_0}\frac{1}{\varepsilon_r^2}\frac{R_X}{n^2} \tag{1.4}$$

where, μ is the reduced mass, m_0 is the mass of electron, ε_r is the dielectric constant of GaN, R_X is Rydberg constant of Hydrogen atom (13.6 eV), and n is the principal quantum number. Due to large dielectric constant (ε) ~ 8.9 of GaN, the electrostatic attraction between electron and hole is weak in GaN. Thus weakly bound Wannier-Mott exciton with energy ~26 meV are observed in GaN. Since the binding energy of exciton is

comparable to thermal energy at room temperature, exciton in GaN exists even at room temperature. Thus most of the photo-excited carriers in GaN goes through excitonic

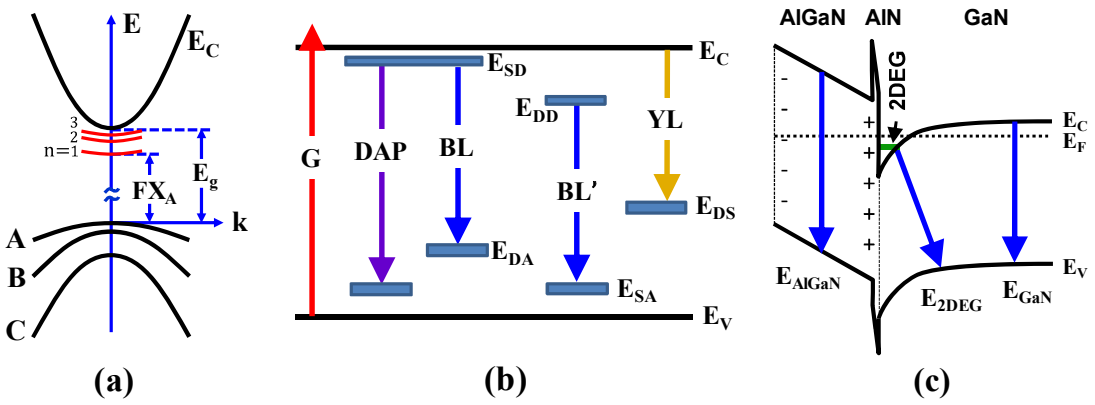

Figure 1.6 Schematic of (a) E-k diagram of GaN, (b) defect states and corresponding optical transitions in GaN, and (c) AlGaN/AlN/GaN heterostructure with optical transitions. A, B and C corresponds to three valence bands of GaN. E_g and FX_A correspond to bandgap of GaN and free exciton recombination energy respectively. E_C, E_V, E_F, E_{SD}, E_{DD}, E_{DA}, E_{SA}, and E_{DS} correspond to conduction band, valence band, Fermi level, shallow donor, deep donor, deep acceptor, shallow acceptor and deep state respectively. G, DAP, BL and YL corresponds optical generation, donor-acceptor pair recombination, blue luminescence and yellow luminescence respectively.

recombination (at 3.43 eV) below room temperature. In addition, there are dopants and impurity centers in GaN which attracts exciton via the van der Waals interaction. Due to this attraction, excitons are trapped by neutral donor impurity and thus forms bound excitons. Due to additional binding energy, bound excitonic transition occurs at energy lower than the energy of free excitons. Bound exciton emission is important for the characterization purposes because it provides a qualitative signature of defects that bounds the exciton. Dopants and impurities further create shallow and deep levels within the bandgap of GaN. Electrical characteristics of defects mainly depend on the energy

position within the bandgap. The states which lie in close vicinity of band edges (approximately < 3kT) are called shallow states. Thermal activation of carriers from these states is responsible for the background carrier density in respective bands. The states which lies deep in the bandgap are known as deep states. They do not contribute in conductivity, however, act as efficient carrier traps and recombination centers. The commonly observed shallow and deep states are shown schematically in Fig. 1.6 (b). After photo-excitation (G), the carriers get distributed in the bands and in defect states depending on their capture cross section and occupation probability. After a characteristic lifetime, photo-excited carriers undergo either radiative or non-radiative recombination. When the carriers are recombining radiatively, they create some luminescence corresponding to each transition. The transition energy provides information about the position of defect states within the bandgap whereas its intensity provides a qualitative density of defects. The defect related luminescence observed in GaN are also shown in Fig. 1.6 (b). Transition from shallow donor (E_{SD}) to shallow acceptor (E_{SA}) is called donor-acceptor pair (DAP) recombination which provides violet luminescence at ~ 3.27 eV.[68] The origin of blue luminescence (BL) is controversial where a transition from E_{SD} to a deep acceptor level or a deep donor level (E_{DD}) to E_{SA} is considered to be the probable transition.[63] On the other hand, yellow luminescence (YL) originates due to E_C/E_{SD} to a deep state (E_{DS}) transition where its correlation to a particular defect state is controversial.[63]

In case of AlGaN/GaN HEMT structures, all these defects are present in GaN buffer layer. Hence, band edge transition related to GaN, AlGaN along with defect related transitions are typically observed in AlGaN HEMT structures. In addition, there are quantum confined energy levels of 2DEG. After optical excitation, the 2DEG can

recombine with the photo-excited holes. The spatially indirect recombination generates a very low intensity luminescence at energy lower than the band edge transition as shown in Fig. 1.6 (c). Useful information related to the formation of 2DEG, electric field at the triangular potential, effective confinement of 2DEG can be approximated after careful analysis of luminescence spectra.

All the above mentioned signature of defects and 2DEG are obtained in case of radiative recombination. In case of non-radiation recombination, the emission based measurements are inefficient. However, one can resonantly excite the defects by tunable optical excitation and therefore can get information related to the defects. Excitation based spectroscopic techniques such as transmission and surface photovoltage spectroscopy (SPS) provides sufficient information about such defects.[64]

1.9 Literature Survey and Scope of Present Work

Advancements in the device performance depends significantly on the fundamental understanding of defects that are present in the active region of device. Efforts can be put to minimize the number of defects in layer once their origin is well established. It is therefore essential to probe the optical and electrical signatures associated with the point defects by different characterization techniques. The identification and characterization of dominant defects in GaN and AlGaN/GaN heterostructures by using various characterization techniques are reported by several researchers.[63, 69-76] A number of theoretical calculations are already reported on the defects in GaN. In spite of substantial research, there are several issues which are still under intense debate. For example, the

optical signature of dominant defects in GaN namely the blue luminescence (BL) and yellow luminescence (YL) are commonly observed in GaN epitaxial layers. The exact attribution of these luminescence features to specific defects in GaN, their spatial and spectral origin within the sample and impact on HEMT performance is not yet clear.[38, 75, 77-84] Various characterization tools and simulations approaches are already reported by numerous researchers over the last three decades that have been focused to identify the exact attribution of defects to these luminescence bands. For more than a decade, Gallium vacancy (V_{Ga}) related defects/ defect complex were considered as the source of YL band.[72, 85-89] Due to low formation energy, V_{Ga} defect centres are present in GaN bulk and epitaxial layers with typical concentration of 10^{17}-10^{18} cm^{-3}.[86] They further make complexes with carbon atom substituting the nitrogen (C_N)[72] or oxygen atom substituting nitrogen (O_N)[87] and form deep acceptor complex of energy E_V+0.87 eV. The radiative recombination between shallow donors such as oxygen (O) or Silicon (Si) and deep acceptor gives rise to YL band. A low activation energy of 15 meV estimated from the temperature dependence of YL matches reasonable well with the activation energy of shallow donors.[90-92] Later, a correlation of C-concentration with the deep acceptor state for YL have been occasionally appearing with the exclusion of V_{Ga} defect complex.[25, 53, 62, 63, 75, 77, 78, 93] In particular, Huber *et al.*[93] have shown that the intensity of YL band follows the concentration of carbon rather than V_{Ga}. Further, hybrid density functional calculations are performed by Reshchikov *et al.*[77] where it is found that V_{Ga} and its complexes have either higher formation energy or the thermodynamic transition level is too high above the valence band to contribute to YL. Furthermore, the formation energies of C_N-O_N deep donor complex and isolate C_N deep acceptors are found to be low energy and the corresponding thermodynamic transition levels matches well with the YL

transition as shown schematically in Fig. 1.7 (a). However, there is still some ambiguity in identifying which carbon related defects contribute to YL band in GaN. It is because the transition energies of both the defect complexes are predicted to be very close. The

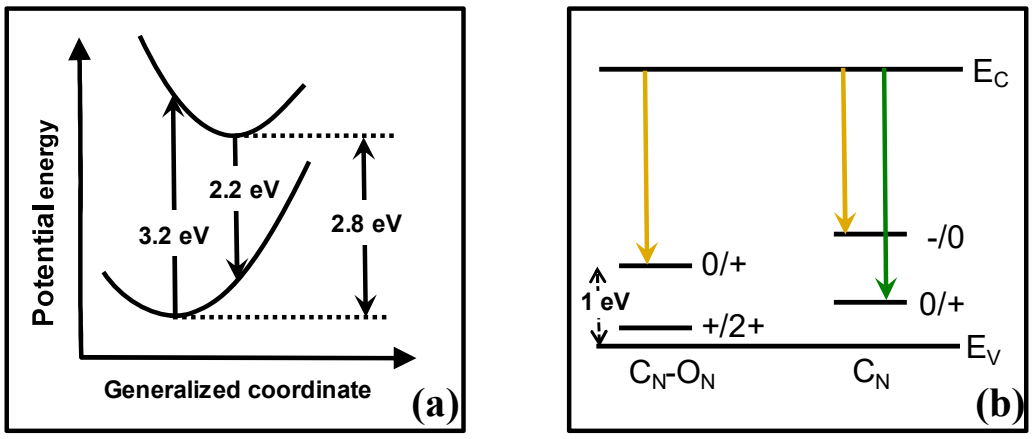

Figure 1.7 (a) Configuration coordinate diagram and corresponding optical transitions in C_N-O_N defect complex, (b) Schematic location of deep levels formed by different charge states of C_N-O_N and C_N deep defects within the bandgap of GaN.[77]

optical transition in these deep states are schematically shown in Fig. 1.7 (b). The resonant excitation in these defect complex occurs at 3.2 eV with zero phonon excitation at 2.8 eV. A luminescence feature occurs at 2.2 eV after a large lattice relaxation. Recently, Reshchikov *et al.*[77] have shown that the purity of GaN layer decides whether the mechanisms of YL band is governed by either isolated C_N defects or C_N-O_N defect complexes. The presence of a green luminescence (GL) band at a high excitation intensity is considered to be a firm confirmation of the dominance of isolated C_N defects in GaN. Several researchers have performed temperature and excitation intensity dependent measurements on YL to identify the recombination mechanism and spectral origin however they were unable to differentiate between the two carbon related defect complexes. Very recently, Huber *et al.* have found correlation between YL band and the

degradation of HEMT performance experimentally.[93] They have shown that the threshold voltage and drain to source onset resistance is correlated to the intensity of YL band. Note that the PL measurements were performed with 325 nm laser which is strongly absorbed within 100 nm of GaN layer. Thus it mainly correlates YL defects near to AlGaN/GaN interface with the degradation of HEMT. However, there may be dominant shallow and deep level defects lying very deep in the bulk of GaN which can contribute to leakage current and parallel conduction process.[36] It is therefore essential to identify the spatial distribution of YL related defects in GaN, however, the spatial location of YL band is highly controversial. There are several complementary reports which deals with the queries on whether YL is a surface or bulk property.[38, 83, 94-99] Cathodoluminescence measurements indicates that the YL band is spatially uniforms in a plane and its intensity is enhanced with increasing probe depth towards the substrate.[100-102] In contrast, Kelvin probe surface photovoltage spectroscopy measurements were performed by Shalish *et al.* where YL was reported to be a surface defect related phenomenon.[94] Furthermore, there are several reports which correlates the dominance of YL related point defects at the threading dislocation edges due to enhanced trapping by point defects.[87, 103, 104] On the contrary, there are several reports where people have performed selective area etching and island growth where YL density is found to be large near the dislocation free area which excludes the correlation of YL defects with threading dislocations.[88] Very recently, Matys et al. reported that the YL band arises from donor-acceptor pair (DAP) recombination in very limited regions of nanometre scale lying in the depletion region in the proximity of semiconductor surface.[84] Thus the experimental results are highly contradictory. It can be argued that the different observations appear

because of the limitations of a particular probing technique which is used in the identification and/or distribution of defects within the sample.

Similar to YL, the origin of blue luminescence (BL) in heavily magnesium (Mg) doped p-type GaN is also controversial.[76, 105-111] p-type GaN is an essential part of p-n junction based light emitting devices and bipolar junction based transistors. Mg is the only suitable acceptor dopant in GaN which creates a shallow acceptor level at about 200 meV above the valence band.[11, 68, 112] The radiative recombination of electron in shallow donor level with holes in shallow acceptor state contributes to donor acceptor pair (DAP) recombination at around 3.28 eV in low temperature PL spectra which is an evidence of the incorporation of Mg in GaN. While Mg is found to be an efficient p-type dopant in GaN, its applicability is limited by self-compensation effects at large concentration. A few reports are though available where a high value of p-type dopant concentration in GaN is measured,[113-117] Mg incorporation in p-GaN is poorly understood. In general, hole density increases with Mg incorporation up to ~ $10^{20}/cm^3$ and thereafter a gradual fall is seen at large Mg content.[118-121] A strong blue luminescence (BL) band in PL spectra appears in heavily doped p-GaN samples. In literature, there are two school of thoughts regarding the origin of BL band. According to model-1, which is mostly appreciated, a deep donor state is created at ~0.35 eV below the conduction band minima (E_C) which compensates holes in case of heavily doped p-GaN layers. The recombination of carriers between deep donor to shallow acceptor at E_V+0.2 eV is responsible for BL band.[109, 110, 122-124] Temperature dependent PL measurements provide an activation energy of 200 meV for BL band which corresponds to the thermal activation of holes from shallow acceptor level to the valence band. However, no firm signature of the involved deep donors is recorded in optically detected magnetic resonance experiments in case of

heavily doped p-GaN samples.[70] According to model-2, a deep acceptor level at 550 meV above the valence band is created in case of heavy doping. The recombination of electrons in conduction band with holes in deep acceptor level at E_V+0.55 eV are said to be responsible for BL band.[76] A low activation energy of 200 meV for BL band is explained by considering distributed density of states of the deep acceptor level towards the valence band. However, no confirmatory evidences were given for the energy position of particular deep defects/complex within the bandgap of GaN. Density functional theory predicts several defects such as nitrogen vacancy (V_N), interstitial Mg (Mg_i) and even Mg_{Ga}-V_N defect complex which can lead to the compensation mechanism. [113, 121, 125-128] Unfortunately, both the models are feasible in DFT which also creates some confusion. Very recently, Wahl *et al*. have performed ion implantation experiments to show that the incorporation of Mg in interstitial sites (Mg_i) increases in p-GaN epitaxial layer.[128] Further, Miceli *et al*.[121] have performed hybrid density functional calculations where they found that at high doping limit, the incorporation of Mg atoms in interstitial at the expense of substitutional Ga sites leads to the drop in hole density as observed experimentally. Furthermore, the charge transition in the aforementioned defects occurs near valence band rather than conduction band. Hence, an exact attribution to self-compensation effect and direct experimental evidence of the energy of deep levels associated with BL band are still unavailable. It makes the investigation of YL and BL bands as the two key areas where further efforts are essential.

Optical characterization of defects in wide bandgap semiconductor is preferred over electrical characterization due to contactless nature and ability to probe large activation energy which cannot be estimated by temperature dependent measurements. Techniques like Surface Photovoltage Spectroscopy (SPS), Photoluminescence (PL) and

Photoluminescence Excitation (PLE) spectroscopy are commonly used to characterize the defects in III-nitride epitaxial layers and heterostructures. Optical response of a defect depends on its density, absorption cross section/ emission probability and also on the occupation function of defect states. Conventional optical spectroscopy techniques therefore provide information about those states only where transition probability is nonzero in equilibrium. Furthermore, no depth resolved information can be obtained from conventional spectroscopic measurements. For example, in metal-insulator-semiconductor configuration of SPS technique, one measures the magnitude and phase to learn about the defects present in layer. Due to sub-bandgap optical excitation, the photovoltage can originate from sample surface, interface (if any) and from the back surface. However, one can't distinguish from which region the signal is originated. Note that the SPS signal due to a particular process can be negative or positive depending on the band bending in the field driven region.[129] Since the spatial location is not pinpointed by conventional SPS, no firm conclusion can be drawn from the phase of SPS signal. It therefore becomes difficult to know the nature of particular process contribution to SPS signal. Thus, one needs innovative way to identify the spectral and spatial origin of defect features within the sample.

As 2DEG is the heart of HEMT devices, identification of the presence of 2DEG in HEMT structures prior to the device fabrication is essential. The most confirmatory evidence for the presence of 2DEG is obtained from transport measurements. The evidence of high electron density from Hall measurements or observation of Subhnikov-de Hass oscillation in quantum hall experiment at low temperature confirms the formation of 2DEG in HEMT structure.[130-132] However, these are contact based method and needs liquid Helium temperature. In this context, spectroscopic technique can

provide useful information about the 2DEG in a truly non-destructive manner. Several researchers have used PL technique to characterize the presence of 2DEG in HEMT structures due to its contactless nature.[14, 45] The optical signature of 2DEG in AlGaN/GaN heterostructure was first reported by Shen et al.[45] A sharp feature (E_0) appeared below the free exciton edge (FX_A) of GaN as shown in Fig. 1.8(a). The feature showed a peculiar temperature and excitation intensity dependence which is different from genuine GaN excitonic or defect related features as shown in Fig. 1.8 (b) and (c) respectively. E_0 feature redshifts slower than FX_A with temperature for which the energy gap between exciton feature (FX_A) and E_0 decreases. Further, it shows a small blueshift with excitation intensity. The feature is assigned as spatially indirect recombination between 2DEG electrons with photo-excited holes. The transition appeared at lower energy than GaN band edge due to quantum confined Stark effect (QCSE). The temperature and excitation intensity dependencies are explained considering the thermal shrinkage of bandgap, screening of the electric field in potential well by thermal and photo-generated carriers.[45] Later on, other researchers also have performed spectroscopic

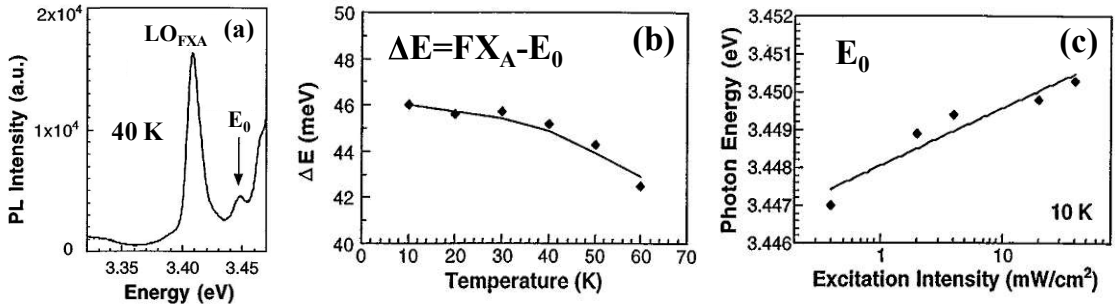

Figure 1.8 (a) 40 K PL spectra of AlGaN/GaN heterostructure, (b) temperature dependence of energy separation (ΔE) between 2DEG peak (E_0) from GaN free exciton (FX_A) emission, and (c) Excitation intensity dependence of E_0 at 10 K. LO_{FXA} corresponds to the 1st longitudinal phonon replica of free exciton-A.[45]

measurements on AlGaN/GaN HEMT structures where they found the appearance of several fine features in PL spectra.[133-138] These features were found to follow a similar temperature and excitation intensity dependencies as mentioned by Shen *et al*.[45] In spite of a large number of fine features, researchers had assigned them as the sub-levels of 2DEG. An electric field of 90 kV/cm at AlGaN/GaN heterointerface was estimated from the peak position of fine features.[136] On the contrary, a maximum of only two sub-levels are reported in literature from simulation and transport measurements.[131, 133, 139] These results indicate that there is ambiguity in true identification of 2DEG signature by optical spectroscopic technique which need to be carefully explored.

In this thesis, various spectroscopic techniques such as PL, PLE, reflectivity and SPV are used to identify and characterize the defects and 2DEG features in nitride epitaxial layers. In **chapter 2**, an introduction of the relevant techniques is briefly given before describing an innovative way of performing spectroscopic measurements under pump-probe configurations. It is shown to be extremely helpful in pinpointing the location of defects and to understand the associated electronic transitions. In **chapter 3**, the origin, spatial and spectral location of defects present in GaN epitaxial layer and AlGaN/GaN HEMT structures and their correlation to BL and YL is presented. In **chapter 4**, the main aim is to find an unambiguous identification of 2DEG signature in MBE grown AlGaN/AlN/GaN heterostructures. In **chapter 5**, the effect of Mg doping during initial growth of AlGaN/AlN/GaN HEMT structure on compensation of shallow and deep donors is studied by spectroscopic technique. In **chapter 6**, important results of the thesis are summarized.

Chapter 2

Experimental Techniques

2.1 Introduction

When a light beam falls on an optical medium, a part is reflected from the front surface while rest of the beam propagates through the material. During the propagation, light is attenuated by material due to the absorption process mediated by various electronic states. After travelling through the media, a fraction is reflected from the back surface while the remaining part is transmitted through the material. Optical response of a solid material is unique which can be probed by investigating its response to light via reflection, transmission and luminescence processes. Absorption of incident light excites electrons to high energy states in material. The electrons in excited state can then relax by emitting photons via a process known as photoluminescence. Optical characterization techniques can be used to investigate many aspects of semiconductor materials like electronic band structure including the bandgap, impurities, defects, and quantum confined energy states in case of low dimensional structures etc.[63, 64, 67, 140, 141]

This chapter focuses mainly on the spectroscopic characterization techniques that are extensively used during the course of this thesis. Important details of the spectroscopic characterization tools like Reflectivity (R), Photoluminescence (PL), photoluminescence excitation (PLE) and Surface Photovoltage Spectroscopy (SPS) are

presented in this chapter. A new modification in SPS technique is also presented which is found to be very useful in understanding the nature and location of defects in nitride semiconductor materials. It is based on a pump-probe configuration where an additional cw pump laser beam is used along with conventional SPS setup. Details of the experimental techniques, their applications, advantages and limitations are discussed in this chapter.

2.2 Reflectance Spectroscopy

Reflectance spectroscopy is based on measuring the amount of light reflected by the sample as a function of wavelength. Intensity ratio of reflected versus incident light beam gives the measure of Reflectivity or reflectance. All materials possess a complex index of refraction ($\tilde{n}$) given by,

$$\tilde{n} = n + ik \tag{2.1}$$

where n is the real part of refractive index and k is the extinction coefficient. In case of excitation to energy levels associated with the critical points in band structure, n and k shows a large variation at resonant excitation energy. Reflectivity for the normal incidence of incident light is defined by Fresnel equation,

$$R = \frac{(n-1)^2 + k^2}{(n+1)^2 + k^2} \tag{2.2}$$

which depends on both n and k. Thus reflectivity shows a sharp variation near resonant excitation energy and can be used to locate sharp energy levels such as excitonic transitions in semiconductor materials.[142, 143] Further the technique can be used to estimate the refractive index and thickness of sample. When the material is transparent

to optical excitation, the sample acts like a Fabry-Perot cavity where the excitation makes multiple reflections between the two interfaces i.e. air/layer and layer/substrate. Consider that a light beam of amplitude E_0 is incident upon a sample of thickness 'd' as shown in Fig. 2.1. A part of the light is reflected from sample surface whereas the rest of the light

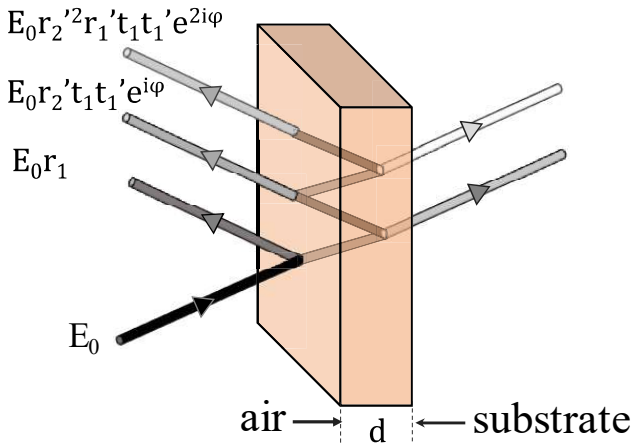

Figure 2.1 Schematic ray diagram to illustrate the multiple reflections and transmission within a transparent sample where d and E_0 correspond to the thickness of layer and amplitude of incident light respectively. r_1 (r_1'), and t_1 (t_1') correspond to reflection and transmission coefficients of air/layer surface when light is propagating from air to material (material to air) respectively. r_2' corresponds to reflection coefficient of layer/substrate interface.

is going to make multiple reflections within the cavity. Let r_1 (r_1') and t_1 (t_1') be the reflection and transmission coefficients of air/layer surface when light is propagating from air to layer (layer to air) respectively and r_2' be the reflection coefficient of layer/substrate interface. For normal incidence, the phase introduced due to a complete round trip travel (2d) in the cavity is given as follows,

$$\Phi = 2kd = \frac{4\pi nd}{\lambda} \tag{2.3}$$

where, k is the wave vector, n is the refractive index of GaN, and λ is the wavelength of the incident light. A few components of the reflected light are also shown in Fig. 2.1. The resultant reflected amplitude is given by,

$$E_r = E_0 r_1 + E_0 t_1 t_1' r_2' e^{i\Phi} + E_0 t_1 t_1' r_2'^2 r_1' e^{2i\Phi} + \ldots$$

$$= E_0 r_1 + E_0 t_1 t_1' r_2' e^{i\Phi}\left(1 + r_1' r_2' e^{i\Phi} + r_1'^2 r_2'^2 e^{i2\Phi} + \ldots\right)$$

$$= E_0 \left\{ r_1 + t_1 t_1' r_2' e^{i\Phi} \frac{1}{1 - r_1' r_2' e^{i\Phi}} \right\} \tag{2.4}$$

Using Stokes relation, $r_1' = -r_1$, $r_2' = -r_2$ and $r_1^2 + t_1 t_1' = 1$,

$$E_r = E_0 \frac{r_1 - r_2 e^{i\Phi}}{1 - r_1 r_2 e^{i\Phi}} \tag{2.5}$$

The reflected intensity is given by,

$$I_r = \left|E_r\right|^2$$

$$= E_0^2 \frac{r_1^2 + r_2^2 - 2 r_1 r_2 \cos\Phi}{1 + r_1^2 r_2^2 - 2 r_1 r_2 \cos\Phi} \tag{2.6}$$

Thus the intensity of reflected beam is considerably influenced by the interference phenomena where phase (Φ) carries the information of refractive index and thickness of sample. The value of thickness (refractive index dispersion) of sample can be accurately measured if the refractive index (thickness) of the material is known. Note that the absorption is considered to be negligible in our calculations which is a valid assumption in case of sub-bandgap excitation. Nevertheless, the absorption will cause a variation

only in intensity of the reflected light while the phase of reflectivity signal is expected to be invariant with respect to absorption in the material under investigation. Thus, the estimation of refractive index or thickness of the sample from phase dependence can easily be carried out even in presence of some absorption of sub-bandgap beam.

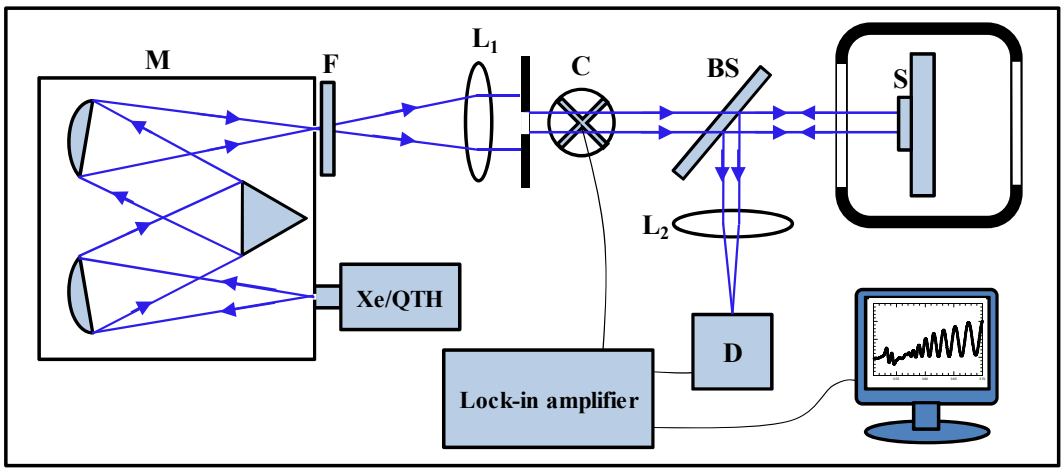

Figure 2.2 Schematic diagram of the reflectivity spectroscopy setup. Symbols M, F, L, C, BS, S and D corresponds to monochromator, long pass filter, lens, chopper, beam splitter sample and detector respectively.

A schematic diagram of the experimental setup used for reflectivity measurements is shown in Fig. 2.2. A 100 W Xenon/QTH lamp and a 0.32 m Horiba monochromator assembly is used as a tunable excitation source. The diverging beam from the monochromator is converted into a parallel beam with the help of a plano-convex lens. A small aperture of 2 mm diameter is used to pass a small portion of the incident light through it. The incident light then falls perpendicularly on the sample surface through a beam splitter. The sample is mounted on a Cu-plate which is placed in a closed cycle Helium cryostat. Reflected light is detected by a Silicon photo-detector. The measurements are done by using conventional lock-in technique. For spectral calibration, a spectrum is recorded by replacing the sample with an aluminium mirror

while other setup remains almost identical. Ratio of the reflectivity intensity in two consecutive measurements provides the reflectance spectra of sample.

Reflectance spectroscopy technique is used in this thesis to estimate the thickness and refractive index dispersion of AlGaN/GaN heterostructures samples studied in this thesis. It is used to distinguish genuine features of the sample from interference oscillations in PL spectra. In case of GaN, the exciton binding energy is as high as 26 meV.[66] Since excitons form discrete energy levels in the band structure, sharp features related to several excitonic transitions are observed in the reflectivity spectra of AlGaN/AlN/GaN epitaxial layers.

2.3 Photoluminescence Spectroscopy

Photoluminescence (PL) Spectroscopy is an emission based non-destructive technique to characterize the semiconductor materials and to study the dynamic processes that occurs subsequent to the excitation step. The technique is based on measurement of the energy distribution of emitted photons subsequent to optical excitation. The distribution of emitted photons is analysed in order to determine the optical quality of material, alloy composition, transition energy of involved states, layer thickness in case of quantum confined structures, recombination mechanism, emission efficiency and qualitative estimate of defect density etc.[63, 69, 144] A schematic diagram describing various upward and downward optical transitions that are possible in a bulk semiconductor material is given in Fig. 2.3. Optical excitation (G_1) with energy higher than the bandgap of material generates electrons and holes in the respective bands. Photo-excited carriers then relax to the lowest possible energy state in the bands via emission

of phonons. A fraction of the photo-excited carriers gets captured by the sub-bandgap states present within the material. After a particular characteristic time, photo-excited

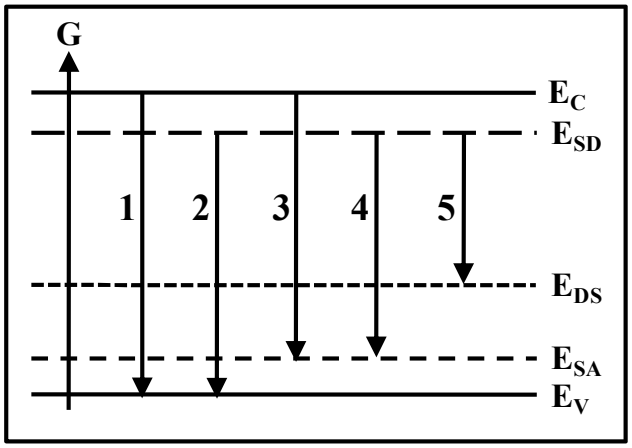

Figure 2.3 Schematic diagram showing various electronic transitions that are possible in a PL process. Symbols G, E_c, E_v, E_{SD}, E_{DS}, E_{SA} stand for excitation process, conduction band, valence band, shallow donor, deep traps, and shallow acceptor respectively.

carriers either in the band or in the sub-bandgap states recombine with holes leading to emission of photon via a process known as luminescence. Several downward transitions are possible such as band-to-band (1), excitonic, shallow donor-to-valence band (2), donor-acceptor pair (3), conduction band-to-shallow acceptor (4) and shallow donor-to-deep trap state (5) as schematically shown in Fig. 2.3. Spectral identification of PL features along with their relative luminescence efficiency provides useful information about the material under investigation. Figure 2.4 shows the schematic diagram of experimental setup used for PL measurements. A 12 mW 325 nm He-Cd cw laser is used to excite the samples. Samples are mounted on a copper holder placed in a closed cycle Helium cryostat which can cool down up to 10 K. The luminescence generated in the sample is collected by a 0.25m Sciencetech/0.5m Horiba monochromator via lens

assembly. An appropriate long pass filter is used to block the laser before it gets into the monochromator. The dispersed luminescence is recorded by photomultiplier tube (CCD) detector using lock-in (dc measurement) technique. A mechanical chopper is used in synchronization with lock-in amplifier. For intensity dependent PL measurements, a circularly variable neutral density filter is also used.

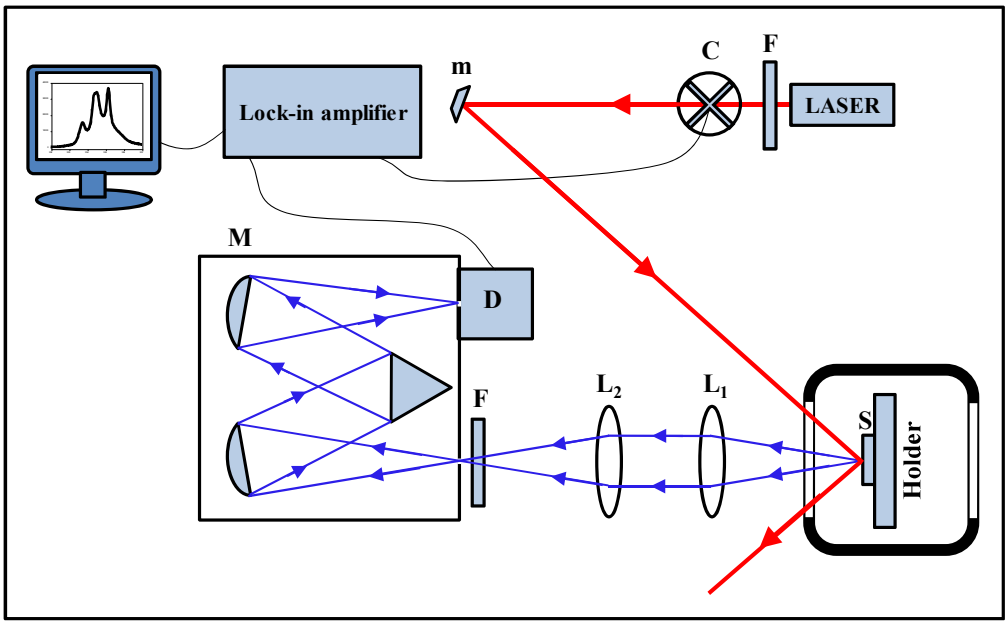

Figure 2.4 Schematic diagram of a photoluminescence spectroscopy setup where symbols C, F, m, L, D, M and S stand for mechanical chopper, optical filter, mirror, lens, detector, monochromator and sample respectively.

PL is an attractive technique for studying direct band gap semiconductor materials where useful information about various electronic states can be obtained in a truly non-destructive manner. During the course of this thesis, PL spectroscopy is extensively used to identify the signature of 2-dimensional electron gas (2DEG) in AlGaN/GaN heterostructures. 2DEG related features are uniquely distinguished from interference oscillations and defect related PL features. Several band edge, excitonic and

defect related PL features are also identified in GaN epitaxial layers and AlGaN/GaN heterostructures.

2.4 Photoluminescence Excitation Spectroscopy

Photoluminescence excitation spectroscopy (PLE) is an important technique which can provide useful information related to fundamental electronic transitions in material similar to absorption technique. However, the information is obtained in an indirect manner where the fundamental origin of a PL peak is probed by varying the energy of excitation beam. In case of quantum structures, PLE is preferred over absorption technique since features related to the absorption process can easily be detected which is rather difficult in case of conventional transmission measurements due to a very small interaction length. In case of absorption spectroscopy, there are several limitations like minimum sample thickness, transparency of substrate, presence of low bandgap interlayer etc. On the contrary, one doesn't need to meet such stringent criterion in PLE where selective absorption transitions which contribute to a particular PL feature are investigated. First, PL measurements are performed on the sample. After this, the detection spectrometer is set to the peak energy of PL feature while the excitation energy is scanned in order to record the PLE spectrum. For example, consider PL signal generation due to shallow donor to deep trap state transition as shown by transition 5 in Fig. 2.3. Here, the involved steps are excitation of electrons to the conduction band, relaxation of carriers to the lowest energy in respective bands, capture of photo-excited electrons (holes) by shallow donor (deep trap) state and recombination of electrons with holes. Note that the same PL feature also can originate due to a resonant excitation from

the E_V to E_{SD}. A PLE measurement at feature-5 will therefore tell whether its origin is associated with excitation to E_C or E_{SD} as shown in Fig. 2.3.

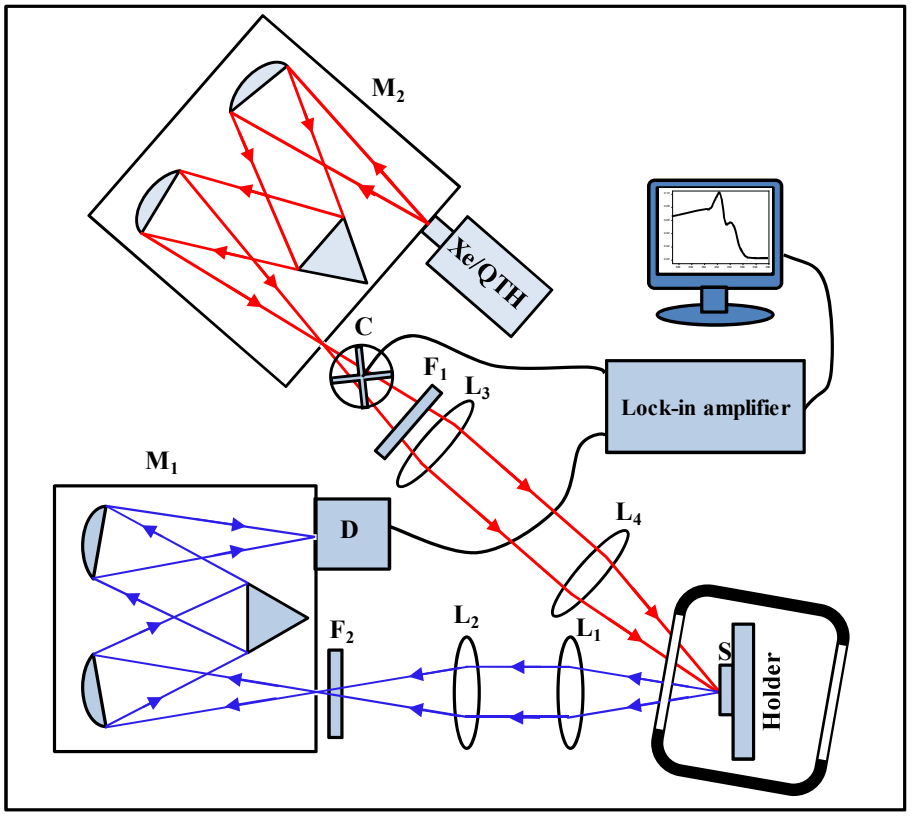

Figure 2.5 Schematic diagram of a PLE setup where symbols C, F, M, L, D, S, and Xe/QTH stand for mechanical chopper, optical filter, mirror, lens, detector, sample, and Xenon/quartz tungsten halogen lamp respectively.

A schematic diagram of PLE setup is shown in Fig. 2.5. Experimental setup is similar to PL setup except the excitation laser is replaced by a tunable light source. A Xe lamp and 0.32m Horiba monochromator assembly is used as the excitation source. The light is focused on the sample with the help of lenses. A suitable long pass filter is used to block the second order diffracted light from the monochromator. A mechanical chopper and lock-in are used for ac measurement. PLE is advantageous over PL technique in the sense that it can probe excited states of quantum structures which are

not generally observed in PL spectrum. During the course of this thesis, PLE technique is effectively used to distinguish 2DEG related PL features from the interface trap states. It is also used to find the energy and spatial location of defects states contributing to the well-known yellow luminescence band in AlGaN/GaN heterostructures.

2.5 Surface Photovoltage Spectroscopy

Surface Photovoltage spectroscopy (SPS) is a well-established non-destructive technique to study the optoelectronic property of bulk, multilayer and nanostructure semiconductors.[64, 94, 95, 129, 145-149] The technique relies on the illumination induced change in surface potential distribution of a given semiconductor structure due to redistribution of photo-excited carriers. The change in surface potential as a function of excitation energy gives SPS spectrum. A strong sensitivity of surface and/or interface band bending to light illumination allows the SPS technique in exploring the information related to band edge, quantum confined energy states in low dimensional semiconductors[144, 150, 151] and defect states which are present either at surface or in the bulk of sample.[64, 95, 152] An advantage of SPS technique over conventional absorption technique is that the band edge related information of thick sample and energy states with very low absorption cross section can be identified successfully. Further no lapping or polishing of the back surface of sample, which is essential in case of transmission spectroscopy in order to reduce scattering losses, is required.[153-155] Moreover, absorption spectroscopy fails to provide any information about the bandgap of epitaxial layers grown on absorbing substrates, for example, AlGaAs grown on GaAs which is not an issue in case of SPS technique. When compared with PL and PLE spectroscopy, where no or weak PL signal is recorded in

case of indirect bandgap materials, SPS technique can provide useful information related to the bandgap of those materials too. SPV thus offers the possibility of performing contactless and non-destructive spectroscopy measurements on a wide variety of semiconductor samples.

Fundamental mechanism of SPS technique is discussed in this section. The boundary between two media of different physical properties is defined as interface.[64] When one of two media is air then it is called surface. A termination of the periodicity at surface creates localized electronic energy levels within the forbidden gap of semiconductor. Thermal equilibrium between the surface and bulk states requires free carrier redistribution which creates a charge depletion or accumulation region near the surface/interface. A schematic of the band diagram near surface is shown in Fig. 2.6 (a) for n-type semiconductor. A depletion region is formed near the surface due to the transfer of electrons from bulk to surface states. The potential developed at the surface under equilibrium conditions is known as surface potential (V_S). When an above bandgap illumination is incident on sample, electrons and holes are created in the respective bands within the penetration depth. Electrons and holes are then spatially separated in opposite directions under the influence of built-in electric field in the depletion region as shown in Fig. 2.6. Spatial separation of electrons and holes generates an electric field which is opposite to the built-in electric field. It therefore reduces the surface potential which is essentially a measure of surface photovoltage (SPV). Thus SPV depends on the absorption of incident illumination in the depletion region of sample. Absorption of incident illumination depends on the absorption coefficient (α) of material which is a function of wavelength (λ) of incident illumination. Thus under certain criterion, SPV is proportional to absorption coefficient which is given by,[149]

$$SPV \approx \frac{\alpha}{h\nu} \tag{2.7}$$

Hence band edge related information can be easily estimated from SPV measurements. SPV can also be generated in the flat band region and field driven region other than the space charge region lying at the surface of sample. In case of optical excitation in semi-insulating semiconductor materials, no illumination induced change in the surface potential is expected due to the negligible surface band bending as shown schematically in Fig. 2.6 (b). Therefore, no SPV signal is expected for such materials. However, strong SPV signal is measured for those materials which originates due to Dember process.[152, 156] Figure 2.6 (b) shows the SPS generation mechanism via Dember process. In case of

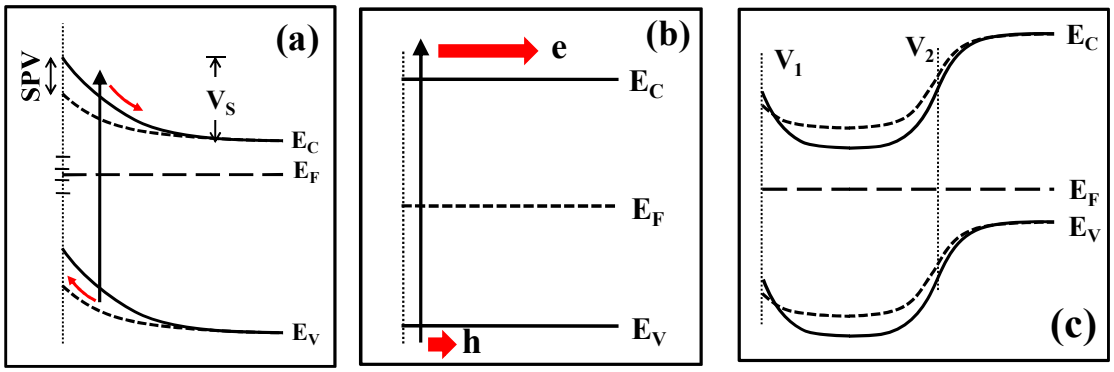

Figure 2.6 Schematic band diagram of (a) n-type semiconductors, (b) semi-insulating semiconductor, and (c) a p-n junction under dark (solid lines) and light illumination (short dashed lines) condition. Symbols Vs, E_C, E_F, and E_V E_{DS}, E_{SA} stand for surface potential (bend bending), conduction band, Fermi level and valence band respectively.

above-bandgap excitation, the density of photo-generated carrier exponentially decreases along the sample depth. Such carriers diffuse into the bulk which is driven by the density gradient of carriers. Significant difference in the mobility of carriers of opposite polarity causes a spatial separation of photo-generated carriers. The charge separation develops a

potential in the quasi-neutral region of semiconductor material which is known as Dember potential. In case of multilayer structure, there exists several field driven regions near the surface and interfaces. Typical schematic band diagram of a p-n junction is shown in Fig. 2.6 (c). A field driven region exists at the surface whereas another field driven region exists at the interface. When the interface is within the penetration depth, significant SPV contribution can arise from the interface field driven region also. The resultant SPV at a particular energy therefore correspond to the algebraic sum of all the SPV components generated by various processes at different spatial depth in the sample.

SPV processes discussed so far are activated by the above bandgap excitation. However, SPV can also be generated due to defect assisted transitions in the sub-bandgap region of semiconductor material. Note that the defect states that are present either on the surface or in the field driven region of bulk material can significantly change the surface potential depending on the absorption cross section and carrier redistribution mechanisms. Figure 2.7 (a) and (b) schematically describe the SPV generation mechanism due to sub-bandgap absorption by the gap states which are assumed to be present in the depletion region of an n-type semiconductor. In case (a), subsequent to photo-excitation, electrons are trapped by deep trap states (E_{DS}) and holes are free to move in valence band (E_V) as schematically shown in Fig. 2.7 (a). These holes are swept to the semiconductor surface under built-in electric field where they are captured by the surface states. Capture of electrons by the deep trap states lying in depletion region leads to a macroscopic field which is opposite to the built-in electric field.[129] It therefore reduces the surface band bending similar to band-to-band transition as schematically shown in Fig. 2.7 (a). On the other hand, when holes are trapped by the defect states lying in the depletion region, a rise in the surface band bending is expected as schematically

shown in Fig. 2.7 (b). Thus, the sign of SPV is expected to be opposite for the two cases related to the defect associated transitions shown in Fig. 2.7. Therefore, defect states can be probed in a non-destructive manner using SPS technique.

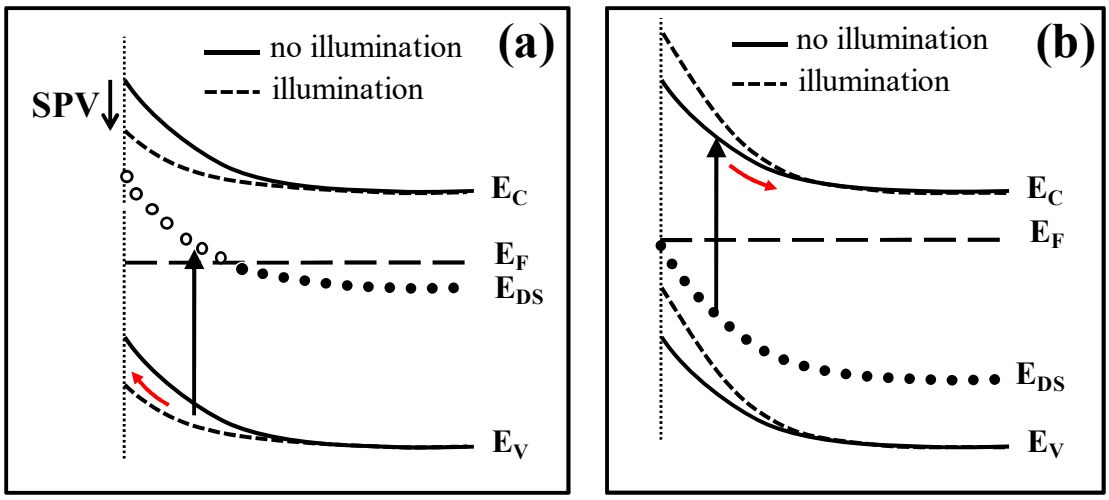

Figure 2.7 Schematic diagram of n-type semiconductor showing (a) valence band to trap and (b) trap to conduction band transition. The symbols E_C, E_F, and E_V corresponds to conduction band, Fermi level and valence band respectively.

2.5.1 Experimental configuration of SPS measurements

Surface potential is a built-in potential which is developed due to the redistribution of carrier between the surface and bulk states. Note that the Fermi level lie at the same energy at front and back surface of the sample under equilibrium conditions. Therefore, surface potential can't be measured directly with the help of a voltmeter. Consequently, several novel techniques have emerged to measure the surface potential. Two most common techniques are a) Kelvin probe method and b) Metal-insulator-semiconductor (MIS) configuration.[64] The two methods are briefly described in the following section.

2.5.1.1 Kelvin Probe Method

Kelvin probe SPS technique is based on the measurement of optical illumination induced changes in surface work function of a semiconductor under continuous exposure scheme. A metal grid is used as a reference electrode to measure the change in work function. Metal grid and semiconductor surface form a parallel plate capacitor. A schematic band diagram is shown in Fig. 2.8 to explain the generation of SPS signal in Kelvin probe method. When metal is short-circuited to semiconductor surface, charge redistribution occurs until an equilibrium of Fermi level between the two is reached as shown in Fig. 2.8 (a). This charge transfer results in an electric field and a drop in the local vacuum level between the metal and semiconductor across the gap. The drop of potential is equal to the difference in work function of metal (Φ_M) and semiconductor surface (Φ_S) as can be appreciated from Fig. 2.8 (a). The potential drop is usually known as the contact potential difference (CPD). A method of measuring the CPD was suggested by Lord Kelvin where an external bias is applied between the metal and semiconductor to nullify the contact potential difference as shown in Fig. 2.8 (b). When external dc bias (V_{null}) is equal and opposite to CPD, semiconductor surface and metal share a common vacuum level. In this situation, no charge transfer takes place between metal and semiconductor surface and therefore no field develops across the capacitor. Thus the dc applied bias at which no charge transfer takes place corresponds to CPD. Further, a change in the gap alters the overall capacitance of circuit which leads to the variation of voltage across the gap ($\Delta V=Q/\Delta C$) and hence a current in external circuit. Thus, CPD can be easily estimated by measuring the dc applied bias for which no external current is observed by changing the spacing between the plates as shown in Fig. 2.8 (b). When an external illumination is incident on sample, bend bending in semiconductor changes

which modifies the work function as shown in Fig. 2.8 (c). Such a change in work function is equal to the change in CPD which is a measure of SPV,

$$q\Delta SPV=\Delta W=q\Delta CPD \tag{2.8}$$

Thus, SPV be measured by applying a dc bias (V_{null}+SPV) for which external current is zero in presence of illumination.

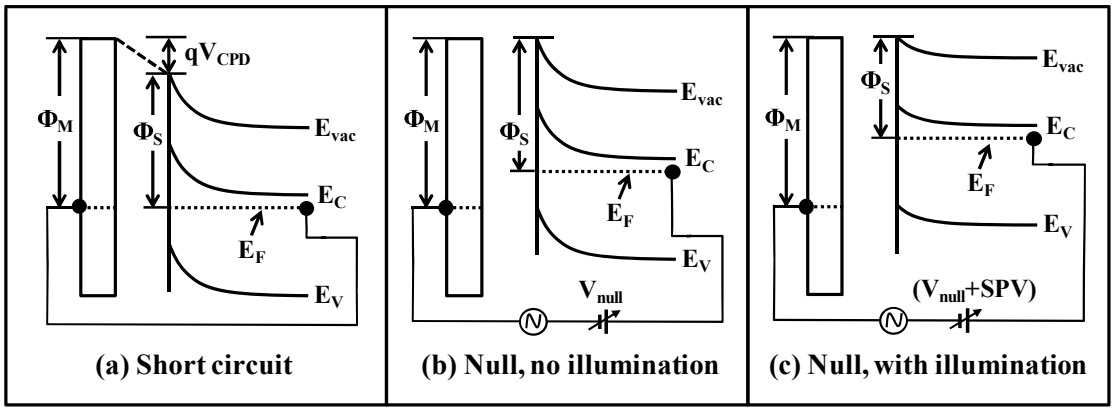

Figure 2.8 Schematic diagram to describe the mechanism of generation of SPV signal in Kelvin probe method, a) short circuit, b) under dark, and c) under illumination. The symbols Φ_M, Φ_S, V_{CPD}, E_{vac}, E_C, E_F, and E_V corresponds to work function of metal, work function of semiconductor, contact potential difference, vacuum level, conduction band, Fermi level and valence band respectively.

2.5.2.2 Metal Insulator Semiconductor Configuration of SPS

Metal-insulator-semiconductor (MIS) configuration is an alternative method for measuring SPV signal. In this technique, a metal grid or a transparent conducting plate is kept in soft contact with the sample.[64, 149, 157] Optical excitation induced changes in the surface potential are capacitively coupled via the transparent conductive probe. Thus,

SPV signal can be measured by recording the photo-induced changes in voltage at the transparent electrode. Note that an insulating air gap is present between the transparent plate and semiconductor surface which reduces the capacitive coupling between the two. As a result, the measured SPV signal is significantly lower than the actual change in surface potential. Such a low voltage is difficult to be measured with the help of a conventional voltmeter. Thus for steady state measurements, the optical excitation is periodically chopped at a given rate and SPV signal is detected with the help of a lock-in amplifier.

Both the SPS measurement techniques have their pros and cons and it is solely up to the choice of an individual which primarily depend on the application/ interest. Kelvin probe method is widely used in semiconductor industry for mapping various wafers. In case of Kelvin probe SPS measurements, one measures dc illumination induced change is surface potential where all the surface states with different time constants are expected to contribute to SPV. The SPV which is proportional to effective density of photo-generated carriers (n_{photo}) for a given excitation intensity (I) is given by,

$$SPV \approx n_{photo} \approx \frac{I(1-R)\alpha\tau}{h\nu} \tag{2.9}$$

Where, I, R, α, τ and hν are the intensity of incident illumination, reflectivity of the sample, absorption coefficient of the material, time constant of a particular SPV process and energy of the incident illumination respectively. Thus the states having longer time constant will contribute more to the SPV signal. Thus, kelvin probe SPS is largely sensitive to surface states which involves a long time constant of the order of millisecond to hours.[64] In case of MIS measurements, one measures the ac illumination induced changes in surface potential. The excitation beam is modulated by a mechanical chopper

at a certain frequency (f). The defects, which have longer response time than the time period ($T=1/2\pi f$) of modulated excitation, will not be able to respond and therefore will not contribute to SPV. Thus it put a cut off time constant below which the states are assigned to be 'fast' and therefore contributes to SPV and above which the states are assigned to be slow and therefore does not contribute to SPV. MIS configuration is therefore more suitable for characterization of bulk related optical transitions which involves fast relaxation phenomena. Another important advantage of MIS structure is that Ohmic back contact, which is crucial for Kelvin probe method, can be replaced by contactless capacitive coupling for example by mounting the sample on a conducting plate. On the other hand, accurate estimation of surface potential can be obtained by using Kelvin probe method where MIS only provide relative variation. During the course of this thesis, SPS measurements are performed under MIS configuration.

Schematic experimental setup used for MIS SPS measurements is shown in Fig. 2.9. A 100W Xenon/ QTH lamp is used as a tunable excitation source. A 0.32m Horiba IHR320 monocromator is used to disperse the incident illumination. A suitable long pass filter is used depending on the scan range to block higher order diffractions from the monochromator grating. Sample is mounted on a copper base plate which acts as a ground electrode. The change in the surface potential is picked up by a transparent conducting quartz glass plate coated with indium–tin–oxide (ITO) which is kept in soft contact with the sample surface. The measurements are performed in chopped light geometry where incident light is chopped by a mechanical chopper at a certain frequency. SPV signal is detected by lock-in at the same chopping frequency. For modulation frequency dependent SPS measurement chopping frequency is varied from 10 Hz to 3 kHz. To exclude any other features coming from substrate or instrument, SPS

measurements are also performed on bare sapphire substrate with identical experimental conditions. SPS technique is extensively used in this thesis to identify and characterize different semiconductor epitaxial layers and AlGaN/AlN/GaN heterostructures.

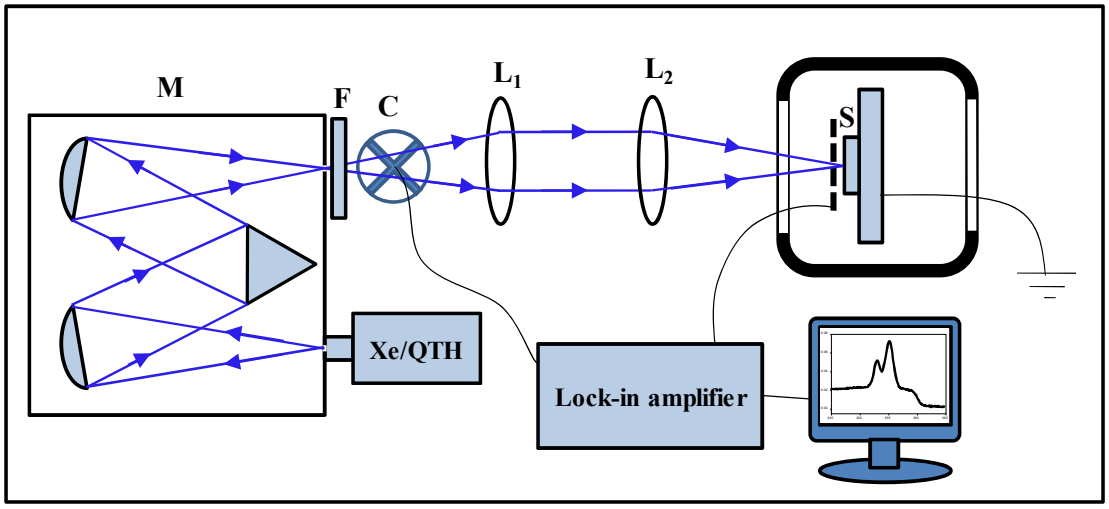

Figure 2.9 Schematic diagram of the SPS measurement setup. L, F, TCG, and S stand for the focusing Lens, order sorting Filter, Transparent Conducting Glass, and Sample, respectively. Pump beam is either a laser or an assembly of Xenon arc-lamp and a monochromator.

2.6 Pump-probe SPS Measurements: A New Configuration for Probing Heterointerface

As explained in the previous section, SPV not only depends on absorption coefficient but also on the response time of particular transition and carrier redistribution mechanisms. Thus, it is largely sensitive to the sub-bandgap states present at surface and in the bulk of semiconductor material. SPS spectrum therefore is much more complicated than the absorption spectrum. Due to this, the bandgap estimation using SPS technique becomes tedious whenever shallow sub-bandgap features mask the band edge feature.

Several tricks have already been suggested to resolve this issue. SPS measurements at high chopping frequency, or at high temperature are used to get rid of the contribution of sub-bandgap transitions.[157] Freshly cleaved surfaces with low recombination velocity were used by Cavalcoli *et al.* to get band edge related information of CdZnTe samples.[155] In spite of this, the information is not accessible in a few cases. It is therefore essential to look for a new method where one can suppress the effect of localized sub-bandgap states considerably and can measure the bandgap accurately. On the other hand, the characterization of defect states becomes tedious due to uncertainty in their spatial location within the sample and also the dominance of band edge feature. In this chapter, we present SPS measurements in pump-probe configuration which can be used not only for accurate bandgap measurement but also to characterize defect states in heterostructures. In this method, a cw sub-bandgap or above bandgap pump laser beam is incident on sample along with the conventional SPS setup as shown in Fig. 2.10. Energy of pump laser beam is chosen in such a way that it can selectively suppress particular SPS feature(s) and therefore enhances the visibility of feature of interest. For example, SPS magnitude spectrum of p-GaAs/SI-GaAs epitaxial layer is shown in Fig. 2.11 (curve a). The contribution of sub-bandgap SPS features is seen above 0.7 eV up to the bandgap of GaAs in conventional SPS spectra. Bandgap feature of GaAs is masked by a strong contribution of sub-bandgap states due to which an accurate measurement of bandgap is not possible. To get an accurate measurement of the band edge, pump-probe SPS measurements are performed on the sample with a CW 100 mW 1064 nm laser as pump beam and the spectrum is shown in Fig. 2.11 (curve b). Energy of pump laser (1.16 eV) is chosen on the basis that it can resonantly excite the deep trap states throughout the sample. It is clearly noticed that the sub-bandgap features are largely

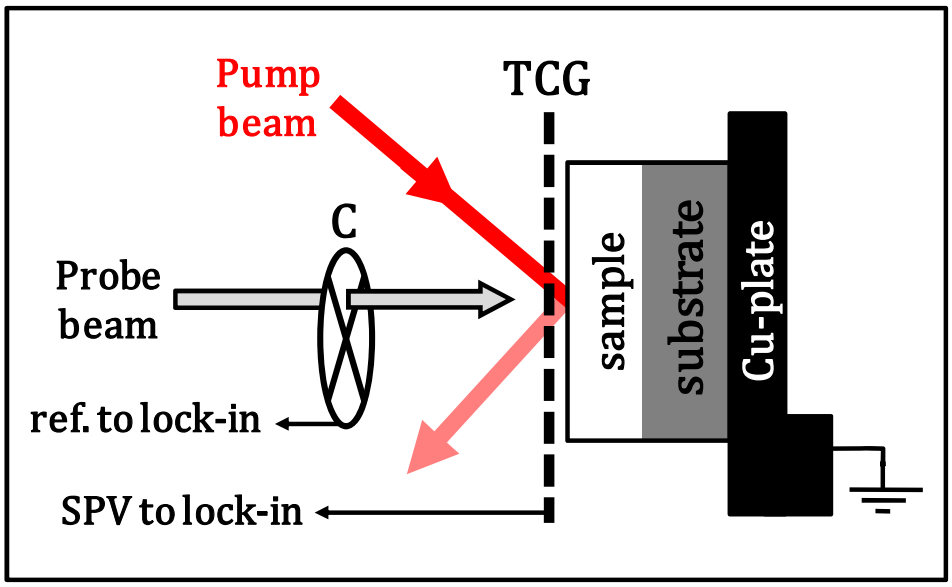

Figure 2.10 Schematic diagram of the pump-probe SPS measurement setup. Symbol TCG and C stand for transparent conducting glass and chopper respectively. Pump beam is either a laser or an assembly of Xenon arc-lamp and a monochromator.

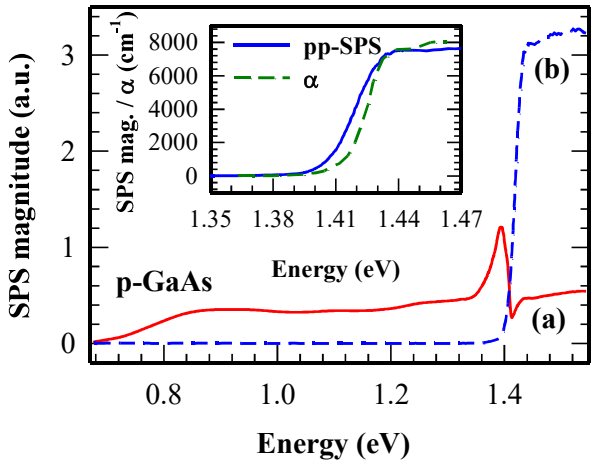

Figure 2.11 SPS magnitude spectra and (b) pp-SPS magnitude with 1064 nm laser spectra of p-GaAs/SI-GaAs at 28 Hz chopping frequency. Inset shows the comparison of pp-SPS and absorption spectra of GaAs over the same spectral range. The pp-SPS spectra is normalized with the value of α at 1.45 eV for comparison purpose.[158]

suppressed and a distinct feature related to the bandgap of GaAs is observed. It is interesting to observe that pump-probe SPS curve reasonably follows the variation of the

absorption coefficient (α) of GaAs material reported in literature[158] as shown in inset of Fig. 2.11. A suppression of the sub-bandgap SPV in presence of apparent pump laser is possible due to the following mechanisms. First, the laser populates/ depopulates the deep defect states via resonant excitation due to which the probe beam is not absorbed by the defect states. Second, it creates a background carrier density in conduction band. When the background carrier density is comparable to the probe beam induced carrier density, the component of SPV signal which is generated due to the diffusion of charge carriers is suppressed. Third, surface recombination is also suppressed due to the population/depletion of surface states by the pump laser. Note that a recombination of photo-excited carrier is considered to be a loss in SPV signal. This effect not only suppresses the surface state related SPV but also enhances the SPV related to band-to-band transition as obvious from Fig. 2.11. In presence of appropriate CW sub-bandgap laser excitation, all the sub-bandgap states assisted mechanisms are therefore minimized. Therefore, a strong enhancement of above bandgap SPV with a sharp edge related to bandgap of GaAs is observed in case of pump-probe SPS spectra.

While the pump-probe SPS measurements with 1064 nm laser are seen to provide an accurate value of the band edge of semiconductor epitaxial layers such as GaAs and InP, few obstacles are still observed in case of nitride epitaxial layers. To check the applicability of pump-probe SPS technique, conventional SPS measurements are performed on heavily Mg doped p-GaN epitaxial layer. The layer structure is consisted of 1000 nm Mg-GaN, 200 nm UID GaN, 70 nm AlN layer grown on sapphire substrate. The hole density was found to be 2.5x $10^{16}/cm^3$ whereas Mg concentration was $1x10^{20}/cm^3$.[159] SPS magnitude and phase spectra of p-GaN epitaxial layer which are recorded at 166 Hz modulation frequency are shown in Fig. 2.12 (a) and (b) respectively.

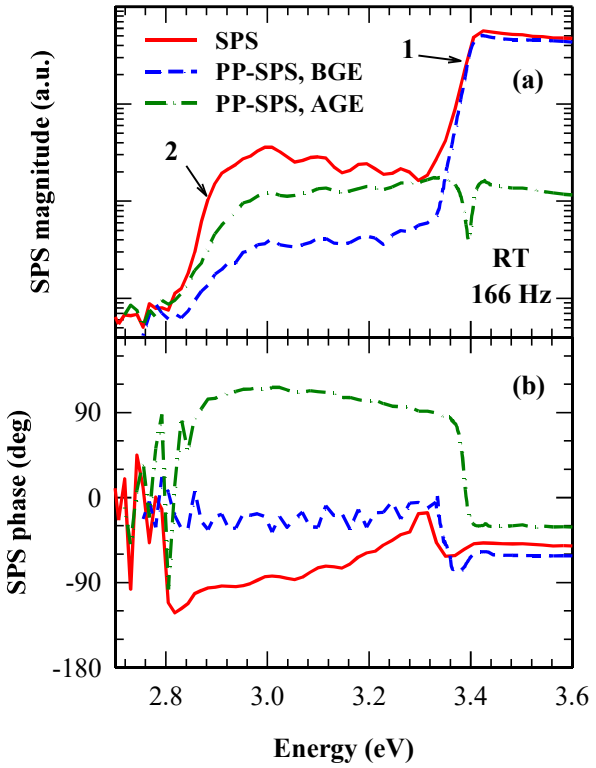

Figure 2.12 Room temperature SPS and pump-probe SPS (a) amplitude and (b) phase spectra of p-GaN sample recorded at 166 Hz modulation frequency. BGE and AGE corresponds to below bandgap pump excitation at 3.02 eV from lamp-monochromator assembly and above bandgap pump excitation at 3.81 eV from CW 325 nm laser respectively.

Band edge feature (feature-1) of GaN is obtained at 3.4 eV while an extra feature (feature-2) is also observed at 2.88 eV with an onset at 2.8 eV. Several fine oscillations are also observed between 2.8 and 3.4 eV in SPS spectra which are found to be related to interference oscillations by performing angle dependent SPS measurements. Though the contribution of feature-2 is small, its presence might affect the determination of bandgap by SPS technique as discussed earlier. To measure the bandgap of GaN, pump-probe SPS measurements with 1064 nm laser are performed. However, no measurable change in the SPS spectrum is seen in presence of apparent pump laser. This indicates that the pump beam is not absorbed at all by the sub-bandgap states. The observation

puts a limitation on pump-probe SPS measurements since one needs to choose a suitable laser which can make resonant excitation in defect states and can populate/ depopulate them considerably. Conventional SPS spectrum can help in choosing the appropriate laser as pump beam. Since the sub-bandgap SPS signal kicks at 2.8 eV, an optical excitation with energy higher than 2.8 eV can effectively suppress the contribution from those states. Due to the unavailability of a suitable sub-bandgap pump laser, we opted for a lamp based apparent pump beam which is obtained from a Xenon-arc lamp and monochromator assembly. The lamp based excitation is tuned to 410 nm (3.02 eV) which is well below the bandgap of GaN. A wide band pass (10 nm) of monochromator is chosen to maintain a reasonable value of photon flux of around 100-150 μW. Pump-probe SPS spectrum with lamp based sub-bandgap pump excitation is shown in Fig. 2.12 (curve BGE). It is observed that the contribution of Mg related sub-bandgap features is significantly suppressed even with such a low intensity of pump beam. It enables an unambiguous determination of the bandgap of p-GaN material even in presence of a large contribution of localized states and therefore demonstrates the suitability of pump-probe SPS technique for an accurate determination of the bandgap of epilayers under the strong influence of localized sub-bandgap states.

There is another advantage of pump-probe SPS which lies in pinpointing the spatial location of sub-bandgap SPS features as a function of depth. The schematic band diagram of p-GaN sample is shown in Fig. 2.13 which is obtained using BandEng software.[160] Above bandgap optical excitation is mostly absorbed with in few hundreds of nanometer from the sample surface. Thus, SPV signal corresponding to feature-1 is generated from the surface depletion region as marked by process-1 in Fig. 2.13. Excitation via process-1 reduces the surface potential giving rise to SPV signal. In

subsequent discussion, phase (-45°) of process-1 is taken as the reference. If phase of a SPS feature is same (opposite) to the reference phase, then the corresponding transition is reducing (increasing) the surface potential provided it is originated from the surface

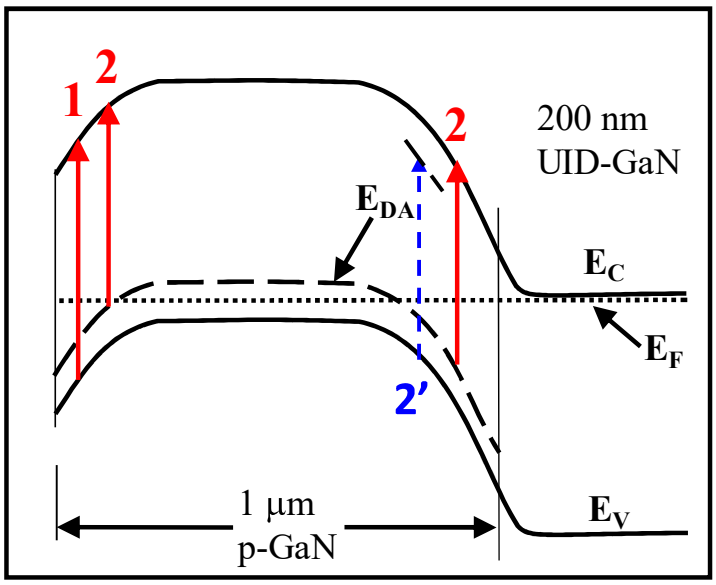

Figure 2.13 Schematic band diagram of p-GaN sample. Symbols E_C, E_V, E_F and E_{DA} correspond to conduction band, valence band, Fermi level and deep acceptor state respectively.

depletion region. Feature-2 is found to be in phase with feature-1 as shown in Fig. 2.12 (b) and therefore leads to suppression of surface potential if its origin lies in the surface depletion region. Feature-2 therefore can be correlated with deep acceptor to conduction band transition in the surface depletion region as described earlier in Fig. 2.7.[129] However, the sample is transparent to the optical excitation corresponding to feature-2. SPV corresponding to feature-2 therefore can originate from surface and/or interface depletion region. Further, the direction of surface electric field at the two depletion region is opposite as shown in Fig. 2.13 which will lead to SPV of opposite polarity for feature-2 in the two field driven region. If feature-2 is originated from the interface depletion

region, then the same phase corresponds to valence band (E_V) to deep donor state (E_{DD}) transition (process-2') for feature-2. Thus, from conventional SPS measurements, it is difficult to comment on the nature of the SPS transition when its spatial location within the sample is not appropriately pinpointed. In this context, pump-probe SPS with above bandgap pump laser can resolve this problem. To check the effectiveness, we have performed pump-probe SPS measurements on p-GaN sample with CW 325 nm laser (curve AGE). Strong absorption of 325 nm laser flattens the band bending and therefore leads to suppression of SPV that are generated in the surface depletion region. However, since the laser is unable to reach the interface depletion region, SPS generated from interface region will remain unaffected. A suppression of above bandgap SPV is observed as shown in Fig. 2.12 (a) which confirms its origin at the surface depletion region. However, feature-2 is found to have a strong contribution in opposite phase with respect to conventional SPS. This clearly indicates that the feature-2, where conventional SPS spectra is dominated by the component originating in surface depletion region, is dominated by the SPS component originating from the interface depletion region in case of pump probe SPS spectra. Once the spatial location of feature-2 is pinpointed in the surface depletion region in case of conventional SPS measurements, its origin can be firmly correlated with deep acceptor to conduction band transition which provide free electrons in conduction band. More details about the origin of feature-2 will be discussed in **chapter 3**. The technique is found to be very useful for characterization of defect states in AlGaN/GaN heterostructures which is presented in the next chapter.

2.7 Conclusion

Basic working principle of various experimental techniques that are extensively used to characterize AlGaN/GaN heterostructures is briefly discussed in this chapter. The spectroscopic techniques are found to be useful for studying the electronic band structure, dominant defects of epitaxial layers and heterostructures. Capabilities and limitations of conventional spectroscopic techniques are also briefly discussed. In particular, an accurate estimation of the bandgap of semiconductor epitaxial layer is found to be limited by a strong contribution from defects in case of conventional SPS measurements. An accurate determination of the bandgap of epitaxial layers, even under the strong influence of the localized states, is demonstrated by performing SPS measurements under pump-probe configuration. By choosing an appropriate energy and intensity of the apparent pump beam, the contribution of sub-bandgap states can be effectively suppressed which otherwise swamp the bandgap related information. Furthermore, an above bandgap pump beam can be used to obtain the complementary information related to the energy of sub-bandgap states and its spatial location along the depth of the material.

Chapter 3

Optical Characterization of Defects in GaN and AlGaN/AlN/GaN Heterostructures

3.1 Introduction

Efficiency of semiconductor devices based on heterostructures is primarily governed by the crystalline quality of associated epitaxial layers. In case of nitride epitaxial layers, the lack of native GaN substrate becomes the main obstacle in fabricating reliable and high efficiency devices. A large lattice and thermal mismatches introduces a large density of defects/dislocations of the order of ~ 10^8 cm^{-2} to 10^{10} cm^{-2} in GaN epitaxial layer when grown on foreign substrates such as Si or Sapphire. These defects are responsible for a variety of shortcomings in nitride based optoelectronic devices. In case of power devices, presence of defects/ dislocations leads to low gain, large noise, parallel conduction and current collapse.[22, 24, 51, 161] In case of light emitting devices, formation of non-radiative/radiative recombination centers reduces the device efficiency and its operational life.[162] Several reports are available in literature which deal with the identification and characterization of defects by applying different techniques such as photoluminescence (PL),[63] surface photovoltage spectroscopy (SPS),[64] photoionization,[163] photo-capacitance,[161] and deep level transient spectroscopy[73, 164]. Density functional theory based calculations on the probable defects states are developed

in parallel to correlate the experimentally observed defect signatures to specific defects.[92, 165, 166] A remarkable progress has been made by optimizing the growth process, superior buffer design and by minimizing the defect density. In spite of considerable progress, identification of point defects remain surprisingly puzzling where a large number of controversial observations are reported by numerous researchers. Two such controversial issues are related to the origin of blue luminescence (BL) and yellow luminescence (YL) in luminescence spectra of GaN. Despite of several counterbalancing reports, it is still not clear which defects contribute to the two emission bands. Further, the type of transition and its spatial location within the sample has also been the subject of discussion during the last two decades. Since the quality of buffer layer is of paramount importance for the optimization of device characteristics, this chapter is dedicated to the characterization of defects in GaN epitaxial layers. Optical spectroscopy methods like SPS and newly developed pump-probe SPS techniques are used to investigate the dominating defects in GaN epitaxial layers and AlGaN/GaN heterostructures. These results are then correlated with the commonly observed BL and YL bands by performing Photoluminescence spectroscopy (PL), and photoluminescence excitation (PLE) experiments.

3.2 Sample Details

A heavily Mg doped GaN epitaxial layer (p-GaN), a n-type GaN epitaxial layer (n-GaN) and an AlGaN/AlN/GaN HEMT structure (Sample-A) which are grown on c-plane (0001) of α-Al_2O_3 (sapphire) substrate are used in this study. Specifications of p-GaN sample are described in **Chapter 2.** The n-GaN sample is obtained from commercial

vendors which is grown by metal organic chemical vapour epitaxy technique. The n-GaN epilayer is ~5 um thick with a doping concentration of $2x10^{18}$ cm^{-3}. Sample-A is grown by Ammonia molecular beam epitaxy (MBE) system on c-plane Fe-GaN semi-insulating templates. The layer structure is consisted of 25 nm $Al_{0.33}Ga_{0.67}N$ barrier layer, 1 nm AlN interlayer, 1 µm undoped GaN channel layer, 200 nm lightly Mg-doped GaN buffer interlayer grown on 3.5 µm Fe-doped GaN template. Typical values of sheet carrier concentration and mobility are measured to be $2.4x10^{13}$ cm^{-2} and 1400 cm^2/V-sec at room temperature respectively from Hall experiments.

3.3 Characterization of Blue Luminescence Band in Heavily Mg Doped GaN

3.3.1 PL Characterization

Room temperature (RT) PL spectra of p-GaN and n-GaN samples are shown in Fig. 3.1. Three distinct features related to free exciton-A (FX_A), blue luminescence (BL) and yellow luminescence (YL) are observed at 3.4 eV, 2.8 eV and 2.2 eV respectively for p-GaN sample. For n-GaN sample, only FX_A and YL features are observed. In both the samples, PL features are superimposed with interference oscillations.[167] YL feature in GaN is related to the conduction band/shallow donor level to a deep defect transition at ~ 1 eV above the valence band maxima.[78, 81, 168] In literature, BL band is reported to appear only in case of heavily Mg doped GaN epitaxial layers and is considered to be associated with Mg related deep states. However, the origin of BL band is reported to be

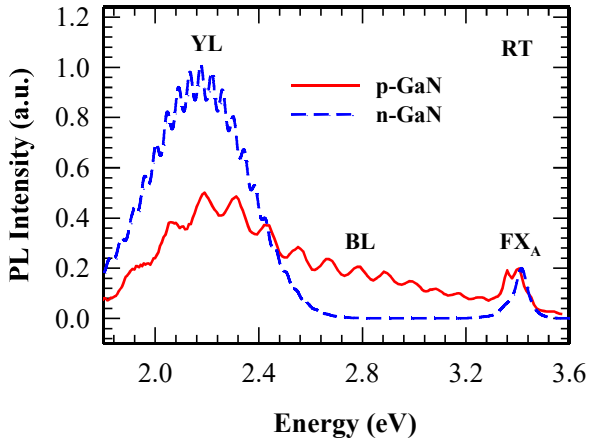

Figure 3.1 Room temperature PL spectra of p-GaN and n-GaN epitaxial layers where labels FX_A, BL and YL corresponds to Free exciton-A, blue luminescence and yellow luminescence respectively.

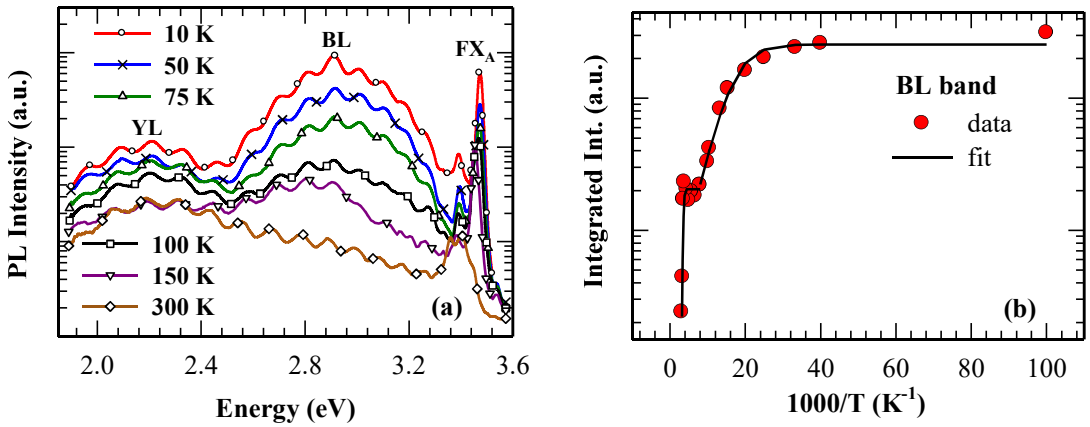

Figure 3.2 (a) Temperature dependent PL spectra of p-GaN sample recorded at 0.8 W/cm^2 excitation intensity. (b) Temperature dependence of the integrated BL intensity of p-GaN sample. YL, BL and FX_A corresponds to yellow luminescence band, blue luminescence band and free exciton-A respectively.

contradictory. Two recombination models are proposed to explain the origin of BL band: 1) excitation from deep donor at E_C-0.35 eV to shallow acceptor at E_V+0.2 eV, and 2) excitation from the conduction band to deep trap state at E_V+0.55 eV. Surprisingly,

experimental evidences in support/against both the models are available in literature.[70, 76, 106, 108, 110, 111] In order to find the true recombination model for BL band, temperature dependent PL measurements are performed on p-GaN sample. Figure 3.2 (a) shows the temperature dependent PL spectra of p-GaN at few representative temperatures recorded at an excitation intensity of 0.8 W/cm^2. A sharp FX_A peak is observed at 3.475 eV. Broad YL and BL bands are also observed at 2.2 and 2.93 eV respectively. It is found that the intensity of BL band decreases with sample heating. Line shape analysis of PL spectra is carried out where BL band is fitted by a Gaussian function. An Arrhenius plot for the BL band is shown in Fig. 3.2 (b). It is noticed that the integrated intensity of BL band first gradually falls with rise in temperature up to 150 K. No appreciable change in the integrated intensity is then seen up to 250 K above which a sudden fall is observed. Such a kind of temperature dependence of PL peak energy is a bit uncommon and cannot be fitted with Arrhenius formula[169, 170] as given below,

$$I(T) = \frac{I(0)}{1 + \sum_i C_i \exp\left(\frac{-E_{Ai}}{kT}\right)} \tag{3.1}$$

where $I(T)$ represents temperature dependent integrated PL intensity, C_i is fitting constant and E_{Ai} is the activation energy of i^{th} energy component contributing to the PL peak. A similar anomaly was observed by Lu *et al.*[170] in case of non-resonant excitation in InGaN/GaN based LEDs. It was explained by considering the temperature dependent carrier transport from GaN barrier to InGaN quantum well. In case of p-GaN epitaxial layer, hole mobility increases with rise in temperature up to ~200 K.[118] The enhanced drift/diffusion increases the capture of photo-generated holes by the deep trap states leading to an increase in intensity of BL band. The net effect of enhanced drift/ diffusion

and temperature dependent activation lead to anomalous temperature behavior of BL band as shown in Fig. 3.2 (b). Since the Arrhenius plot can't be fitted with single function for entire temperature range, activation energy is approximated by fitting two Arrhenius function in the two temperature ranges with i=1. An activation energy of 24±2 meV is estimated from 10 -150 K temperature range while activation energy of 396±132 meV is estimated in the high temperature region. Activation energy estimated in the high temperature range contains relatively large error due to less number of data points. Nevertheless, a large value of activation energy in the high temperature range is expected due to the sudden fall of PL intensity. A low activation energy of 24±2 meV corresponds to the activation of shallow donors in p-GaN. A similar value is estimated at very low optical excitation intensity which excludes the possibility of potential fluctuation as a possible cause of PL decay in low temperature range. Note that the PL intensity shows a gradual fall up to 150 K whereas the spectral shape of BL band remains almost the same. This indicates that the recombination from shallow donor level dominates the BL band below 150 K. However, recombination from the conduction band dominates the BL band in the high temperature range. Since, the initial state in PL recombination is associated with conduction band and/or shallow donor states, the final state has to be a deep state near the valence band. A large value of the activation energy (~396 meV) therefore corresponds to the thermal activation of holes from a deep state to valence band. It therefore indicates that the BL band in heavily doped p-GaN sample is governed by the downward transition following model-2. Temperature dependence of BL band is discussed by several researchers where temperature invariance of integrated intensity is reported below 200 K.[124, 159] Only a few reports are available where intensity of BL band is seen to vary with temperature below 200K.[107, 108, 110] In particular, Sheu *et al.*[108]

presented the temperature dependence of BL band up to room temperature where they speculated that the BL band originates due to the downward transition from a shallow donor level lying 30 meV below E_C to Mg-related deep level lying 510 meV above E_V. However, no efforts were made by them to estimate the activation energy corresponding to the respective energy levels. The measurements shown in Fig. 3.2 (b) clearly support this hypothesis where the values of activation energy are also found to be in reasonable agreement. However, a low activation energy is estimated by us for the deep acceptor states. Note that the activation energy of deep levels estimated by most of the researches vary from 0.2 to 0.35 eV.[63] In case of model-2, an underestimation of activation energy can be explained by considering a wide distribution of the density of states of deep acceptors towards the valence band edge in p-GaN.[106] Holes might be thermally excited to E_V at high temperature from the low energy deep acceptor states which can result in an underestimation of the activation energy.

Note that, an activation energy of ~340 meV was estimated by Reshchikov *et al.*[124] by studying the quenching of BL band. It was correlated with the thermal activation of electrons from deep donor state at E_C-0.35 eV to E_C in line with model-1 where deep donor to shallow acceptor transition is considered as the origin of BL band. This raises a doubt about the assignment of deep donors since shallow acceptors have a much lower activation energy (~0.2 eV) than deep donors. However, no information about the activation energy of shallow acceptors was given by them from Arrhenius plot of BL band. In this context, the experimental results fits better with model-2.

3.3.2 SPS Characterization

In order to understand the fundamental mechanism of sub-bandgap spectroscopic features including the BL band, systematic SPS measurements are performed on both the samples. Figure 3.3 (a) and (b) show the room temperature SPS magnitude and phase spectra of the two samples recorded at 28 Hz respectively. SPS spectra of p-GaN sample is already presented in **chapter 2** (Fig. 2.12) where feature-1 and feature-2 are correlated to band edge and deep acceptor-to-conduction band transition. The features are found to be dominated from surface depletion region in conventional SPS measurements, however, transition detail of feature-2 is not discussed in detail. A low energy feature is also observed in Fig. 3.3 (a) (feature-3) which is clearly distinguishable from the noise level above 2.3 eV. In case of n-GaN sample, feature-3 is extended up to GaN band edge where its magnitude increases exponentially with energy. Spectral location of feature-2 (feature-3) is found to be in good corroboration with BL (YL) band observed in the PL spectra shown in Fig. 3.1 respectively. Thus feature-3 is considered as upward transition from YL related deep trap state to conduction band.[94] This process will enhance (reduce) the surface barrier height in case of n-GaN (p-GaN) epitaxial layers respectively.[129] Thus the SPS signal corresponding to feature-3 should be in opposite (same) phase with respect to feature-1 for n-GaN (p-GaN) epitaxial layers respectively. A 180^{o} phase difference observed between feature-1 and feature-3 in case of n-GaN epitaxial layer as shown sample, an intermediate phase difference of ~90^{o} is observed. An intermediate phase corresponds to the lag of feature-3 SPV signal with respect to optical excitation.[171] Absence of feature-3 in Fig. 2.12, which is measured at 168 Hz, is a direct evidence for the large lag of feature-3 with respect to optical excitation. Now, we need to see if the aforementioned model can explain the fundamental origin of feature-2. Figure 3.3 (c)

and (d) shows the schematic band diagram of p-GaN sample along with optical transitions according to model-1 and model-2 respectively. According to model-1, the excitation process must inject electrons in deep donor level (E_{DD}) and holes in shallow acceptor level (E_{SA}) simultaneously. Activation energy of shallow acceptors (200 meV) and deep donor (350 meV) is substantially larger than thermal energy at room temperature. Since, both the carriers are trapped by the deep donor/shallow acceptor at the same location in sample, no SPS signal will be generated. However, a weak signal

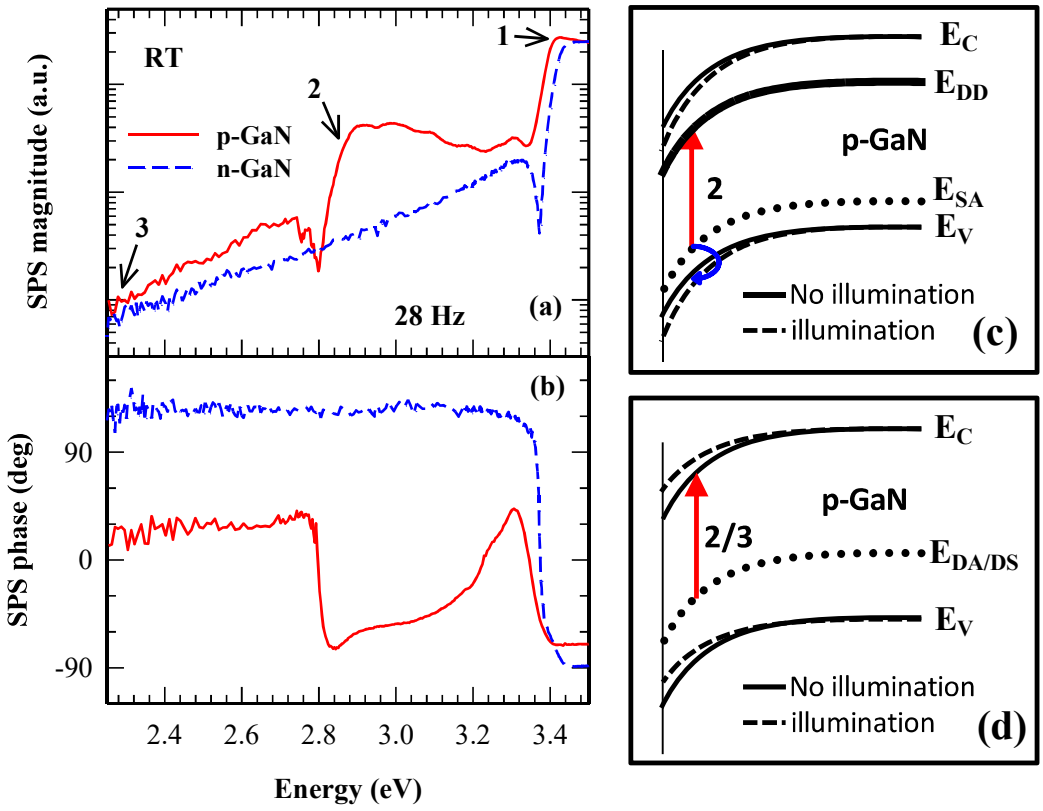

Figure 3.3 Room temperature SPS (a) magnitude and (b) phase spectra of p-GaN and n-GaN samples recorded at 28 Hz modulation frequency. Schematic band diagram of p-GaN sample showing upward transitions according to (c) model-1 and (d) model-2. E_C, E_V, E_{DD}, E_{SA}, E_{DA}, E_{DS} corresponds to conduction band, valence band, deep donor, shallow acceptor, deep acceptor and deep state respectively.

might appear only if at least one of the two photo-excited carriers is thermally excited to the respective band. Since the shallow acceptors in p-GaN possess low activation energy compared to deep donors, thermal excitation of holes from E_{DA} to E_V is favored. Hence, following the excitation process in p-GaN, holes are thermally excited to E_V which drift away from the surface depletion region. However, electrons are still trapped by the deep donors. This process increases the surface potential and therefore produces SPV in opposite phase with respect to feature-1. However, a contradictory observation is made in Fig. 3.3 (b) where phase the two features is found to be almost the same. A large variation of SPS phase near the band edge of GaN is observed because of the dominance of feature-3 over feature-2 in the particular energy range. The same can be appreciated by examining the shape of SPS spectra of two samples shown in Fig. 3.3 (a). It is therefore clear that the model-1 cannot explain the observations made here. To exclude model-1 further, temperature dependent SPS measurements are performed and a few representative spectra are shown in Fig. 3.4. These SPS measurements are performed at 1 KHz modulation frequency where the contribution of feature-3 is largely suppressed. A blueshift of feature-1 is seen due to the increase bandgap of GaN layer at low temperature. It is also seen that the intensity of feature-2 decreases with sample cooling whereas its energy onset remains almost the same over the entire temperature range. At low temperature, both the shallow acceptor as well as deep donor states are expected to be filled. Ideally, no excitation from shallow acceptor to deep donor is possible at 10 K. Further, thermal activation of holes from E_{DA} to E_V is also not favored at 10 K. Therefore, if feature-2 is governed by the excitation of electrons from shallow acceptor level to deep donor states then such a feature shouldn't appear at 10 K. However, a small contribution of feature-2 is present even at 10 K. Moreover, a blueshift of feature-2 with cooling is

also expected due to the filling of low lying donor/acceptor states. However, no major change in the energy onset of feature-2 is seen in Fig. 3.4. It therefore excludes the correlation of feature-2 with shallow acceptor to deep donor transition (model-1). However, if model-2 is considered, then the process excites electrons from deep acceptor state (E_{DS}) lying at E_V+0.55 eV to the conduction band minima. Due to downward band bending at the surface and at p-GaN/undoped GaN interface, acceptor states are expected to be filled in the depletion regions enabling optical excitation corresponding to feature-2. Since, the minority carrier (electron) is free in such a transition, SPS signal is expected

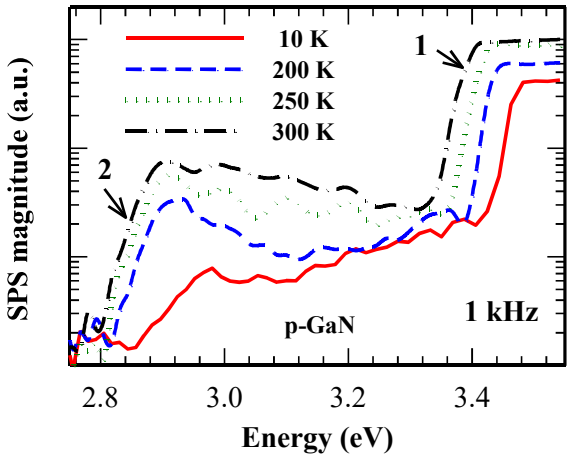

Figure 3.4 Temperature dependent SPS magnitude spectra of p-GaN sample recorded at 1 kHz modulation frequency.

to be in phase with the above bandgap SPV component.[129] The same is confirmed by the variation of phase shown in Fig. 3.3 (b). Note that the intensity of such a transition is expected to be high at low temperature due to the filling of shallow acceptor states. On the contrary, a systematic fall in the strength of feature-2 with cooling is seen in Fig. 3.4. One possible explanation for the low SPS signal at low temperature can be given by the recombination of photo-excited carriers. A firm confirmation of enhance recombination is already shown in Fig. 3.2 (a) where BL intensity increases with decreasing

temperature. At elevated temperature, shallow donor states are expected to be in thermal equilibrium with the conduction band which accelerates spatial separation of photo-excited electrons from the holes captured by the deep acceptors. With decreasing temperature, the photo-excited electrons get localized by shallow donors. The localized carriers recombine efficiently leading to a stronger BL band whereas a poor spatial separation of carriers lead to a weak SPV signal. Note that the recombination of excess carriers is considered to be a loss in SPS signal. Thus, the strength of SPV related to fearure-3 decreases with decreasing temperature as shown in Fig. 3.4.

Temperature dependent PL studies therefore confirms that the presence of a deep acceptor state is responsible for the generation of BL band in p-GaN. SPS measurements provide unambiguous signature of a deep acceptor level lying at E_V+0.55 eV only in p-GaN sample. The acceptor levels provided by the two complementary methods will indeed be the same provided the Franck-Condon shift (d_{FC}) is negligibly small. In fact, a feature at E_C-2.97 eV with d_{FC}=0.02 eV is already reported in steady state photo-capacitance and deep level optical spectroscopy measurements on p-type GaN by Armstrong *et al*.[172] Further, following a low value of d_{FC}, the recombination lifetime of BL band is expected to rather very short as reported by several researchers.[76, 122] Thus, the optical transition between shallow donor/ conduction band and deep acceptor at E_V+0.55 eV is responsible for feature-2 in SPS spectra and the BL band in p-GaN sample.

3.4 Characterization of Yellow Luminescence Related Defect States in AlGaN/AlN/GaN Heterostructure

One of the most notorious defect in GaN is related to the observation of yellow luminescence (YL) band whose spatial location within the sample and exact attribution to specific defects in GaN is still a matter of intense debate.[38, 75, 77-84] Very recently, interesting theoretical predictions and experimental observations have been made by a few research groups where either isolated C_N defects [75, 79, 83] or a shallow donor (SD)-deep donor (DD) C_N-O_N defect complexes[78] are proposed as the main source for the generation of YL band in GaN. In fact, Reshchikov *et al*. have shown that the purity of GaN layer decides whether the mechanisms of YL band is governed by either isolated C_N defects or C_N-O_N defect complexes.[77, 80] It is also observed that the spatial location of YL band is equally controversial. Long ago, Shalish *et al*. have shown that the YL related defect states exist on the surface of GaN film.[94] Later, a few other researchers also reported the presence of defect states which lie on the surface of nitride semiconductors.[95-99] On the other hand, defect states associated with YL band are reported to be distributed over the bulk material by other groups.[38, 83, 173] Bulk nature of defect states is also confirmed by some researchers by employing characterization techniques other than the PL spectroscopy.[82, 101, 174] Very recently, Matys *et al*.[84] reported that the YL band arises from donor-acceptor pair (DAP) recombination in very limited regions of nanometre scale lying in the depletion region in the proximity of semiconductor surface. Note that, the intensity ratio corresponding to the band edge and yellow luminescence signals in GaN is often used to define the purity of epilayers.[84, 93] It will therefore lead to the conclusion that the purity of epilayer is a function of sample depth which might not be true. In this chapter, SPS and pump-probe SPS measurements

are performed with an overall aim to identify the defect states along with their spatial location in AlGaN/AlN/GaN heterostructures. Conventional and pump-probe Photoluminescence excitation (PLE) measurements at YL band are also performed which nicely complement the observations made through SPS measurements. In particular, YL band is studied in depth where a phenomenological model based on the optical transitions involving a three-level system is proposed to explain the spectroscopic results.

3.4.1 SPS Characterization

Figure 3.5 (a) shows the room temperature SPS magnitude spectra of AlGaN/GaN heterostructure (Sample-A) recorded at 28 Hz chopping frequency whereas the corresponding phase variation is shown in Fig. 3.5 (b). Several sharp features are observed in SPS spectra which are labelled as feature-1, is related to the band edge of top AlGaN barrier layer. Various upward transitions associated with the generation of SPS signal corresponding to the features seen in Fig. 3.5 are schematically shown in Fig. 3.6. The band diagram shown in Fig. 3.6 is based on a self-consistent solution of Schrödinger and Poisson equations.[160] When the energy of excitation beam is larger than the bandgap of AlGaN barrier layer, electron-hole pairs are mainly generated in the top AlGaN barrier layer while only a small fraction is generated in GaN channel layer. Photo-induced electrons in the AlGaN layer drift towards the AlGaN/GaN interface whereas holes drift towards the air/AlGaN surface under the influence of polarization induced electric field. The charge separation screens the electric field which leads to the generation of SPS signal as schematically shown by process-1 in Fig. 3.6. The electron-hole pairs injected in the triangular potential well in GaN layer move in an opposite direction compared to

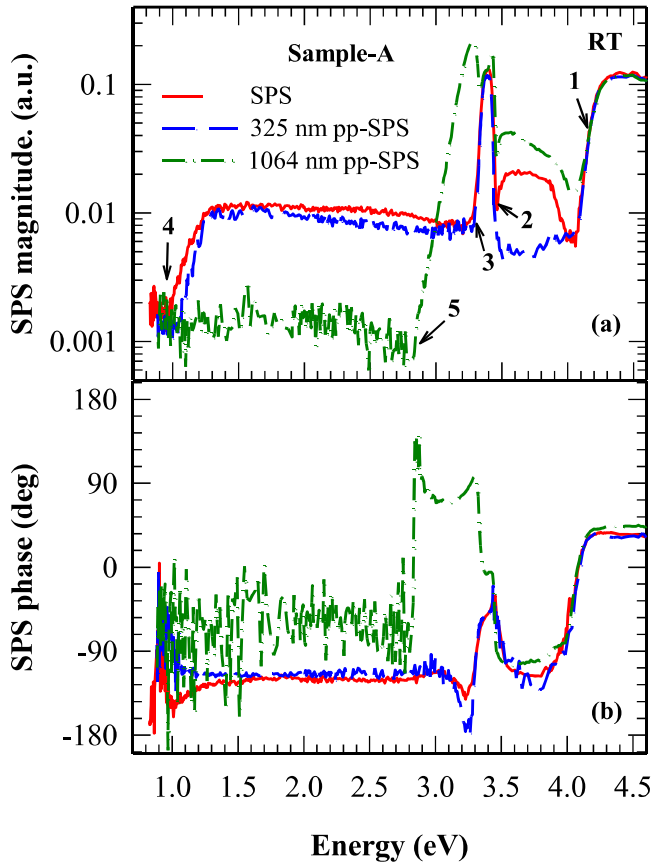

Figure 3.5 Room temperature SPS and Pump-Probe SPS (a) magnitude, and (b) phase spectra of AlGaN/GaN heterostructures recorded at 28 Hz chopping frequency.

those created in AlGaN layer due to the opposite built-in electric field. Therefore, the generation of electron-hole pairs in this region will provide a SPS signal, marked as process-2 in Fig. 3.6, which has a phase value exactly opposite to that of the process-1. Note that the resultant SPS signal is given by the vector sum of individual SPS components generated via different processes occurring in respective regions of AlGaN/AlN/GaN heterostructure. The observation of AlGaN related SPS feature in the energy range above 4 eV confirms that the SPS signal generated in AlGaN layer via process-1 dominates over process-2 in GaN channel layer. When the energy of excitation beam falls below the bandgap of AlGaN barrier layer, the SPS signal generated via process-2 in GaN channel layer dominates. An opposite phase of feature-2 compared to

feature-1, as shown in Fig. 3.5 (b), is in line with the abovementioned discussion. A relatively low magnitude of SPS signal corresponding to process-2 is expected due to the presence of

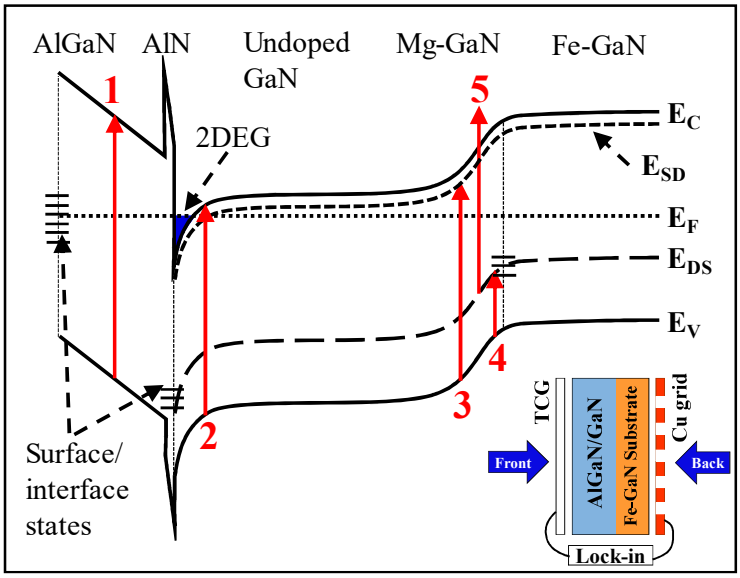

Figure 3.6 Schematic band diagram of the AlGaN/GaN heterostructure (sample-A) where symbols 2DEG, E_C, E_V, E_F, E_{SD}, and E_{DS} stand for 2-dimensional electron gas, conduction band, valence band, Fermi level, shallow donor and deep trap states respectively. Note that the band profile is drawn not to scale and is enlarged in certain locations to illustrate the field driven regions for the purpose of clarity. Inset shows the geometry of SPS measurements performed under front and back illumination schemes.

high background electron concentration in the bulk GaN and also the 2DEG at AlN/GaN heterointerface.[175, 176] Note that the presence of 2DEG in the triangular potential well is equivalent to an accumulation region in n-type GaN. In this case, majority carriers (electrons) moves towards the triangular potential well while the minority carriers (holes) are either captured by the deep traps located near the triangular potential well or they move deep inside the GaN layer where they recombine with free electrons present in the flat band region of n-GaN.[64] In either case, the magnitude of SPS signal is expected to

be rather small. Recombination of excess carriers is considered as a loss in SPS measurements since only those photo-generated carriers which can be separated out by some physical mechanism are able to contribute towards the measured SPS signal. Present hypothesis is also supported by SPS measurements performed on HEMT samples with high concentration of Mg in Mg-doped interlayer. In those samples, a strong SPS signal corresponding to process-2 is observed over the same energy range which is shown later in **chapter 5**. Mg-doping of a part of GaN channel layer in AlGaN/GaN HMET structures is needed to reduce the background electron concentration and also compensate the deep trap states.[35, 36] The low background electron concentration reduces the recombination probability whereas a low deep trap density reduces carrier trapping. Both these effects lead to an enhancement in the magnitude of SPS signal.

3.4.1.1 Identification of Spatial Location of Defects

Once the energy of excitation beam falls below the bandgap of GaN channel layer, light is absorbed throughout the GaN channel layer via the involvement of sub-bandgap states. Several mechanisms can be attached with the absorption of sub-bandgap excitation beam in different parts of GaN channel layer i.e. accumulation region near AlGaN/GaN interface, flat band region, depletion region near GaN/Fe-GaN interface and Fe-GaN region. In order to pinpoint the location of sub-bandgap SPS features, SPS measurements are performed under back illumination geometry. In case of back illumination geometry, back side of the sample is polished mechanically and the sample is mounted between TCG and Cu-grid electrode. SPS measurements are thereafter performed with light illumination from either side of the sample keeping all other

conditions nearly the same as shown in the inset of Fig. 3.6. However, the SPS magnitude is low in this configuration. Hence, we opted for laser of different wavelengths or Xe lamp/monochromator assembly with relatively large bandpass to get adequate SPV signal in the sub-bandgap region of GaN. It is found that the phase of sub-bandgap SPS features remain more or less the same when either the front or back illumination geometry is used (not shown here). Such an observation is critically important in order to rule out the possibility of SPS mechanism based on Dember process. Note that the phase of SPS signal should switch by 180^{o} when going from the front to back illumination geometry, if the origin of SPS signal was governed by the Dember process. In view of this, the possibility of generation of sub-bandgap SPS features in the flat band region of undoped GaN and Fe-GaN via Dember process is ruled out. It indicates that the sub-bandgap SPS signal is generated either in the accumulation region near AlGaN/GaN heterointerface or in the depletion region lying at GaN/Fe-GaN interface. In order to obtain further clarity about the spatial location of SPS features, pump-probe SPS measurements[177] are performed with a He-Cd laser operating at 325 nm and the results are shown in Fig. 3.5. Note that the He-Cd laser beam is going to be absorbed strongly in the accumulation region which will suppress the associated SPS signal. A substantial decrease in the magnitude of feature-2 is observed. On the other hand, no significant change is observed in the SPS spectra associated with sub-bandgap features. It confirms that the feature-2 is originating from accumulation region while all the sub-bandgap SPS features are generated mainly at the depletion region lying near GaN/Fe-GaN interface.

3.4.1.2 Identification of Spectral Origin of Defects

In light of this information, the spectral origin of sub-bandgap SPS features seen in Fig. 3.5 can be understood with a reasonable clarity. A strong SPS peak with an onset at ~3.28 eV is observed at ~3.4 eV and is labelled as feature-3. Origin of this feature can be explained by considering an upward transition from the valence band (E_v) to shallow donor level (E_{SD}) in GaN as shown by process-3 in Fig. 3.5. The shallow donor states lie ~30 meV below the conduction band edge and are related to Si atoms present at GaN/Fe-GaN interface.[178] Incorporation of Si in GaN caused by the out-diffusion of Si from Fe-GaN template is a well-known problem which leads to parallel conduction in the devices based on AlGaN/GaN heterostructures grown on Fe-GaN templates.[36] In general, a significant fraction of Si donors is ionized at room temperature. Absorption of excitation beam resonant with Si donor levels creates free holes in the valence band. Electrons excited to Si donor levels are either trapped by the defects states or thermally excited to the conduction band. Both these effects reduce the interface potential barrier and provide an SPS signal which is in phase with respect to process-2. A very broad SPS feature is observed at ~1.3 eV with an onset at ~0.95 eV as shown in Fig. 3.5 (a) and is labelled as feature-4. Note that the broad SPS feature covers a large energy range even approaching the band edge of GaN which is also evident from a constant phase below 3 eV in Fig. 3.5 (b). Further, the SPS phase of feature-2 and feature-4 are nearly same which indicates that the feature-4 is also associated with the photo excitation of holes in the valence band. Here, photo-excited electrons are trapped by the deep trap states (E_{DS}) (process-4 in Fig. 3.6) whereas holes move towards GaN/Fe-GaN interface which generates an SPS signal in phase with feature-2. In order to investigate it further, pump-probe SPS measurements are performed with Nd-YAG laser operating at 1064 nm where the magnitude and phase

of SPS spectra are plotted in Fig. 3.5 (a) and (b) respectively. Since the deep level lies ~1 eV above the valence band, pump beam is able to excite electrons only to those states. It is interesting to see that the Feature-4 is completely suppressed by the pump beam due to the filling of deep trap states. In addition to this, the SPS signal associated with process-2 is significantly enhanced by the pump beam as obvious from Fig. 3.5 (a). The deep trap states near AlN/GaN heterointerface, which were able to trap the photo-generated holes in case of conventional SPS, are effectively saturated by the pump laser beam. It enhances the number of spatially separated photo-excited holes and therefore enhances the amplitude of feature-2. Nearly same phase of feature-2 for SPS and pump-probe SPS measurements indicate that the mechanisms of SPS generation is identical in both the cases. Further, a new SPS peak appears at ~3.28 eV with an onset at ~2.8 eV which is labelled as feature-5 in Fig. 3.5 (a). Intensity of feature-5 in SPS spectra sharply rises with the 1064 nm pump laser where that of the feature-4 falls as shown in Fig. 3.7 (a). Simultaneous appearance of feature-5 and disappearance of feature-4 in pump-probe SPS measurements with a sub-bandgap laser confirms that the two features are related to the same set of defect states lying in the vicinity of GaN/Fe-GaN interface. The pump laser intensity dependence of SPV can be understood in terms of the variation of occupation function (f_{DS}) of the deep state (E_{DS}) as shown schematically in Fig. 3.7 (b) and (c). Due to upward band bending, a fraction of deep trap states lying at GaN/Fe-GaN interface are empty even in absence of probe beam excitation. Feature-4 therefore arises due to E_V to unoccupied E_{DS} transition. Now, the value of f_{DS} rises with the intensity of sub-bandgap pump beam. This suppresses feature-4 transition probability which follows the variation of $(1-f_{DS})$. However, the rise of f_{DS} enhances resonant excitation of electrons from E_{DS} to conduction band (feature-5) which follows the variation of f_{DS}. Note that one

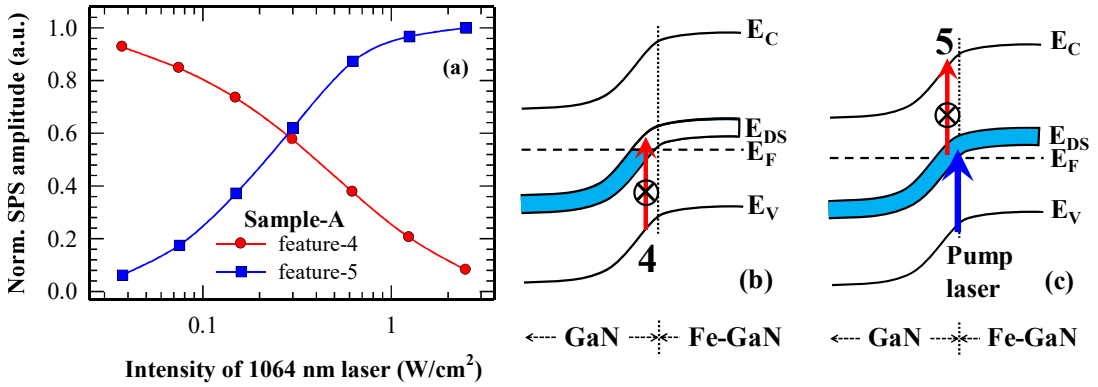

Figure 3.7 (a) Normalized pump-probe SPS magnitude corresponding to feature-4 and feature-5 are plotted as a function of pump beam intensity where solid lines are only a guide to eye. The schematic band diagram of AlGaN/AlN/GaN heterostructure near GaN/Fe-GaN interface in (b) absence and (c) presence of 1064 nm pump laser. The symbols E_C, E_V, E_F and E_{DS} corresponds to conduction band, valence band, Fermi level and deep state respectively. Probe beam is shown by red vertical arrow with chopper symbol while the pump beam is shown by blue vertical arrow.

expects injection of free holes in valence band via process-4 whereas process-5 provides free electrons in the conduction band. That's why the phase of SPS signals corresponding to the feature-4 and feature-5 are ~180° apart as shown in Fig. 3.5 (b). Further clarification about the occupation of the deep state will be discussed in the numerical model in the subsequent section. Now, an important question arises about the origin of feature-5 from the AlN/GaN accumulation region. Since the deep states are already filled in this region under equilibrium, feature-5 is expected to appear from accumulation region in conventional SPS spectra. However, no such features are observed in room temperature SPS spectra as shown in Fig. 3.5 (a). This indicates that either the deep states are absent in the accumulation region or some other fundamental mechanism prohibiting SPS generation corresponding to feature-5. To understand it further, temperature

dependent SPS measurements are performed on Sample-A, and are discussed in the subsequent section.

3.4.1.3 Temperature Dependence of Defect Related SPS Features

In order to identify the presence of deep trap states near AlN/GaN heterointerface, temperature dependent SPS measurements are performed down to 10 K. Figure-3.8 (a) and (b) show the temperature dependent SPS magnitude and phase spectra of AlGaN/AlN/GaN heterostructure recorded at 28 Hz modulation frequency respectively. GaN band edge related feature (feature-2) is not clear due to the dominance of feature-3 above 200 K and appearance of two new SPS features (feature-6 and 7) with onset at 2.85 eV and 3.15 eV respectively below 200 K. The dominance of new features masks feature-3 also due to which its temperature dependence is not clear. It is found that the feature-6 and 7 have a long characteristic time constant compared to feature-3 for which its intensity decreases rapidly with increasing modulation frequency as shown in Fig. 3.8 (c). In view of this, temperature dependent SPS measurements are performed at 3 kHz modulation frequency and the spectra are shown in inset of Fig. 3.8 (a). It is observed that the new SPS features are largely suppressed at high modulation frequency. Feature-3 is now clearly resolved and its temperature dependence can be discussed unambiguously. It is found that feature-3 blueshifts and its intensity decreases at low temperatures. The blueshift is caused by the enhancement of bandgap of GaN. Further, filling of shallow donor states at low temperatures reduce the probability of E_V to E_{SD} transition. It reduces the strength of feature-3 as obvious from the inset of Fig. 3.8 (a). Due to this, the feature-3 can't be distinguished below 150 K where it seems to merge

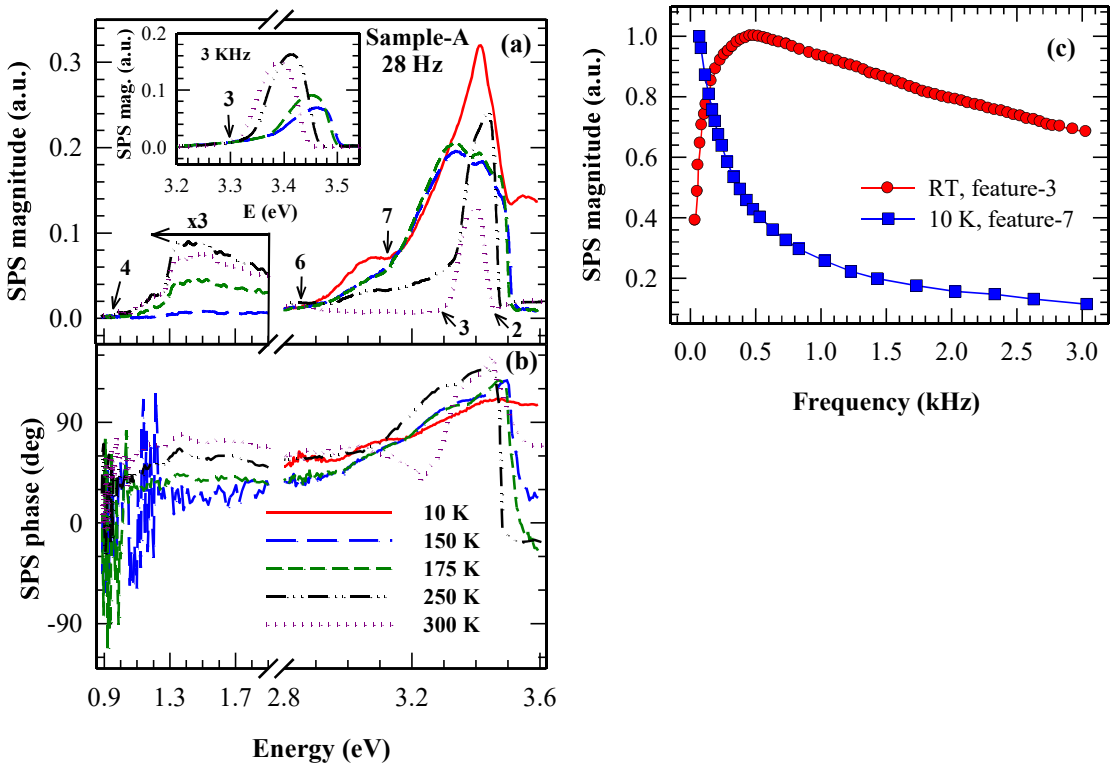

Figure 3.8 Temperature dependent SPS (a) magnitude and (b) phase spectra of Sample-A recorded at 28 Hz modulation frequency. Modulation frequency dependence of room temperature (c)SPS magnitude at 3.39 eV (feature-3) and 10 K SPS magnitude at 3.35 eV (feature-7).

with other sub-bandgap features that are already suppressed at 3 kHz. The strength of feature-4 is found to decrease significantly with cooling and disappear below 150 K as shown in Fig. 3.8 (a). Fall in the intensity of feature-4 with temperature can be explained by considering two possible effects; 1) deep trap states lying in the depletion region are being filled with falling temperature, and 2) mobility of hole reduces at low temperature[118]. A rise in the occupation probability of deep trap states reduces the probability of E_V to E_{DS} transition whereas a low hole mobility reduces the effective separation of charge carriers. Both the effects lead to the suppression of feature-4 similar to feature-3. A limited separation of charge carriers governed by the low mobility of

holes is found to be crucial for the appearance of 2DEG features in PL spectra of AlGaN/AlN/GaN heterostructures at low temperature as will be discussed in the next chapter[175]. It also indicates that at low temperatures the strength of SPV signal is primarily governed by the photo-generated electrons. The dominance of feature-6 and 7 at low temperature therefore indicates that these features lead to the injection of electrons in conduction band. A rise in the occupation of the deep state (E_{DS}) with decreasing temperature will enhance E_{DS} to conduction band (E_C) transition (process-5) similar to pump-probe SPS measurements with 1064 nm laser. In fact, feature-6 and 7 appears at low temperature whose intensity increases with decreasing temperature. Further, the onset of feature-5 in pump-probe SPS spectrum and feature-6 at low temperature SPS spectrum are very close. It indicates that feature-5 and feature-6/7 involves the same set of defect states.

It is worth to note that the phases of feature-4 and feature-6/7 are quite similar as shown in Fig. 3.8 (b). However, the phases of the two features are expected to be opposite if they are originating from same spatial location within the sample as explained before in pp-SPS with 1064 nm laser. Such a contradictory variation of phase can be explained by considering the dominance of feature-6 and 7 near accumulation region at low temperature. A clear indication of this assumption is already reflected in Fig. 3.8 (a) where a rise in SPS magnitude in the above bandgap of GaN is observed. This indicates that SPV from the accumulation region starts dominating at low temperature. In order to know the spatial location of feature-6 and feature-7, pump probe SPS measurements are performed at 10 K with 325 nm cw laser and the spectrum is shown in Fig. 3.9. For comparison, conventional 10 K SPS spectra is also plotted in the same graph. A new feature is observed with an onset at 2.2 eV (feature-8) which can be associated with the

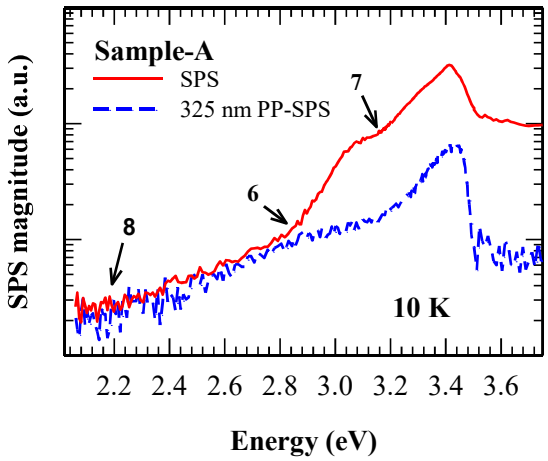

Figure 3.9 10 K SPS and pump-probe SPS spectra of AlGaN/GaN heterostructure recorded at 28 Hz chopping frequency.

deep trap states to conduction band transition[94, 161]. The pump beam is going to be strongly absorbed by GaN channel layer which will suppress all the SPV components originating within the penetration depth. The observations made in Fig. 3.9 strongly support this hypothesis where GaN band edge feature is found to be suppressed in case of pump-probe SPS measurements with 325 nm CW laser. Interestingly, feature-6 and 7 are also considerably suppressed by the pump beam. This is possible only if those features are originated near AlN/GaN interface. Due to the downward band bending in the accumulation region, electrons drifts towards the triangular potential well as shown in Fig. 3.6. It is going to screen the electric field in the accumulation region somewhat similar to the above bandgap excitation in GaN. It will therefore generate SPV in phase with the band edge feature of GaN which is in fact the case as shown by the phase spectra in Fig. 3.8 (b). Another possibility also exists where these features might originate from the deep trap states in AlGaN layer. This possibility is ruled out by the fact that the particular features appear only below GaN band edge and are strongly suppressed by 325 nm pump laser. Hence, it is confirmed that feature-6 and 7 are originating due to resonant

excitation in deep trap states lying in the accumulation region near AlN/GaN heterointerface. The enhancement of SPV signal related to GaN band edge, features-6 and 7 can be explained by considering the temperature dependence of background carrier density which is expected to reduce at low temperature. At room temperature, the background carrier density is much higher than the photo-generated carrier density. Thus a negligible SPV in the above bandgap region of GaN is measured at room temperature as shown in Fig. 3.8 (a). With decreasing temperature, the background carrier density decreases due to low activation of electrons from shallow donors. When photo-generated carrier density exceeds background carrier density in the accumulation region, the spatial separation of them is prominent and therefore contributes to the SPV signal.

3.4.2 PL and PLE Characterization

It is of considerable interest to find some correlation between the sub-bandgap states seen in the SPS spectra with YL feature which is one of most intriguing sub-bandgap PL feature observed in GaN. In order to do so, we have performed complementary PL and PLE measurements. Figure 3.10 (a) shows the room temperature PL spectrum which is recorded with 325 nm laser as an excitation source. In PL spectrum, FX_A feature is observed at 3.43 eV whereas a broad YL peak superimposed with interference oscillations is observed at 2.19 eV. Figure 3.10 (b) shows the room temperature PLE spectrum where the detection wavelength is set to YL peak of PL spectrum. In PLE spectrum, YL signal starts to appear above 3.25 eV where a strong peak is observed at 3.4 eV. The appearance of PLE with above bandgap excitation indicates the presence of YL related defects in the accumulation region near AlN/GaN

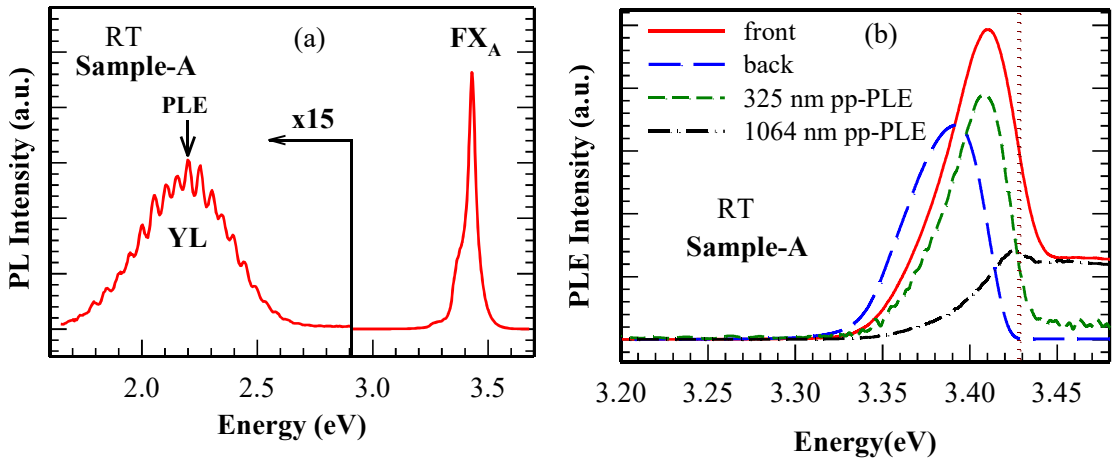

Figure 3.10 (a) Room temperature PL spectra of Sample-A which is recorded with 325 nm laser as an excitation source; (b) room temperature PLE and pump-probe PLE spectra corresponding to yellow luminescence of Sample-A sample. The symbols FX_A and YL corresponds to free exciton-A and yellow luminescence respectively. pump-probe PLE measurements are performed from front surface.

interface. It is interesting to see that the energy of sub-bandgap PLE peak matches reasonably well with that of the feature-3 in SPS spectrum shown in Fig. 3.5 (a). It indicates that the sub-bandgap PLE feature is related to process-3 shown in Fig. 3.6. In order to pinpoint the location of YL feature, PLE measurements are also carried out from the back side of the sample and the spectrum is shown in Fig. 3.10 (b). It is found that the above bandgap PLE signal disappears almost completely and a strong PLE peak is seen at 3.39 eV. Note that the above bandgap excitation will be significantly absorbed by the 3.5 µm thick Fe-GaN template. Negligible above bandgap PLE signal is an indication of a low density of YL related defect states in Fe-GaN template. A weak YL is already reported in Fe-GaN epilayers by other researchers.[179] However, a strong peak is still observed at 3.39 eV in the PLE spectrum recorded from the backside of the sample which clearly indicates that the YL feature is originating from undoped GaN layer. Note that a sub-bandgap excitation beam can excite electron-hole pairs throughout the GaN

layer. An apparent red shift of PLE peak with respect to the front excitation appears mainly due to the absorption of high energy tail of excitation beam in 3.5 μm thick Fe-GaN layer before it reaches the undoped GaN layer. Further confirmation about the spatial location of YL feature can be obtained from the pump-probe PLE measurements performed with 325 nm laser as the pump beam and the results are shown in Fig. 3.10 (b). Here too, the above bandgap PLE signal is suppressed strongly whereas sharp PLE peak is still evident at 3.4 eV. Note that the pump laser beam is strongly absorbed near the AlGaN/GaN interface, which saturates the deep levels responsible for the generation of YL feature in accumulation layer. Therefore, the above bandgap probe beam does not make a measurable contribution to YL feature. On the other hand, sub-bandgap probe beam penetrates deep into the GaN layer. That is why the intensity of PLE peak at 3.4 eV is not significantly affected by the above bandgap pump beam. This means that the sub-bandgap PLE peak is originating from deep inside the undoped GaN layer. The changes observed in pump-probe PLE measurements indicate that the defect states related to YL feature are present throughout the undoped GaN layer including accumulation and depletion region. In order to find out the spectral origin of YL band, Pump-probe PLE measurements are also performed by using a sub-bandgap 1064 nm CW laser as shown in Fig. 3.10 (b). It is seen that the sharp PLE peak is strongly suppressed by the sub-bandgap pump beam whereas above bandgap PLE signal is reduced only by ~10%. Further, free exciton (FX_A) feature is also observed in presence of 1064 nm laser as marked by a vertical dashed line in Fig. 3.10 (b). Note that the energy of 1064 nm probe laser beam is not large enough for observing the resonant excitation in YL defect complex. Therefore, a complete depletion of YL defect states by 1064 nm pump beam is not possible. Suppression of YL feature in presence of a sub-bandgap

excitation is already reported by other researchers[81, 90] where they considered the existence of a deep trap state 1 eV above the valence band. In order to get more insight of 1064 nm laser intensity dependence on YL band, the variation of PLE signal is investigated as a function of pump and probe beam and the same is discussed in the subsequent part of this chapter. The observation of YL at 2.19 eV and their correlation with SPS features at 0.9 eV and 2.8 eV in our work indicates that the features are associated with C_N-O_N deep donor complex.[77, 78, 80] Absence of green luminescence band at high excitation intensity further certifies C_N-O_N donor complex to be the main source of YL band in our sample. It is in strong corroboration with the results obtained by other researchers.[77]

3.4.2.1 Recombination Model

To understand the results of pump-probe PLE measurements, we implement a phenomenological model involving a three-level system which is based on the model proposed by Julkarnain *et al*.[81] and is shown schematically in Fig. 3.11 (a). Above bandgap optical excitation injects electrons and holes in the respective bands in GaN. At room temperature, shallow donor states are assumed to be in thermal equilibrium with the conduction band (E_C). A fraction of the photo-generated holes in the valence band (E_V) are captured by the deep trap state (E_{DS}). Recombination of electrons in E_C with holes in E_V provides band-to-band or excitonic recombination in GaN whereas recombination of electrons in E_C with the holes captured by E_{DS} provides YL feature. Due to the excitation by 1064 nm laser, electrons are excited to the unoccupied deep trap

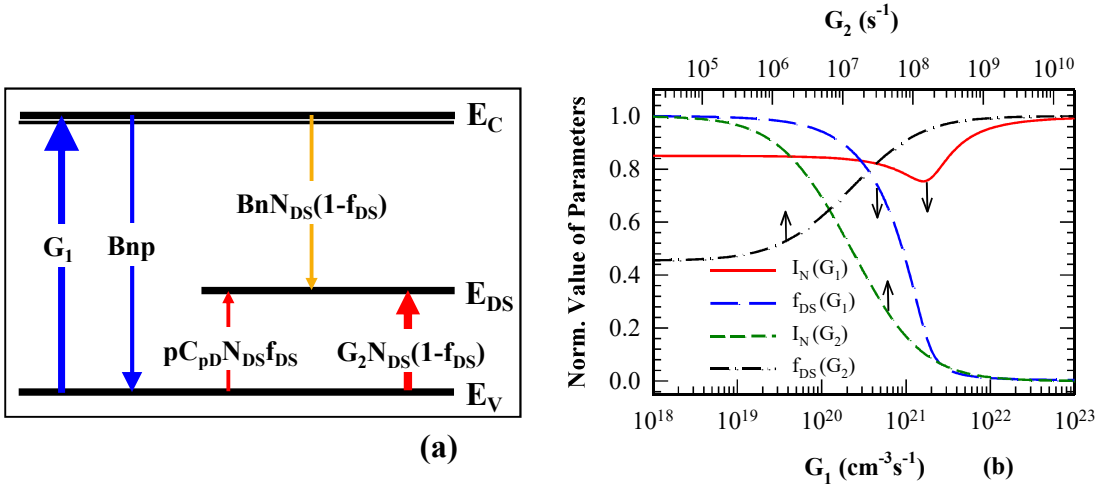

Figure 3.11 (a) A schematic diagram to illustrate the absorption and emission processes in undoped GaN layer. E_C, E_V, E_{DS}, N_{DS}, f_{DS}, G_1, G_2, n, p, B, and C_{pD} corresponds to conduction band, valence band, deep trap state, density of deep trap state, occupation function of deep trap state, generation rate by probe beam, generation rate by sub-bandgap pump beam, density of electron in E_C, density of holes in E_V, radiative recombination coefficient and hole capture coefficient of E_{DS} respectively; (b) Numerically simulated values of the normalized intensity (I_N) of YL feature and occupation probability of deep trap states (f_{DS}) plotted as a function of the intensity of probe beam (G_1) at a given value of intensity of sub-bandgap pump beam (G_2). Similarly, the variation of I_N and f_{DS} is also shown as a function of G_2 for a given value of G_1.

states while holes are created in E_V. Considering charge neutrality condition, the rate equations are given as follows,[81]

$$\frac{dn}{dt} = G_1 - Bnp - BnN_{DS}(1 - f_{DS}) = 0 \tag{3.2}$$

$$\frac{df_{DS}}{dt} = Bn(1 - f_{DS}) - pC_{pD}f_{DS} + G_2(1 - f_{DS}) = 0 \tag{3.3}$$

$$\frac{dp}{dt} = G_1 - Bnp - pC_{pD}f_{DS}N_{DS} + G_2(1 - f_{DS})N_{DS} = 0 \tag{3.4}$$

$$n = p + N_{DS}(1 - f_{DS}) + N_{SD} \tag{3.5}$$

where G_1 [$cm^{-3}s^{-1}$] and G_2 [s^{-1}] stand for the generation rate corresponding to the probe beam excitation and sub-bandgap pump beam excitation respectively, B[cm^3s^{-1}] is the radiative recombination coefficient, C_{pD}[cm^3s^{-1}] is the hole capture coefficient of E_{DS}, N_{DS}[cm^{-3}] is the density of E_{DS}, f_{DS} is the electron occupation function of the E_{DS}, N_{SD} [cm^{-3}] is the shallow donor density which is considered to be fully ionized and thus correspond to the background carrier density. The third term in Eq. 3.2 is proportional to intensity (I_{YL}) of YL feature. The set of equations are solved numerically and the dependencies of n, p and f_{DS} on G_1 (G_2) for a given value of G_2 (G_1) are estimated by taking the appropriate value of parameters N_{SD}, B, N_{DS} and C_{pD}. The value of G_1 is estimated from the intensity of above bandgap excitation beam. G_2 can't be estimated from the intensity of sub-bandgap excitation as the absorption coefficient is unknown at this energy. In view of this, a normalization factor is considered in order to match G_2 dependence with the experimental data. The parameter related to defect states are taken similar to the reported data[81] as N_{SD}=5x10^{16} cm^{-3}, B=1x10^{-11} cm^3s^{-1}, N_{DS}=3.3x10^{15} cm^{-3} and C_{pD}=5x10^{-9} cm^3s^{-1}. The values of I_{YL} are numerically estimated as a function G_1 where the ratio $\frac{I_{YL}(G_2 \neq 0)}{I_{YL}(G_2 = 0)}$ is defined as the normalized PL intensity (I_N). A fractional decrease in I_N indicates an effective suppression of YL feature when the sample is subjected to secondary sub-bandgap excitation under pump-probe PLE configuration. Figure 3.11 (b) shows the numerically calculated values of I_N and f_{DS} as a function of G_1 for a given value of G_2 =10^6 s^{-1}. At low G_1 (10^{18} $cm^{-3}s^{-1}$), the value of f_{DS} is close to unity which is seen to fall with G_1. It is due to the enhanced capture of photo-generated holes ($pC_{pD}N_{DS}f_{DS}$) by the deep trap states. However, these holes are effectively neutralized by

the sub-bandgap pump beam in pump-probe PLE with a rate of $G_2N_{DS}(1-f_{DS})$. A fall in f_{DS} with G_1 supports an increased absorption of sub-bandgap pump beam by the deep trap states leading to the reduction of I_N as shown in Fig. 3.11 (b). However, above a critical value of G_1, the value of f_{DS} becomes very small. Under such circumstances, the capture of holes by the deep trap states supersedes the neutralization effect of sub-bandgap pump beam. It supports a steady rise of I_N as shown in Fig. 3.11 (b). Next, the variation of I_N and f_{DS} with G_2 is numerically simulated where the values of I_N and f_{DS} are plotted as a function G_2 at a given value of $G_1=10^{21}$ $cm^{-3}s^{-1}$ in Fig. 3.11 (b). Due to the finite value of G_1, initial value of $f_{DS}(G_2)$ is set to 0.45 in absence of G_2. In presence of sub-bandgap pump laser, f_{DS} rises as a function of G_2 due to the filling of deep trap states as shown in Fig. 3.11 (b). It causes a sharp fall in the values of I_N. It therefore explains the neutralization effect of the sub-bandgap pump beam for a given value of the probe beam intensity.

Note that the coefficient B is taken to be same in eqn. 3.2 for the two radiative transitions for the purpose of simplicity. This is a good assumption in our case since the values of normalized PL intensity are plotted. If we consider the coefficient B to be different for the two-recombination processes then the absolute value of intensity will vary. However, it will not lead to any significant change in our analysis. Note that the absolute values of G_1 and G_2 and their temperature dependences are not well established in case of nitrides. A similar assumption has also been taken by other researchers while solving the rate equations in nitride semiconductors.[81]

It is of considerable interest to know if the intensity dependence of I_N as predicted by the numerical simulations in Fig. 3.11 (b) can be confirmed by the experiments. Intensity dependent pump-probe PLE measurements are performed at two values of the

excitation energy on either side of the GaN band edge where the values of I_N are measured as a function of probe beam intensity as shown in Fig. 3.12 (a). The values of G_1 corresponding to the intensity of 3.82 eV pump beam are shown on the upper x-axis. These measurements are carried out at a constant flux of 2.5 W/cm^2 of 1064 nm pump laser beam. For PLE measurements at 3.37 eV (low energy tail of the sub-bandgap PLE peak shown in Fig. 3.10 (b)) the probe beam is obtained by using a xenon lamp and monochromator assembly while for the PLE measurements at ~3.82 eV, He-Cd laser is used as the probe beam. The intensity of probe beam is varied with the help of a circularly variable neutral density filter. In case of probe beam intensity dependence at 3.82 eV, I_N is measured to be 0.97 at very low excitation intensity which decreases up to 0.76 at an excitation intensity of $2x10^{-2}$ W/cm^2. Thereafter, the value of I_N increases with the intensity of the probe beam. It is obvious that the trends shown in Fig. 3.12 (a) are in reasonably agreement with the results of numerical simulations shown in Fig. 3.11 (b). A minor deviation in the values of I_N between simulation and experiments appears due to the simplicity of proposed model. In case of intensity dependence at 3.37 eV, a similar variation is seen however the dip is observed at a lower intensity ($5x10^{-4}$ W/cm^2) of the. probe beam. Moreover, the initial value of I_N turns out to be relatively small when compared with the above bandgap measurements. Due to the low absorption coefficient, the value of G_1 at 3.37 eV is much lower than that at 3.82 eV for the same excitation

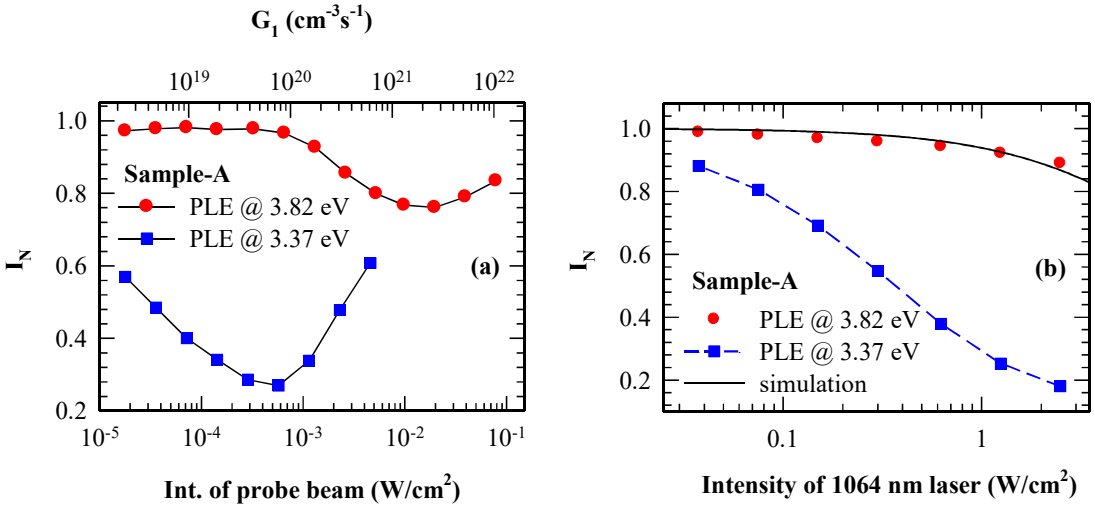

Figure 3.12 (a) Normalized PL intensity (I_N) of YL feature plotted as a function of probe beam intensity at two excitation energies under pump-probe PLE configuration. The G_1 corresponding to the excitation intensity of 3.82 eV excitation is shown in upper x-axis. (b) Normalized PL intensity (I_N) of YL feature plotted as a function of pump beam (1064 nm laser) intensity at two excitation energies under pump-probe PLE configuration. Numerically simulated variation of I_N (solid line) at 3.82 eV excitation energy is also shown.

intensity. Ideally one expects that the initial value of I_N shall be close to unity and the dip in I_N should appear at large intensity of the probe beam. In order to understand the contradictory observation made here, presence of empty deep trap states near the undoped GaN/Fe-GaN interface is essential and the same is being discussed in the next few paragraphs.

The variation of I_N at the two energy values as a function of sub-bandgap pump beam intensity for a fixed probe beam intensity of $1x10^{-3}$ W/cm^2 is shown in Fig. 3.12 (b). In strong corroboration with the numerical simulations, a moderate fall in I_N with pump beam intensity is seen when pump-probe PLE is measured at 3.82 eV. However, the values of I_N at 3.37 eV fall sharply with the pump beam intensity. Ideally a low fall

in I_N is expected with 3.37 eV excitation due to low absorption coefficient. The difference in the behavior of I_N when measured on either side of the bandgap of GaN channel layer can be explained by considering the spatial location of deep trap states. In case of 3.37 eV PLE, YL is mainly generated within the depletion region at GaN/Fe-GaN interface. The upward band bending in this region indicates the majority of shallow donor states and a fraction of deep trap states lying at GaN/Fe-GaN interface are empty even in absence of probe beam excitation. A sub-bandgap PLE feature therefore is due to the resonant excitation to the empty shallow donor states within the depletion region at GaN/Fe-GaN interface. Abundance of empty deep trap states in this region ensures the generation of a strong YL feature in absence of pump laser beam. This is the reason why a strong PLE peak is observed at ~3.4 eV in Fig. 3.10 (b). In case of pump-probe PLE measurements, a strong absorption of sub-bandgap pump beam (1064 nm) by the empty deep trap state causes a large increase in f_{DS} which therefore suppresses I_N considerably as shown in Fig. 3.12 (a) and (b). On the other hand, YL feature with excitation at 3.82 eV is mainly generated via the deep trap states lying in the accumulation region near AlGaN/GaN heterointerface. The pump beam of 1064 nm laser is only weakly absorbed in this region due to a large value of f_{DS}. That's why only a slight fall in I_N is seen at 3.82 eV pump-probe PLE as shown in Fig. 3.12 (b). Hence, it is the effective absorption of pump beam which is significantly large in case of PLE measurements at 3.37 eV and governs a large variation of I_N with G_1 and G_2. It therefore explains the observation of a strong suppression of PLE signal at 3.4 eV compared to the above bandgap PLE signal. Note that, the consideration of a high density of deep trap states in the depletion region can explain the observation of strong YL generation in this region[94] but can't explain the

1064 nm pump laser dependence of I_N. One needs to consider the occupation of the deep trap states while making comment on their spatial location from PL measurements.

It is rather surprising to see that a simple phenomenological model based on the flat band conditions, as shown in Fig. 3.11, is able to provide a satisfactory match between the numerical simulations and experimental observation, as also shown in Fig. 3.12. Ideally, one cannot use such a model to explain the phenomena occurring in the accumulation and depletion regions. However, by using a probe beam of 3.82 eV in pump probe spectroscopic configuration, one is essentially probing the accumulation region. Note that the penetration depth of 3.82 eV probe beam in GaN is about 100 nm whereas the width of accumulation region is only few nm.[146] Hence, one essentially probe the quasi-flat region of GaN while performing the pump-probe PLE measurements at 3.82 eV and therefore the model is applicable here. Moreover, only relative variations and not the absolute magnitudes are discussed in our measurements. It is the primary reason why we get a reasonable match between numerical simulations and experiment results at 3.82 eV. However, the model is indeed invalid in case of 3.37 eV measurements since the probe beam is going to excite carrier in the depletion region. It is the reason why a match between the simulations and experiments cannot be obtained and therefore effect of pump beam at 3.37 eV measurements is discussed only qualitatively.

3.5 Conclusion

SPS and PL and PLE measurements are performed in conventional and pump-probe configurations to identify the spatial and spectral origin of dominating defects

present in n-GaN epitaxial layer, heavily Mg doped p-GaN epitaxial layer and AlGaN/AlN/GaN HEMT structures. In case of p-GaN, BL band is observed at ~2.8 eV in PL spectra which is found to be in perfect agreement with a unique feature at the same energy of the SPS spectra. The SPS phase spectrum at room temperature indicates that electron gets free in this transition. The appearance of the particular SPS feature at low temperature and the temperature dependence of BL band reveals that the SPS feature is due to deep state at 0.55 eV above the valence band to conduction band transition. The optical transition from conduction band/ shallow donor state to the deep acceptor state is responsible for the origin of BL band. In case of AlGaN/AlN/GaN HEMT structure, several SPS features are observed which are strongly corroborated by the PL and PLE measurements. Pump-probe SPS and PLE measurements provide useful information related to the identification and spatial location of defect levels in AlGaN/GaN heterostructures. Suppression of a SPS feature by 325nm laser in pump-probe configuration indicates that the particular feature is originating from the accumulation region lying at AlGaN/GaN heterointerface. On the other hand, suppression of a SPS feature under the exposure of 1064 nm pump laser indicate about its existence in undoped GaN layer and at GaN/Fe-GaN interface. No obvious change in the phase spectra is recorded under the front and back illumination configurations which infers about the absence of Dember contribution in SPS spectra. A deep trap states is found to be located at ~1 eV above the valence band. Such states act as a recombination center where both the valence band to deep trap states and deep trap states to conduction band excitations are possible. Depending on the band profile and occupation probability, SPS signatures related to resonant excitation from deep trap states to conduction band are observed at 2.8 eV from the depletion and accumulation region of GaN channel layer. The same deep

state is found to be responsible for the origin of YL band in GaN. Deep trap states associated with YL band are found to be distributed throughout the sample, however a strong contribution in YL band arises from the defect states lying in the depletion region at GaN/Fe-GaN interface. A phenomenological model is proposed to explain the intensity dependence of YL band and that of the sub-bandgap SPS features as a function of the intensity of pump beam.

Chapter 4

Identification of 2-dimensional Electron Gas Present in AlGaN/AlN/GaN Heterostructure by Spectroscopic Techniques

4.1 Introduction

Formation of the two-dimensional electron gas (2DEG) in AlGaN/GaN heterostructures is critical for the successful operation of nitride based high electron mobility transistor (HEMT) devices. The 2D-electron gas is spatially separated from the ionized donors and therefore have less ionized impurity scattering probability and possess high carrier mobility.[14] A large density of 2DEG at AlGaN/GaN hetero-interface occurs due to the strong polarization discontinuities.[41] The most confirmatory evidence of 2DEG presence at AlGaN/GaN heterointerface is given by the observation of Shubnikov-de Hass (SdH) oscillations in magneto-transport measurements [130-132, 180]. However, one requires high magnetic field and liquid helium temperatures for observing the SdH oscillations. Furthermore, the technique is destructive since one needs to make metallic contacts. In view of this, optical characterization techniques like photoluminescence (PL) are very attractive due to their contactless nature. Several reports are already available on the optical characterization of AlGaN/GaN

heterostructures [130, 133, 134, 136, 137, 181, 182], where researchers apply several tricks to identify the 2DEG features in PL spectra. For example, the disappearance of a PL peak after careful etching of AlGaN barrier layer is considered to be one of the most direct method for identifying the 2DEG related features [130, 137, 181]. However, the information might be ambiguous under certain cases since the particular PL peak might be associated with some defect level of AlGaN/GaN interface [182]. Due to these reasons, 2DEG related transitions of AlGaN/GaN heterostructures are usually identified by performing systematic temperature and intensity dependent PL measurements [45, 130, 135-137], where PL features related to 2DEG are seen to redshift (blueshift) with temperature (excitation intensity) respectively. However, there are some discrepancies. For example, Shen *et al.*[45] reported a blue shift of < 4meV whereas Nam *et al.*[136] reported a blue shift of > 50 meV for the 2DEG feature. Such a large variation puts a doubt on the identification of 2DEG features in the low temperature PL spectrum. Moreover, a few researchers assign a shoulder peak in the sub-bandgap region of GaN as the 2DEG feature [45, 133] while the others report a broad 2DEG PL peak superimposed with peculiar oscillatory features [134-137, 182]. Surprisingly, the oscillatory features also show a similar temperature and intensity dependent behavior. Most of the researchers therefore claimed that the oscillatory features are related to 2DEG sub-levels of AlGaN/GaN heterostructures [133-138]. An electric field ~90 kV/cm at the triangular potential well is also estimated by Nam *et al.* by treating the fine oscillations as 2DEG sub-levels. On the contrary, 2DEG sub-levels are also theoretically predicted through a self-consistent solution of Schrödinger and Poisson equations for AlGaN/GaN heterostructures where maximum two sub-levels of 2DEG is found below Fermi level.[133] No clarity about the identity of 2DEG in the low temperature PL spectrum of AlGaN/AlN/GaN heterostructure therefore exists.

This chapter mainly focuses on the identification and characterization of 2DEG related feature in PL spectra. We explore the origin of these oscillatory features by performing angle dependent PL measurements. Contrary to the present understanding, we find that the fine oscillatory features are not at all related to 2DEG sub-levels rather these are nothing but the interference oscillations. Identity of 2DEG features is also confirmed by comparing the PL spectra of as grown and top barrier layer etched samples. Peculiar temperature and excitation power dependencies of broad PL peaks provide further confirmatory evidences for an unambiguous identification of the ground and exited states 2DEG features. A methodology is presented though which 2DEG features in the PL spectra can be unambiguously identified without even etching the top barrier layer.

4.2 Sample Details

AlGaN/AlN/GaN heterostructure used in the study is the same sample (Sample-A) which was used to characterize defects in **chapter 3**. It is grown by using Ammonia molecular beam epitaxy (MBE) system on c-plane Fe-GaN templates which is grown on sapphire substrate. The layer structure consists of 25 nm undoped $Al_{0.33}Ga_{0.67}N$ barrier layer, 1 nm AlN inter-layer, 1 μm undoped GaN channel layer, 200 nm lightly Mg-doped GaN buffer layer grown on 3.5 μm thick Fe-doped GaN template.

4.3 Origin of Fine Oscillation in 2DEG PL Spectrum

In order to identify the 2DEG PL signature, we have performed temperature and excitation intensity dependent PL measurements on Sample-A at low temperature. Figure 4.1 (a) shows the temperature dependent PL spectra of Sample-A at few selective temperatures which is recorded with 0.02 W/cm^2 excitation intensity. At 10 K, the band edge PL spectra is dominated by donor bound excitonic transition (D^0X) at 3.488 eV which is generally observed in the low temperature PL spectra of GaN epitaxial layers.[142, 183-185] The feature lying at 3.493 eV is A-exciton feature (FX_A) while the feature obtained at 3.513 eV is related to excited state of FX_A(n=2). The phonon replica of bound exciton feature ($LO_D{}^oX$) is also seen in Fig. 4.1. In addition to these features, two broad PL feature (E_0 and E_1) at ~3.36 eV and 3.47 eV are also seen. Note that the broad features are composed of several fine features. Surprisingly, these fine oscillatory features show a temperature dependent behavior similar to the 2DEG sub-level features reported by other researchers.[45, 137, 181] The energy gap (ΔE) between a particular fine feature and FX_A is found to decrease with increasing temperature which can be appreciated from the shift of the features with respect to vertical dashed line in Fig. 4.1 (a). Further, the excitation intensity dependent PL measurements are performed on Sample-A where the spectra at few excitation intensities are shown in Fig. 4.1 (b). The excitation intensity dependent small blueshift of particular fine oscillation peak, as can be appreciated with respect to the vertical dashed line, is also similar to reported data.[137] On the basis of these observations, we tentatively assign the broad feature as 2DEG related feature while the fine oscillations are labelled as the signatures of sub-levels of 2DEG formed at the AlGaN/GaN heterointerface. Such an assignment of PL features is reasonably consistent

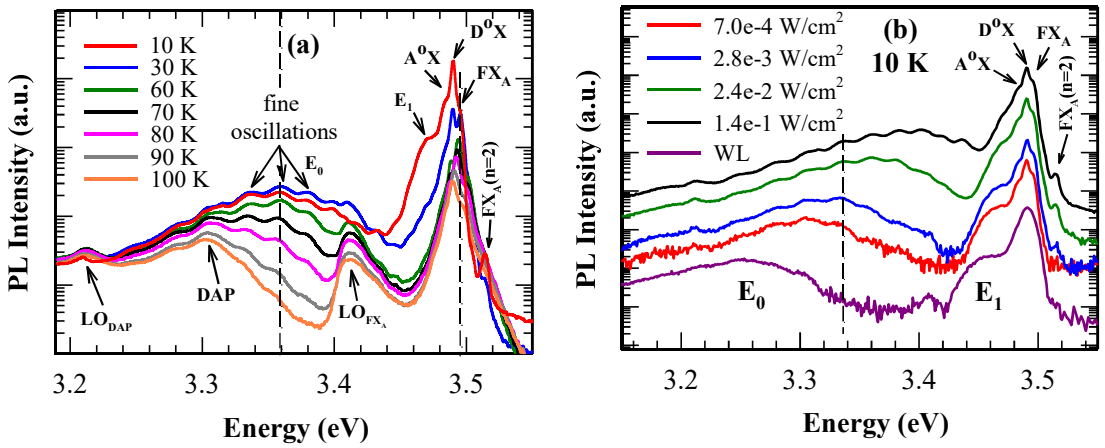

Figure 4.1 (a) Temperature dependent PL spectra of AlGaN/AlN/GaN heterostructures (Sample-A) recorded at 0.02 W/cm^2 excitation intensity; (b) excitation intensity dependent PL spectra of Sample-A at 10 K where WL stands for the white light excitation sources tuned at 325 nm. The symbols D^0X, A^0X, FX_A, and $FX_A(n=2)$ stand for the donor bound exciton, acceptor bound exciton, free A-exciton, and the excited state of free A-exciton transitions of GaN while DAP stands for the Donor-acceptor pair (DAP) transition respectively. The phonon replicas of DAP and D^0X are labelled as LO_{DAP} and LO_{D^0X} respectively. Two broad features superimposed with several fine oscillations, labelled as E_0 and E_1, are related to the 2DEG at AlN/GaN heterointerface. Vertical dashed lines are drawn at a particular fine oscillation and at FX_A to visualize temperature and excitation intensity dependent shift.

with the published literature.[130, 136, 183, 184] However, there are approximately two to nine such 2DEG sub-levels which are separated by ~ 30 meV present in the PL spectra as can be appreciated from Fig. 4.1. With triangular potential approximation, we have estimated an electric field of 80 kV/cm from the peak energies of the fine features which is surprisingly low enough in nitride based heterostructures. In order to get further clarity, Schrödinger and Poisson equations are solved self-consistently for Sample-A at 300 K.[176, 186] The potential profile and first two envelop functions are shown in Fig. 4.2. Only two sub-levels are found below Fermi level which are separated by around 160 meV.

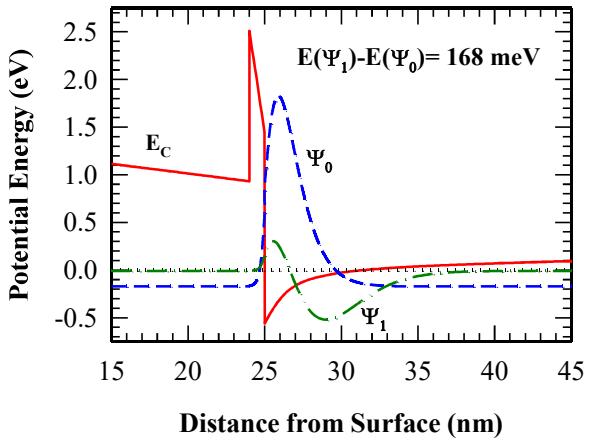

Figure 4.2 The conduction band profile and electron wave functions of Sample-A. The symbols E_C, Ψ_0, Ψ_1 corresponds to conduction band, ground state electron wave function and excited state wave function respectively. The wave functions are vertically shifted to the corresponding eigenenergies. The dotted line corresponds to Fermi level.

Therefore, the identification of oscillatory features as the sub-levels of 2DEG is questionable. Nevertheless, an additional possibility still remains that the fine oscillations might be related to some interference phenomenon. Note that the AlGaN/AlN/GaN HEMT structure is a multilayer architecture and possibility of interference in spectroscopic measurements can't be ruled out. In view of this, we have performed angle dependent PL measurements on Sample-A where the PL signal is collected at different angles with respect to the surface normal as schematically shown in Fig. 4.3. The representative PL spectra at few selective angles are shown in Fig. 4.4. These measurements are performed at large excitation intensity ~ 60 W/cm^2 for which the broad peak is shifted to higher energy. PL plots are vertically shifted for the clarity in viewing. The band edge PL features and its phonon replicas do not show any angle dependence. However, the fine oscillatory PL features vary significantly with the angle of viewing. It provides a clear hint that the oscillatory features in Fig. 4.1 are not related to 2DEG sub-

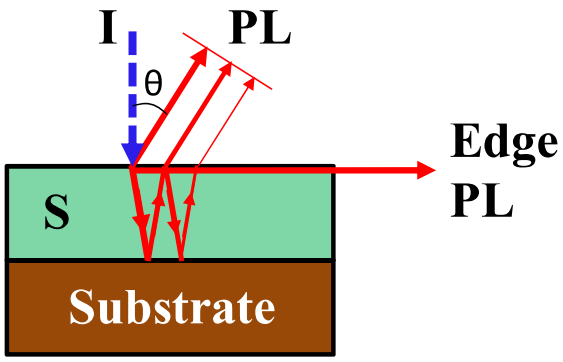

Figure 4.3 Schematic of angle dependent PL and edge PL measurements. I, S and θ corresponds to excitation, sample and collection angle respectively.

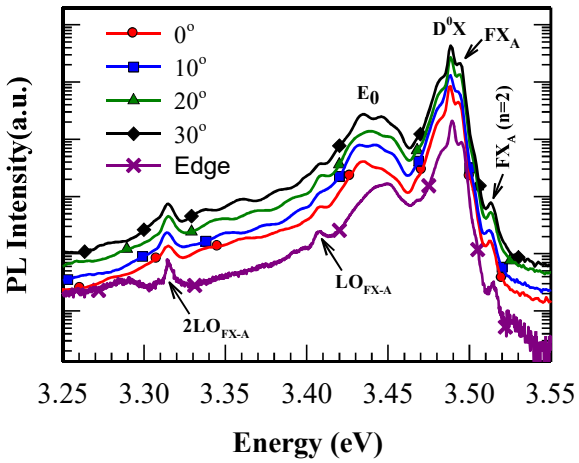

Figure 4.4 Angle dependent 10 K Photoluminescence spectra of sample-A where the viewing angle is measured from the surface normal. In case of edge PL, sample is excited from the front surface whereas the luminescence is collected from the edge (90°). The spectra are recorded with an excitation intensity of ~60 W/cm^2. D^0X, FX_A, and FX_A (n=2) stand for the donor bound exciton, free exciton-A, and the excited state of free exciton-A transitions of GaN respectively. The phonon replica of FX_A feature are labelled as LO_{FXA}. A broad feature (E_0) superimposed with several fine oscillations is related to the 2DEG at AlN/GaN heterointerface. The spectra are vertically shifted for clarity.

levels. It is therefore highly possible that the fine oscillatory PL features seen in Fig. 4.4 are governed by an interference phenomenon. For further confirmation we have performed edge PL measurements where the sample is excited from the top and the luminescence is collected from the edge of the sample as shown in Fig. 4.3. In this case, luminescence is not going through multiple interference within the sample and therefore no interference oscillation is expected to appear in PL spectra. In fact, fine oscillation features disappeared in PL spectra when it is collected from the edge of the sample as shown in Fig. 4.4. This evidently confirms that the fine oscillatory features of PL spectrum are related to interference oscillations. Note that, there are several interference oscillations observed on 2DEG PL feature for Sample-A. So in the first glance, one will consider it as interference oscillations. However, the number of interference features might be less depending on the thickness of the sample and the full width at half maximum (FWHM) of 2DEG PL feature where one can misinterpret the interference features as 2DEG sub-levels by following reported characteristics. If the fine features are related to interference oscillations, then why it shows a peculiar temperature dependent redshift and excitation intensity dependent blueshift? It is therefore essential to understand these observations in light of the assignment of oscillatory features as the interference oscillations.

4.3.1 Temperature Dependence of Fine Oscillations

To check this issue, we have performed the temperature dependent reflectivity measurements under normal incidence condition where the representative plots at a few selected temperatures are shown in Fig. 4.5 (a). The reflectivity spectrum exhibit peculiar

features around 3.5eV that are related to the free exciton transitions of GaN.[142, 143, 187] In addition, several strong oscillations are observed in the sub-bandgap region of GaN. Surprisingly, the period of these oscillations perfectly matches with the period of fine oscillations observed in 10 K PL spectrum. It is therefore obvious that the oscillatory features seen either in PL or reflectivity spectrum are related to interference and the period of these oscillations is governed by the thickness of GaN layer. Free exciton features redshift with increasing temperature as illustrated by the vertical dotted line marked at 3.495eV. Interestingly, the oscillatory features seen in the reflectivity spectrum also redshift with increasing temperature as shown by another vertical line marked as '1' in Fig. 4.5 (a). The energy separation (ΔE) between the free exciton (FX_A) and the oscillatory feature '1' is plotted as a function of temperature in Fig. 4.5 (b). For comparison, the value of ΔE for a particular fine oscillation at 3.36 eV is measured from

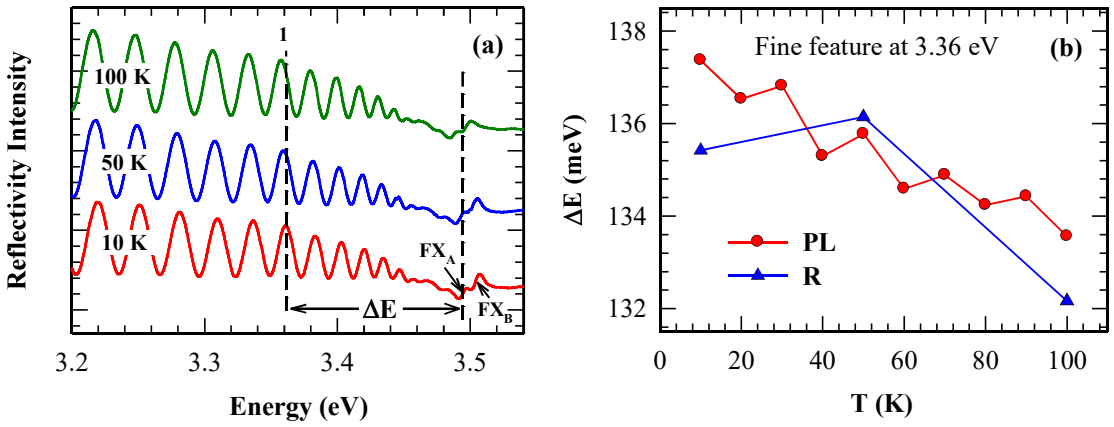

Figure 4.5 (a) Temperature dependent reflectivity spectra of Sample-A which is recorded under normal incidence condition. Vertical dashed line drawn at 3.495 eV and 3.36 eV marks the energy of free exciton-A (FX_A) and a particular oscillation peak (1) at 10 K respectively. The energy difference between FX_A and '1' is schematically marked as ΔE. The symbol FX_B corresponds to free exciton-B. (b) Temperature dependences of ΔE as obtained from reflectivity and PL measurements.

temperature dependent PL spectra (Fig. 4.1 (a)) is also shown in the same figure. It is seen that the value of ΔE reduces by few meV when the sample temperature is raised from 10 K to 100 K. Temperature dependence of the interference oscillations can be understood by considering the temperature dependent rise of refractive index (η) of GaN. The wavelength and temperature dependencies of the refractive index of GaN are described in **Appendix A** and **B** respectively. Another contribution arises from the thermal expansion of GaN where the thickness (d) of GaN layer increases with temperature due to the thermal dilation of lattice. The product of refractive index and layer thickness i.e. (n*d) therefore increases with the sample temperature. It is this factor which is liable for the observed shift of a particular oscillatory peak (m^{th} peak in **Appendix A**) to higher wavelengths. However, the shift is slower than the temperature dependent redshift of band edge of GaN which leads to a decrease in ΔE with increasing temperature. Hence, it is clear that the temperature dependence of ΔE is governed by the variation of refractive index and thickness of GaN layer with temperature.

4.3.2 Excitation Intensity Dependence of Fine Oscillations

Another evidence for considering fine oscillations as 2DEG sub-levels is the blueshift of oscillatory features as a function of excitation intensity which needs to be clarified within the framework of interference phenomenon. Here, we try to reproduce the excitation intensity dependence of 2DEG PL by the following procedure. We find that the broad PL feature, marked as E_0 in Fig. 4.1 (b), can be reasonably fitted with a single Gaussian peak. The 2DEG PL peak can be treated as the convolution of a broad

PL peak and fine interference oscillations. By performing excitation intensity dependent edge PL measurements, it is found that the broad PL peak blueshifts with excitation intensity. For simulation purposes, we take a broad Gaussian function which is obtained from the line shape analysis of excitation dependent PL spectra and superimpose it with the 10 K reflectivity spectrum shown in Fig. 4.5 (a). The outcome of such an exercise is shown in Fig. 4.6 (a). The fine oscillations show an apparent blueshift with excitation intensity as can be seen by comparing the peak position of a fine feature marked by putting a vertical dotted line in Fig. 4.6 (a). The simulated apparent peak energy of a particular feature at 3.334 eV is plotted as a function of excitation intensity in Fig. 4.6 (b). For comparison, the excitation intensity dependence of one of oscillatory features, seen at 3.331 eV in Fig. 4.1(b), is also plotted in Fig. 4.6 (b). It is found that simulated

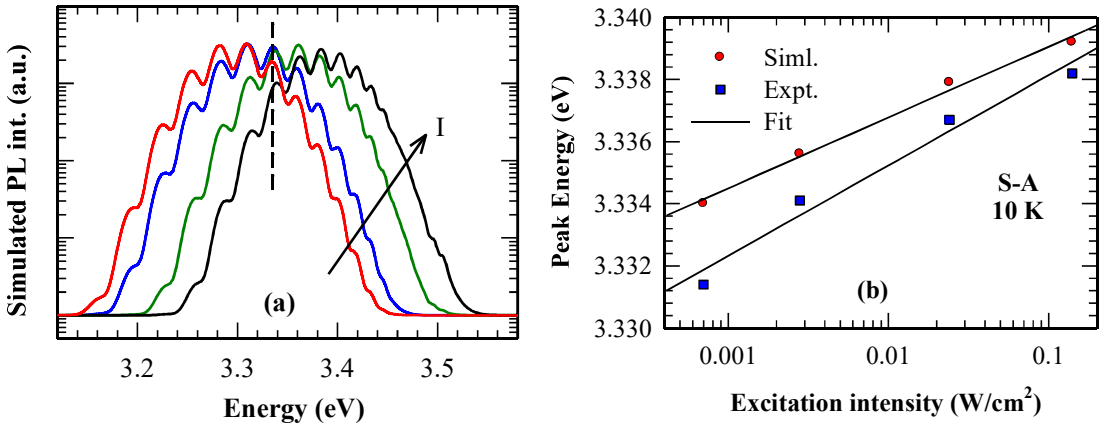

Figure 4.6 (a) The simulated excitation intensity dependent PL spectra which is obtained from the convolution of broad Gaussian peak with 10K reflectivity spectrum. The broad Gaussian peak for different excitation intensity is obtained by fitting E_0 PL peak in Fig. 4.1 (b). The symbol I stands for laser intensity. Excitation intensity dependence of peak energy of one of the fine oscillations, marked by a vertical dashed line, is also shown. (b) Excitation intensity dependence of fine oscillation peak which is obtained from simulation and experiment.

excitation intensity dependence reasonably follows the experimental excitation intensity curve. Hence, it is obvious that the excitation intensity dependent blueshift of oscillatory features is governed by the blue shift of broad PL peak. It reasonably explains why the fine features blueshift with excitation intensity even though these are the usual interference oscillations. The oscillatory peaks do not shift at all with excitation intensity, and a small blueshift (< 10 meV) is artificially induced by the broad PL peak that shifts by more than 100 meV with laser intensity. It is confirmed here that the fine oscillations are not at all related to the sub-levels of 2DEG. The fundamental mechanism of these oscillations is governed by the interference phenomenon.

Finally, it is worth to discuss the results of a few other researchers who have earlier assigned the fine oscillations in PL spectra as the signature of 2DEG sub-levels of AlGaN/GaN based HEMT structures rather than interference oscillations. We tried to estimate the thickness of GaN layer by assuming the fine features seen by them as interference oscillations. In order to obtain the thickness information, a knowledge of refractive index dispersion along with its temperature dependence is a priori. Unfortunately, this information is not available for GaN over the wavelength range of our interest. We have used the coefficients of Sellmeier equation from literature,[173, 188-191] however, the estimated thickness information is little scattered. In fact, the 300 K reflectivity spectrum is fitted by Eq. 2.6 using the reported values of refractive index. A reasonable match between the simulated and experimental reflectivity spectrum is achieved only in the long wavelength region above 500 nm as shown in the inset of Fig. 4.7. However, the simulation curve doesn't fit with the reflectivity spectrum near band edge of GaN where 2DEG is present. To get the value of refractive index for the short wavelength region, approaching the band edge of GaN, we follow the procedure given

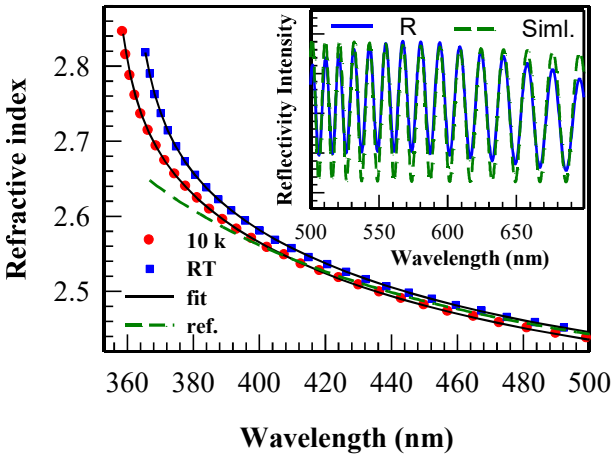

Figure 4.7 Refractive index dispersion of GaN at 10 K and room temperature. Solid lines are the fit with second order Sellmeier equation where the values of coefficients are summarized in Table 4.1. Refractive index dispersion of GaN at 300K which is taken from [189]Ref. 189 is also plotted in the same graph for comparison purpose. Inset shows the experimental and numerically simulated reflectivity spectra for the transparent region of GaN.

below. The numerical simulations of reflectivity spectrum in long wavelength region provides a cavity length (d) of 4.77 μm which matches reasonably well with the planned thickness of GaN layer in our HEMT samples. Thereafter, we use this value of 'd' to estimate the values of refractive index as outlined in **Appendix A**. The wavelength dependence of the refractive index of GaN is shown in Fig. 4.7 at 300 K. The low temperature (10 K) value of refractive index of GaN at 700 nm is thereafter estimated by following the procedure outlined in **Appendix B**. Once again, we use the procedure given in **Appendix A** to find the wavelength dependence of refractive index of GaN at 10 K. Such a plot is also given in Fig. 4.7. The two curves are thereafter fitted by using the second order Sellmeier equation where the values of coefficients are summarized in Table 4.1 for 10 K and 300 K. In all these calculations, the value of extinction coefficient is assumed to be zero, which is valid only for the sub-bandgap region of GaN.

Nevertheless, a non-zero value of extinction coefficient does not affect the period of interference oscillations. It might only dampen the magnitude of reflectivity signal as clearly observed in Fig. 4.5 (a). For comparison purpose, the dispersion curve of GaN taken from [189]ref. 189 is also plotted in Fig. 4.7. Although the values of refractive index measured by us are in good agreement with the values given in [189]ref. 189 for the wavelengths exceeding 500 nm but a clear deviation is observed near the band edge region of GaN. The modified refractive index is used to estimate the thickness. The outcome of such an exercise is shown in Fig. 4.8 where the slope of the plot is inversely proportional to GaN layer thickness. The measured values of GaN thickness AlGaN/GaN HEMT structures are in excellent agreement with the reported values in the corresponding articles.[134-136, 182] It once again confirms that the fine oscillations observed

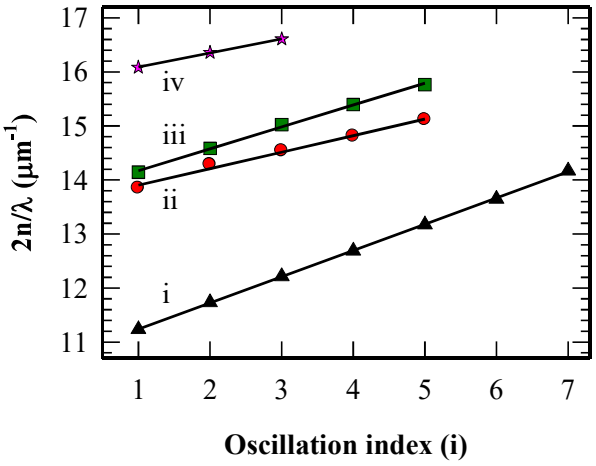

Figure 4.8 Fit of the interference oscillations observed in the PL spectra of AlGaN/GaN based HEMT structures where plots (i), (ii), (iii), and (iv) are made by taking the experimental data based on the low temperature PL spectra from [182]ref. 182, [136]ref. 136, [135]ref. 135 and [134]ref. 134 respectively. Here, the slope of the curve is inversely proportional to the thickness of GaN layer. The estimated (reported) values of GaN layer thickness for the curves (i), (ii), (iii), and (iv) are 2.06 μm (2.03 μm), 3.27 μm (not given), 2.47 μm (2.69 μm), and 3.81 μm (3.28 μm) respectively.

in the low temperature PL spectra of AlGaN/GaN HEMT structures are related to interference phenomenon only.

Temperature	A0	A1	B1 (nm)	A2	B2 (nm)
10 K	3.62 ± 0.07	0.043 ± 0.002	352.0 ± 0.2	1.65 ± 0.06	254.3 ± 2.8
300 K	3.41 ± 0.09	0.055 ± 0.003	356.5 ± 0.3	1.87 ± 0.08	244.5 ± 3.5

Table 4.1 Coefficients of the second order Sellmeier equation given by,

$$n(\lambda) = \sqrt{A_0 + \frac{A_1\lambda^2}{\lambda^2 - B_1^2} + \frac{A_2\lambda^2}{\lambda^2 - B_2^2}}$$

4.4 Identification of 2DEG PL Feature

In the previous section, we have demonstrated reported that the fine oscillations in the PL spectra of AlGaN/AlN/GaN heterostructure are not related to the 2DEG sub-levels, rather those are governed by the interference phenomenon. We also have found that a broad 2DEG related feature on which interference oscillations appears. However, it is of considerable interest to identify whether the broad feature is actually related to 2DEG or not. The simplest procedure for identifying 2DEG PL features is to perform PL measurements on the AlGaN/GaN HEMT sample before and after etching the top AlGaN and AlN barrier layer. The schematic band diagram of as-grown and top barrier etched sample are shown in Fig. 4.9 (a) and (b) respectively. The etched sample is simply an n-type an epitaxial layer where no 2DEG is present. The outcome of PL measurements on as-grown and top barrier etched sample are shown in Fig. 4.10. Several free and bound

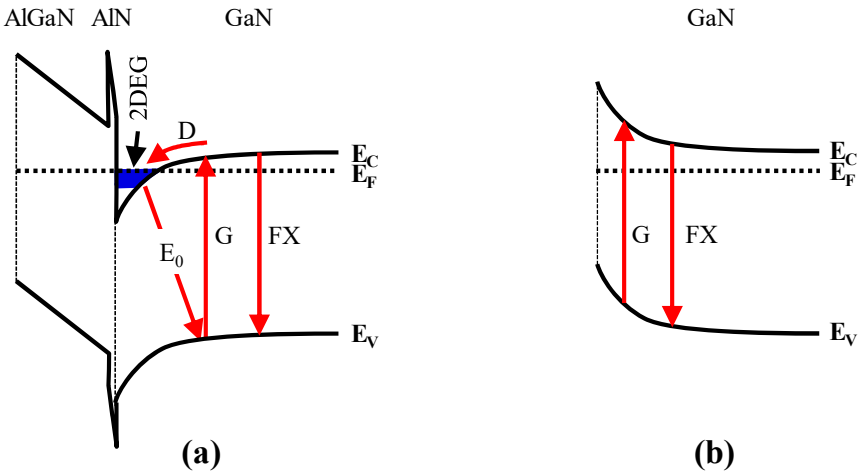

Figure 4.9 Schematic band diagram of (a) as grown AlGaN/AlN/GaN heterostructure (Sample-A) and (b) after etching top AlGaN barrier layer, AlN inter layer and a part of GaN Channel layer. The symbol E_C, E_V and E_F corresponds to conduction band, valence band and Fermi level respectively. G, D, E_0 and FX corresponds to optical excitation, carrier redistribution, 2DEG recombination and free exciton recombination respectively.

exciton features are identified as clearly labelled in figure 4.10 for the as-grown sample.[183, 185] Apart from this, E_0 and E_1 features are also observed at about 3.35 and 3.47 eV in the 10 K PL spectrum. The PL spectrum recorded on the etched sample is also shown in figure 4.10 where the AlGaN barrier layer, AlN inter-layer, and a part of the GaN channel layer (few nm) were etched from one portion of the sample using a reactive ion etching technique. It is observed that E_0 and E_1 completely disappear after etching the top barrier layer. Free exciton (FX_A), neutral donor bound exciton (D^0X) along with its 2 electron replica (D^0X-2e)[183] are clearly observed in the PL spectrum of the etched sample. Apart from this, donor-acceptor pair (DAP) transition, conduction band to acceptor transition (eA), and LO phonon replicas of excitonic, DAP and eA features, which are separated by ~90 meV from the respective PL features, are also clearly observed in figure 4.10. PL measurements shown in figure 4.10 clearly indicate that the

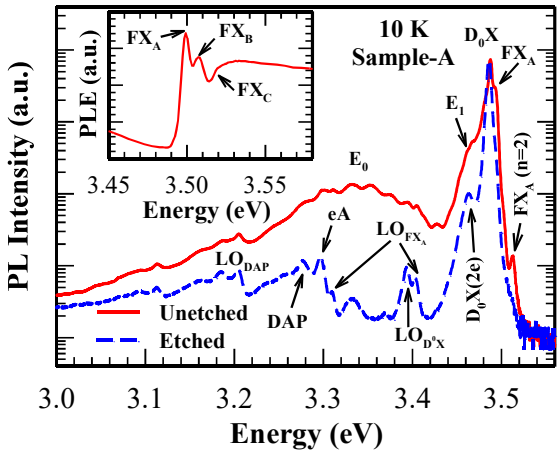

Figure 4.10 10 K PL spectra of Sample-A (unetched) and after etching top AlGaN barrier layer, AlN inter layer and a part of GaN Channel layer (etched). D^0X, FX_A, and FX_A (n=2) stand for the donor bound exciton, free A-exciton, and the excited state of FX_A of GaN while DAP, and eA stand for the donor acceptor pair and conduction band to acceptor transition respectively. D^0X(2e) stands for the two electron replica of the D^0X feature while longitudinal phonon (LO) phonon replicas of DAP, FX_A and D^0X are also shown. Two broad features, labelled as E_0 and E_1, are related to the ground and excited states of 2DEG at the AlGaN/GaN heterointerface, respectively. The inset shows the 10 K PLE spectrum corresponding to the ground state (E_0) PL feature of 2DEG where FX_A, FX_B, and FX_C stand for free exciton features corresponding to the three valence bands of GaN.

origin of E_0 and E_1 PL features lie near the AlN/GaN heterointerface. Note that the AlGaN barrier is transparent to the excitation laser beam hence the possibility of assigning these features as defect related transitions of the AlGaN barrier layer can easily be ruled out. Therefore, the broad PL features are related to either the 2DEG states or some defect/trap states lying at the AlGaN/GaN heterointerface. In this context, PLE measurements can provide useful information related to the origin of broad PL features. A typical PLE spectrum recorded at the peak energy of E_0 feature is shown in the inset of figure 4.10. Free exciton features related to the GaN are clearly seen in the PLE

spectrum. The dominance of GaN exciton edges in PLE spectra indicates about the negligible absorption of excitation beam in the field driven region near the AlN/GaN heterointerface. It further indicates that the photo-excited carriers associated with E_0 features are generated in the flat band region of the GaN layer. Electrons are subsequently confined in the triangular potential well formed at the heterointerface where they recombine with free holes in the quasi-flat valence band region leading to the evolution of E_0 feature. Such a spatially indirect radiative recombination of electrons confined in the triangular potential well with free holes in the valence band indicates that the particular PL feature is related to the 2DEG states.[192] Negligible absorption of the excitation beam in the field driven region of the sample during PLE experiment indicates that E_0 feature is not associated with defects/traps lying at the heterointerface. On the other hand, a few researchers have reported that the 2DEG related PL features might also lie at energies higher than the bandgap of GaN. Such a PL transition had been associated with the recombination of 2DEG electrons with traps lying at the AlGaN/GaN heterointerface.[193, 194] In order to observe such a PL feature, the energy of excitation source needs to be larger than the bandgap of the top AlGaN barrier layer which actually leads to a high possibility of transferring the holes from the AlGaN barrier layer to the interface traps. However, this possibility is ruled out in our case since (1) the energy of excitation laser source in our PL experiments is lower than the bandgap of the AlGaN barrier layer, and (2) no PLE feature related to the AlGaN barrier layer is observed by us. Further, the energy separation between E_0 and E_1 PL features in figure 4.10 matches reasonably well with the numerically calculated energy separation of 2DEG states as shown in Fig. 4.2. Hence, E_0 and E_1 PL features are identified as ground and excited state transitions related to 2DEG lying at the AlN/GaN heterointerface.

4.5 Characterization of 2DEG PL Feature

In the previous sections it is demonstrated that there are only two 2DEG sub-levels below the Fermi level in case of Sample-A. In case of low temperature PL measurements, the electrons in these states recombine with photo-excited holes and contributes to E_0 and E_1 PL bands. A strong interference effect is also observed on 2DEG PL features. It is of considerable interest to characterize the newly assigned 2DEG PL features and also to understand the dominance of interference effect on 2DEG feature. For that, temperature and excitation intensity dependent PL spectra which are shown by Fig. 4.1 need to be reviewed again. At 10 K, two broad features appear in the sub-bandgap region of GaN which indicates a spatially indirect recombination of electrons in 2DEG states and photo-excited holes. The oscillator strength of recombination which corresponds to the overlap integral of 2D-electron and photo-excited hole wave functions, decides the integrated PL intensity of the particular feature. The broadening of the 2DEG PL feature compared to GaN exciton features is mainly associated with the potential fluctuations present at AlN/GaN heterointerface.[195] In addition, the 2DEG density falls exponentially in GaN channel layer after a certain depth. The transition energy also decreases due to decrease in electric field along the depth of the sample. The resultant effect shows a low energy exponential decaying tail in 2DEG PL feature as shown in Fig. 4.1. To include the tailing part in fitting, the PL features are fitted with two Gaussian functions. The dominant PL peak is labelled as the 2DEG ground state (E_0) and excited state (E_1) PL feature.

4.5.1 Temperature Dependence of 2DEG PL Feature

Temperature dependence of the E_0 feature as shown in Fig. 4.1 (a) is analyzed and the same is summarized in Fig. 4.11. It is found that the intensity of the E_0 feature initially increases with temperature up to 30 K and thereafter falls rapidly with rise in temperature. Enhancement of PL intensity with temperature is also reported in the case of multi-quantum well structures.[170, 196] Such a behavior was explained by considering the generation of electron–hole pairs in barrier

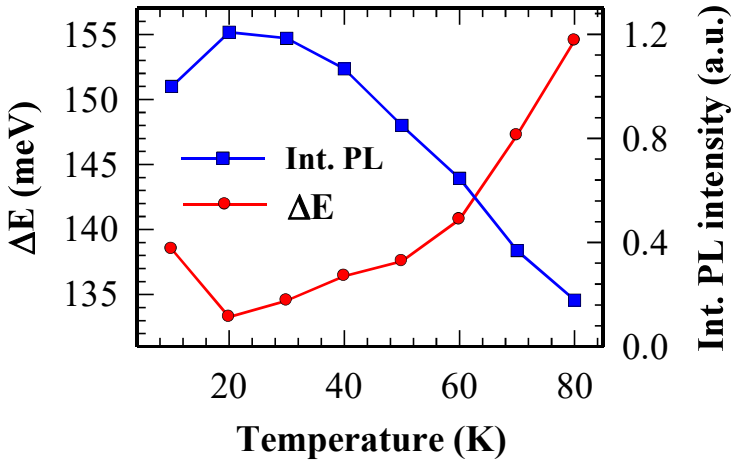

Figure 4.11 Temperature dependence of integrated PL intensity of E_0 feature and the energy separation (ΔE) between the ground state (E_0) feature of 2DEG and GaN free exciton peak (FX_A).

that are more efficiently transferred to well at high temperatures. Initial increase of 2DEG PL intensity with temperature can be explained by considering an efficient transfer of electrons from the flat band region of GaN to the triangular potential well. Further, the thermal activation of lightly bound electrons and subsequent transfer also contribute to enhancement of 2DEG. Note that, efficient transfer of thermally excited electrons from GaN buffer layer to the triangular potential well will screen the electric field. This will

make the triangular potential a bit shallower and a blueshift of the 2DEG PL peak is expected due to screening effect. The energy separation (ΔE) between E_0 and FX_A is shown in Fig. 4.11. A decrease (increase) in ΔE with temperature essentially represents the effective blueshift (redshift) of E_0 due to effects other than thermal shrinkage of bandgap. A decrease of ΔE with increasing temperature up to 30 K is consistent with the above explanation. However, the intensity of the E_0 feature reduces at temperature above 30 K as shown on figure 4.11. It is already known that the 2DEG PL features in general disappear at some critical temperature which is governed by the depth of the triangular potential well.[45, 134, 136, 192] Note that the feature E_0 is located ~ 150 meV below the band edge of GaN as shown in figure 4.1 (a). However, an activation energy of only 38 meV is estimated for E_0 feature from the Arrhenius plot of integrated intensity versus 1000/T (not shown here). A low value of activation energy indicates that the 2DEG ground state in the triangular potential well is filled. By using the 2DEG concentration estimated from Hall measurements, the position of the Fermi level is found to lie near the conduction band edge in the flat band region of the GaN channel layer. Hence, 2DEG carriers near the Fermi level spill out of the triangular potential well even at moderate temperatures causing a significant reduction of the PL intensity. The thermal escape of electrons from the triangular potential well at elevated temperature reduces the 2DEG density which lowers the screening effect. It makes the triangular potential well a bit deeper and provides a redshift of 2DEG features other than the thermal shrinkage of the bandgap of GaN. It is in line with the increase in ΔE with rise in temperature above 30 K as shown in Fig. 4.11. Hence, a cumulative effect of carrier screening and thermal shrinkage of GaN bandgap governs the overall variation of energy separation between the 2DEG and free exciton features of GaN.

However, this might not be the only reason behind a temperature dependent decrease in 2DEG PL intensity. In fact, the 2DEG density is reported to be constant at low temperature and increases at elevated temperature.[197] It is plausible that the diffusion of holes into the bulk of the GaN channel layer can also lead to the decay of 2DEG PL intensity at elevated temperatures. In fact, a sharp increase of hole mobility is already reported for GaN when the temperature is raised towards 100 K.[118] Due to this reason, holes move more swiftly into the bulk GaN layer which reduces the overlap of electron and hole wave functions and therefore reduces their recombination probability with electrons confined in the triangular potential well. The recombination from larger depth leads to redshift the E_0 peak. In addition, background electron density in GaN increases with increasing temperature. At low temperature all the background electrons get freeze out. Therefore, photo-excited holes recombine with either 2DEG or photo-excited electrons. At elevated temperature, a reasonable density of photo-excited holes recombines with background electrons prior to 2DEG recombination which leads to decrease in E_0 intensity. Independent of several possibilities, the temperature dependence of E_0 peak position and integrated PL intensity are consistent with the explanation. Note that the value of ΔE increases by more than 20 meV over the temperature range where it is shown to reduce by 2-4 meV by other researchers.[45, 135, 192] Here, a distinct variation of ΔE with temperature is found which became possible due to an unambiguous identification of 2DEG PL features contrary to other researchers where interference oscillations were labelled as the signature of 2DEG sub-levels. Similar to E_0 feature, E_1 feature also shows a temperature dependent shrinkage and disappears at 30 K. However, the feature is not clearly distinguishable in Fig. 4.1 (a) due to the presence of GaN exciton features. To identify E_1 feature, PL measurements are performed at low excitation

intensity and the spectra are shown in Fig. 4.12 (a). Under low excitation condition, it becomes possible to distinguish E_1 from D^0X (2e) feature which is visible even beyond 30 K as shown by a vertical dotted line in Fig. 4.12 (a).

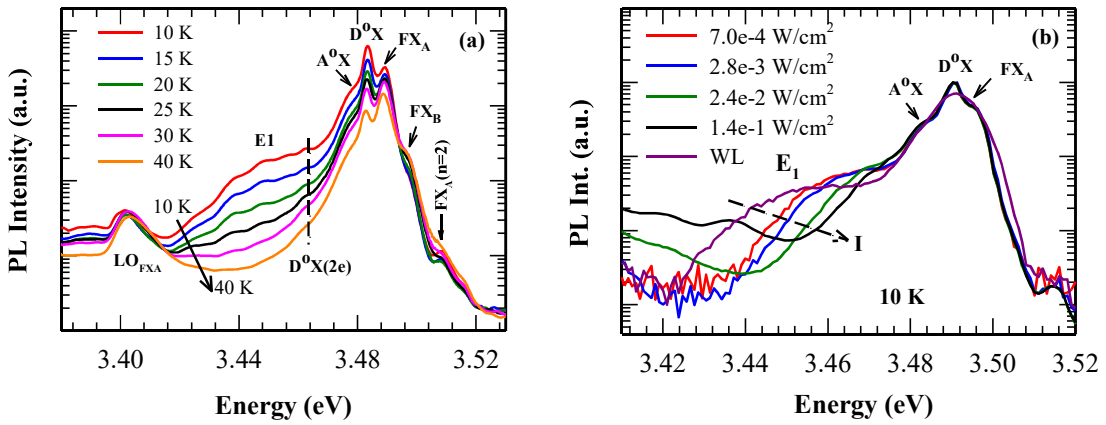

Figure 4.12 (a) Temperature dependent PL spectra of Sample-A recorded at very low excitation intensity for observing the behavior of E_1 feature. (b) Excitation intensity dependent normalized PL spectra of the sample at 10 K where WL stands for the white light excitation sources tuned at 325 nm. The symbols D^0X, FX_A, FX_B A^0X, $FX_A(n=2)$ and $D^0X(2e)$ stand for the donor bound exciton, free A-exciton, free B-exciton, acceptor bound exciton, excited state of free A-exciton and two electron replica of D^0X transitions of GaN respectively. The phonon replica of FX_A is labelled as LO_{FXA}.

4.5.2 Excitation Intensity Dependence of 2DEG PL Feature

Further confirmatory evidence for the identification of 2DEG PL features can be obtained by studying the effect of excitation intensity on E_0 and E_1 features. A strong excitation intensity dependent blueshift of >100 meV for E_0 is observed at 10 K as shown in Fig. 4.1 (b). The excited state feature (E_1) also shows an excitation intensity dependent blueshift of about 5 meV which is shown in Fig. 4.12 (b) in normalized scale for clarity. The excitation intensity dependent peak position of E_0 and E_1 are shown in the lower and

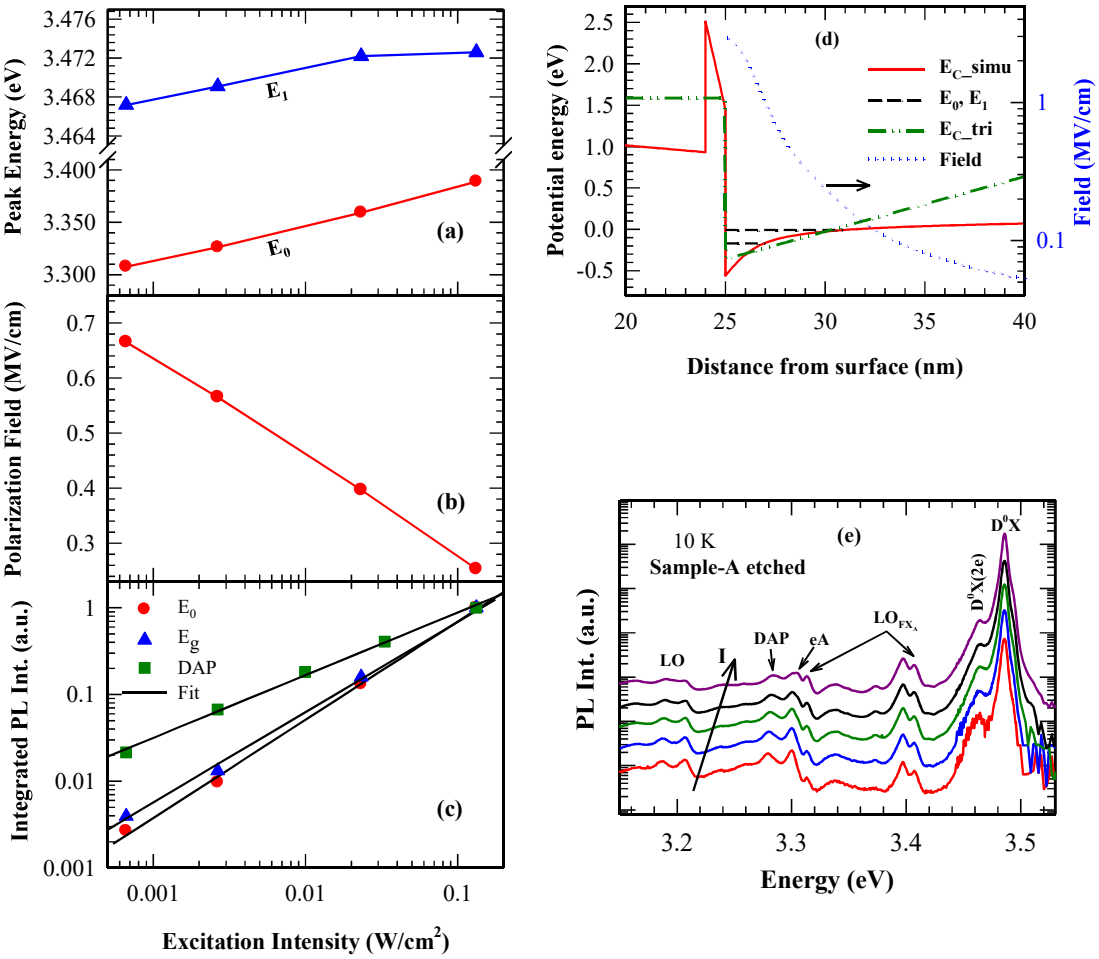

Figure 4.13 (a) Excitation intensity dependence of (a) the ground (E_0) and excited (E_1) state energy levels of 2DEG, (b) the screened polarization induced electric field, and (c) the normalized integrated PL intensity of E_0, band edge PL (E_g) for the as-grown Sample-A and DAP features for the top barrier layer etched Sample-A. (d) The conduction band profile, 2DEG eigenstates, and electric field of Sample-A, and (e) Excitation intensity dependent PL spectra of the etched Sample-A. The symbols D^0X, D^0X (2e), eA, and DAP corresponds to donor bound exciton, two electron replica of donor bound exciton, electron acceptor pair and donor-acceptor pair respectively. The phonon replicas are labelled as LO. 'I' corresponds to excitation intensity.

upper panel of Fig. 4.13 (a). Note that the reported values of excitation intensity governed blueshift of 2DEG feature are ≤ 5 meV.[45, 134, 137] Only Nam *et al.*[136] have reported a blue shift of ~50 meV. In our measurements, a large blueshift of the ground state feature is

observed because of 1) appropriate identification of 2DEG PL features, contrary to older reports,[134, 135] and 2) the effective screening of electric field by photo-generated excess carriers.[136] One can estimate the magnitude of electric field from these measurements by following the procedure of Nam. *et al*. [136]. The outcome of such an exercise is shown in Fig. 4.13 (b). The magnitude of electric field is estimated to be 0.67 MV/cm at an excitation intensity of $6x10^{-4}$ W/cm^2 that systematically reduces with rise in excitation intensity as plotted in Fig. 4.13 (b). We have even performed PL measurements at extremely low excitation intensity by using a Xenon lamp and monochromator assembly tuned at 325nm. Such a plot is also shown in Fig. 4.1 (b). In this case, the value of blueshift of E_0 peak increases to ~150 meV. The magnitude of polarization field estimated from the lamp source based PL measurement turns out to be 1.01 MV/cm. The electric field along the depth of the sample is estimated from the slope of the conduction band which is obtained by self-consistent solution of Schrödinger and Poisson equation for Sample-A. It is plotted as a function of sample depth in Fig. 4.13 (d). The confined energy levels below the Fermi level and the conduction band profile is also shown in the same plot. A maximum electric field of ~3 MV/cm is obtained at the AlN/GaN heterointerface which decreases along the depth of GaN. The values of the electric field at the depth where a crossover between E_0 (E_1) and conduction band occurs is estimated to be 1 MV/cm (0.16 MV/cm) respectively. This can explain the different degree of blueshift for E_0 and E_1. As the polarization field is weak at large spatial depth, the photo-excited carrier induced screening is also less at large depth. Thus the E_1 feature blueshifts with a slower rate than E_0. The energy difference between ground and excited state of 2DEG is estimated to be 0.162 eV from simulation. Similar energy difference of 0.158 meV is obtained experimentally at $6x10^{-4}$ W/cm^2 excitation intensity. The polarization

field is estimated to be 0.67 MV/cm at the same excitation intensity by considering triangular potential well approximation. The triangular potential well is also shown in Fig. 4.13 (d). The estimated field corresponds to an average field to that obtained from the simulation (0.16 MV/cm to 1 MV/cm). It is obvious that the estimated values of polarization induce electric field for AlGaN/AlN/GaN HEMT structures in our measurements are far more realistic when compared with the values reported by other researchers.[136] Excitation intensity dependent PL measurements also support our hypothesis that the E_0 and E_1 feature can't be related to defect levels. Integrated PL intensity of band edge feature and ground state 2DEG feature are plotted as a function of excitation power as shown in Fig. 4.13 (c). We find that the integrated PL intensity of both the features increase linearly (on log-log scale) with excitation intensity with slope more than one showing no signature of saturation. Similar measurements are also performed on etched sample as shown in Fig. 4.13 (e). We find negligible spectral shift in eA and D^0X(2e) transition. The DAP feature is broadened and blueshifts by ~5 meV at large excitation intensity. The integrated PL intensity of DAP is plotted as a function of excitation intensity in figure 4.13 (c) which shows a sub-linear variation (on log-log scale) with a slope of 0.72 ± 0.02 showing saturation.[198] It therefore distinguishes the 2DEG related PL features from defect related transitions.

4.5.3 Dominance of Interference Oscillations

The presence of strong interference oscillations in the identification of 2DEG features needs to be further discussed. The contrast in the interference pattern depends on the reflectivity and quality of the surface/interface. In addition, there is a significant

absorption in the sub-bandgap region due to resonant excitation in traps which also affects interference contrast spectrally. In order to understand this, we did systematic reflectivity measurements under normal incidence conditions and the results are shown in Fig. 4.14 (a). In fact, the magnitude of interference oscillations increases at lower energy. This is expected since the absorption of incident beam increases when one approaches the bandgap from the low energy side. However, an opposite behaviour is observed in the PL spectrum where interference oscillations are more pronounced around the 2DEG feature when compared with the blue luminescence (BL) band as shown in figure 4.14 (a). The magnitude of interference oscillation at different spectral position is estimated by dividing the PL spectra with a Gaussian envelop function and is plotted in Fig. 4.14 (b). The measured value of contrast in the interference oscillations at E_0 (BL) features is 0.1 (0.05) respectively. This is unexpected since the interference oscillations in the PL spectrum must be more prominent for the BL band compared to the E_0 feature if one follows the trends depicted in the reflectivity spectrum where the contrast is

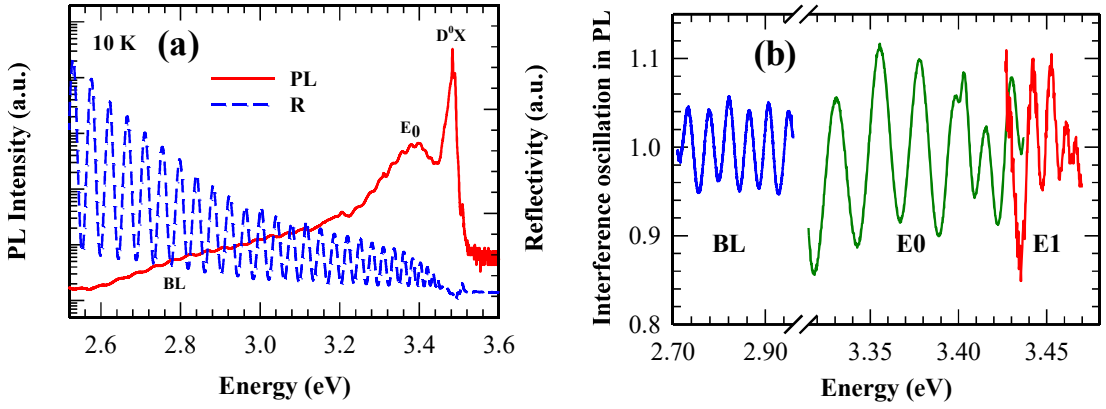

Figure 4.14 (a) 10 K PL and reflectivity spectra of Sample-A recorded under normal incidence condition where D^0X, E_0, E_1, and BL stand for the donor bound exciton, 2DEG ground state, 2DEG excited state and blue luminescence PL features respectively; (b) shows the interference oscillations at different spectral position which is obtained from PL spectra.

estimated to be 0.27 and 0.49 at E_0 and BL spectral location respectively. One possible explanation could be given by considering the spatial location of the 2DEG feature. Note that the period of oscillation is governed by the length of the cavity i.e. the thickness of the GaN channel layer, whereas the contrast of interference oscillations is primarily decided by the interfacial quality and the absorption of concerned radiation by the GaN channel layer. Simple numerical simulations of the interference pattern for a Fabry-Perot cavity are carried out for understanding this behaviour as given in **Appendix C** where one numerically calculates the interference pattern for the two different situations, (1) distributed generation of luminescence signal along the thickness of the GaN channel layer which is usually true in the case of defect luminescence, and (2) localized generation of luminescence signal at one particular facet of the Fabry-Perot cavity which might be the case of the 2DEG PL signal. We find that the contrast of the interference signal is high when the PL signal is assumed to be generated at the AlN/GaN heterointerface. Hence, a poor contrast of interference oscillations in the BL band compared to that of the 2DEG PL feature illustrates that unlike the E_0 feature, BL band is distributed over the GaN channel layer. The presence of strong oscillations around the E_0 peak indicates that the particular feature is originated at the AlN/GaN heterointerface where the formation of 2DEG is expected.

Hence, it is confirmed that one need not to etch HEMT samples for the identification of 2DEG features in PL spectra of AlGaN/AlN/GaN heterostructures. Peculiar temperature and excitation intensity dependencies along with the presence of fine oscillations provide sufficiently strong evidence for an unambiguous identification of 2DEG related features in PL spectra.

4.6 Radiative Recombination Mechanism of 2DEG with Photo-excited Holes

A contactless method for an unambiguous identification of 2DEG features in the photoluminescence (PL) spectrum of AlGaN/AlN/GaN heterostructures is presented so far in this chapter. The particular PL feature originates due to the spatially indirect recombination of 2 dimensional (2D) electrons with photo-excited holes in the valence band.[192] Though several reports aimed towards the identification of 2DEG by observing excitation intensity dependent blueshift of 2DEG related PL features, a little attention has been paid towards the recombination mechanism of 2DEG with photo-excited holes. A lot of work on the study of recombination mechanisms in AlGaAs/GaAs based HEMT structures is already available in literature. The 2DEG related recombination is considered as 1) band-to-band recombination involving localized holes in the valence band without momentum conservation,[199] 2) band-to-band recombination with free holes in the flat band region of valence band with momentum conservation,[200, 201] and 3) excitonic recombination.[202, 203] A super-linear enhancement of 2DEG PL intensity with excitation intensity is also reported which is correlated with the Fermi edge singularity (FES).[204, 205] However, a fundamental understanding of the recombination mechanisms associated with 2DEG PL features in AlGaN/GaN HEMT structures is still missing. In this section, we study the recombination mechanism of 2DEG with photo-excited holes in AlGaN/AlN/GaN heterostructure by performing excitation intensity dependent PL measurements. It is reported that the PL intensity $I_{PL} \propto I_{in}^{k}$ where I_{in} is the excitation intensity and $k=1$ for excitonic recombination and $k=2$ for band-to-band recombination.[206, 207] A log-log plot between integrated PL intensity of E_0 and excitation

intensity is shown in Fig. 4.13 (c). The measured value of k is found to be 1.04 for E_0 feature which indicates about its excitonic origin. Note that, the k values reported in literature[206, 207] are obtained for intrinsic semiconductors where photo-excited carrier density is larger than intrinsic carrier density. It leads to $I_{PL} \propto n_0 p_0 \propto n_0^2 \propto I_{in}^2$ for band-to-band recombination where n_0 and p_0 are the photo-excited electron and hole density respectively. In case of AlGaN/AlN/GaN heterostructure, the 2DEG density (n_{2DEG}) is much higher than photo-excited electron density for which $I_{PL} \propto (n_{2DEG} + n_0)p_0 \approx n_{2DEG} p_0 \propto I_{in}$. Hence, k=1 is possible for band-to-band recombination of 2DEG with photo-excited holes. However, screening of electric field in the triangular well by photo-excited carriers spread the 2DEG density towards the substrate as shown in a later part of this chapter. At a certain depth from the interface, both the 2DEG density and photo-excited hole density increase at large excitation intensity. According to this, $n_{2DEG} \propto I_{in}^{k1}$ where k_1 is a positive constant which depends on the excitation dependent spreading of 2DEG. In case of band to band recombination of 2DEG with photo-excited holes, $I_{PL} \propto (n_{2DEG} + n_0)p_0 \approx I_{in}^{1+k1}$. Thus, band-to-band recombination of 2DEG electrons with photo-excited holes as an origin of E_0 is excluded. It is also important to mention that the excitons will exist only up to a critical field (F_c) which is given by,[134]

$$F_C = \frac{E_B}{e a_B} \tag{4.1}$$

here E_B and a_B stand for the exciton binding energy and exciton Bohr radius in bulk GaN respectively. The estimated value of critical field to break an exciton turns out to be around 100 kV/cm in GaN which is lower than the polarization field estimated from the

2DEG PL peaks as shown in Fig. 4.13 (b). It therefore contradicts the assignment of E_0 transition as an excitonic feature. However, in simulated band profile, the value of electric field falls rapidly with depth beyond AlN/GaN interface as shown in Fig. 4.13 (d). It is therefore clear that the exciton recombination is possible only in quasi-flat region of valence band where electric field weak to break exciton. In order to get further details, PL measurements are performed over a wide range of excitation intensity as shown in Fig. 4.15 (a). The excitation intensity dependent peak energy, FWHM and integrated PL intensity of E_0 feature are plotted in Fig. 4.15 (c), (d) and (e) respectively. The excitation intensity dependent peak shift and integrated PL intensity of E_0 feature is similar to the previously presented data. We find a decrease in FWHM with increasing excitation intensity which can be explained by considering the screening of electric field since potential fluctuations are expected to be less pronounced at low field. A new sharp feature, labelled as 'X' in Fig. 4.15 (a), appears at 3.436 eV at the high energy side of E_0 feature at large excitation intensity. Normalized PL spectra at few intermediate excitation intensities are also shown in Fig. 4.15 (b) for clarity of feature-X. Further, feature-X is absent in PL spectra of top barrier etched sample which suggests that the particular feature is related to 2DEG states. It is therefore important to identify the origin of feature-X including the associated recombination mechanisms. It displays a very different character as shown in Fig. 4.15 (c), (d) and (e) where the energy, FWHM and integrated intensity are plotted as a function of excitation intensity. Feature-X shows a slower blueshift when compared with E_0. Contrary to E_0, the FWHM of feature-X increases at large excitation intensity. Furthermore, the integrated PL intensity increases super-linearly with excitation intensity having $k = 1.44$. The super-linear rise of can occur due to two possible reasons: i) band-to-band carrier recombination or ii) Fermi edge

singularity (FES). If feature-X is related to band-to-band transition, then a k value of $(1+k_1)$ is expected for feature-X as explained before. Now an important question arises that how 2DEG related PL feature is switching from excitonic to band-to-band transition?

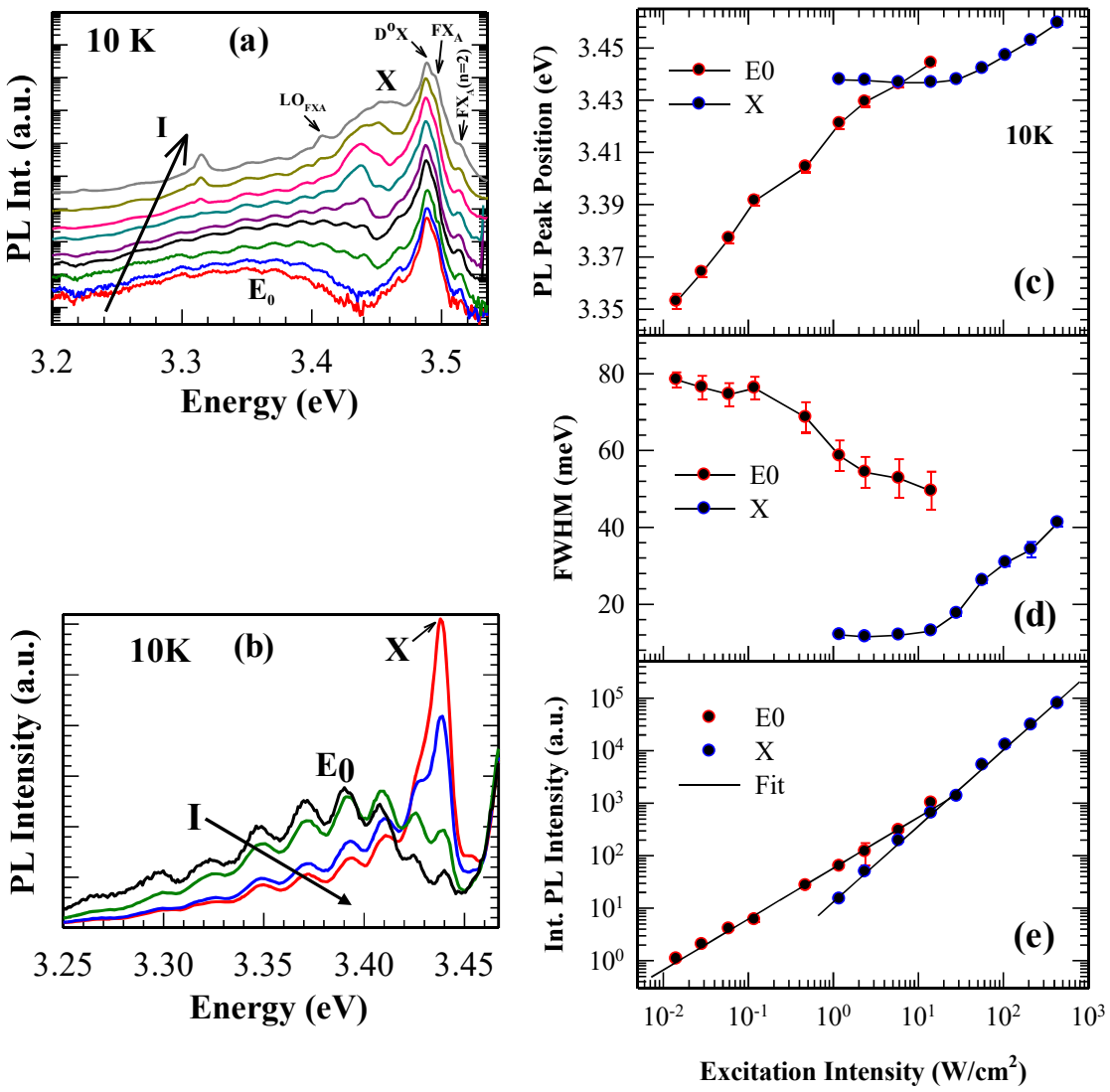

Figure 4.15 (a) 10 K Excitation intensity dependent PL spectra of Sample-A where the normalized PL spectra at some intermediate excitation intensities are shown in (b). 10 K excitation intensity dependence of E_0 feature and feature-X (c) peak energy, (d) FWHM, and (e) Integrated intensity of Sample-A. The symbols D^0X, FX_A, FX_A (n=2), LO_{FXA}, and E_0 stand for donor bound exciton, free exciton-A, excited state of FX_A, optical phonon replica of FX_A, ground state of 2DEG respectively. 'I' stands for excitation intensity.

In order to understand this, Schrödinger equation is numerically solved for triangular potential well. Here, excitation intensity is incorporated as a parameter in terms of the values of electric field as shown in Fig. 4.13 (b). Next, the 2D-carrier distribution along the depth is estimated by using the procedure given by Chu *et al.*[139] as given below:

$$n_{2D}(z) = \sum_i \frac{m^* kT}{\pi\hbar^2} |\psi_i(z)|^2 \ln\left[1 + \exp\left(\frac{E_f - E_i}{kT}\right)\right] \tag{4.2}$$

where m^* is the effective mass of electron, Ψ_i are the normalized 2DEG wavefunctions, E_f is the Fermi level, E_i is the eigenstates of 2DEG. Note that the total 2DEG density is given by,

$$n_{2D} = \int n_{2D}(z) dz \tag{4.3}$$

In presence of optical excitation, the total 2DEG density corresponds to the sum of equilibrium 2DEG density (n_{2d}) and the photo-generated excess carrier density (n_{Exci}) at the heterointerface,

$$n_{2D} = n_{2d} + n_{Exci} \tag{4.4}$$

where n_{2d} is estimated as $1.9 \times 10^{13}/cm^2$ from Hall measurements and n_{Exci} is estimated from the excitation intensity considering a lifetime[136] of 1 ns of 2DEG PL recombination. Now, Fermi level is varied numerically in Eq. 4.2 such that the measured and simulated values of n_{2D} match. The potential profile, eigenstates, Fermi level and the transitions occurring at the triangular potential well for the two values of electric field are plotted in Fig. 4.16 (a). The triangular potential well is flattened due to the screening of electric field. 2DEG energy levels shift towards the minima of potential well whereas potential minimum shifts up due to the flattening of potential profile. The spatial distribution of

2DEG density is numerically calculated by using Eq. 4.3 at different excitation intensity as shown in Fig. 4.16 (b). At low excitation intensity, 2DEG density peaks at a distance of ~1 nm from AlN/GaN interface. The carriers start to leak out from the triangular well at high excitation intensity as obvious from Fig. 4.16 (b). It is reported in literature that

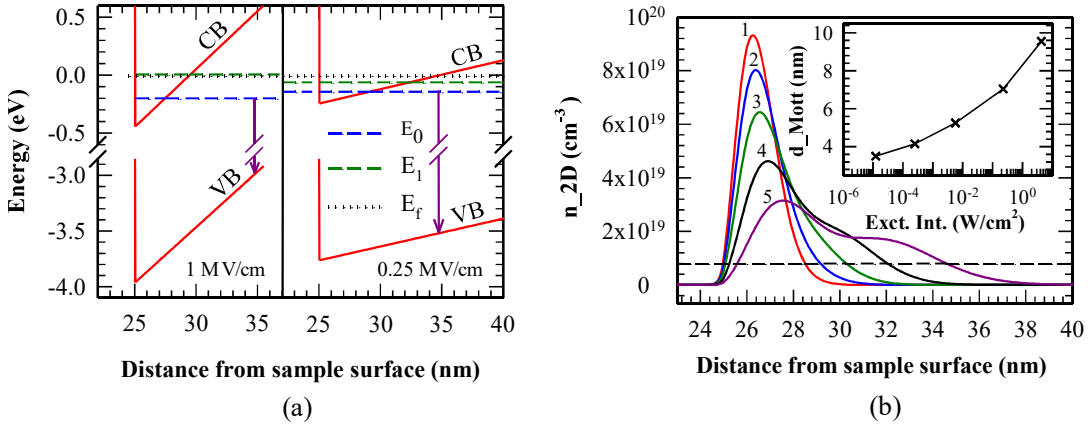

Figure 4.16 (a) Potential profile, eigenstates and the transitions occurring at the triangular potential well for two values of electric field are plotted as a function of depth at a) 1 MV/cm and b) 0.25 MV/cm electric field respectively. The ground state (E_0) and 1st excited state (E_1) energy values are shown along with the Fermi level (E_f). 2DEG ground state PL transition is also marked by a downward arrow. (b) Distribution of 2D-electrons with the depth for AlGaN/AlN/GaN HEMT structure at a few excitation power where curves 1,2,3,4 and 5 stand for 0.012, 0.25, 5.7, 227 and 4281 mW/cm^2 exitation intensity respectively. The horizontal dash line mark the carrier density of 8x10^{18}cm^{-3} which corresponds to critical Mott carrier density. Inset shows the variation of critical Mott thickness as a function of excitation power.

when the carrier density exceeds Mott critical carrier density, Coulomb attraction between electron and hole is screened by the excess carriers and the recombination mechanism shifts from excitonic to free carrier recombination.[208, 209] A Mott transition has been theoretically predicted for 2-dimensional layer at low temperatures and at high

carrier density.[210] To check whether such an effect is occurring in our case, Mott critical carrier density is estimated by using the following equation,[209]

$$n_{Mott} \approx \frac{1}{\frac{4}{3}\pi a_B^3} \tag{4.5}$$

which turns out to be around $8x10^{18}/cm^3$ for bulk GaN as marked by a horizontal dash line in Fig. 4.16 (b). Here, critical Mott thickness (d_{Mott}) is assigned as the distance from the interface below which $n_{2D}(z) \geq n_{Mott}$. One would expect to see a free carrier recombination below d_{Mott} while excitonic recombination is inevitable at larger distances. Note that the holes are expected to drift to the quasi-flat region leading to the dominance of excitonic recombination as displayed by E_0 feature. It is found that d_{Mott} increases with excitation intensity as shown in the inset of Fig. 4.16 (b). At large excitation intensity, d_{Mott} becomes substantially large and approaches the quasi-flat band region where photo-excited holes are already present. Under such circumstances, free carrier recombination of 2D-electrons with holes is possible. In view of the aforementioned discussion, feature-X can be considered as the free carrier recombination associated with 2DEG ground state at high excitation intensity. Feature-X is originating from a small region near d_{Mott} which supports a low value of FWHM and negligible blueshift when compared with E_0 feature. However, at substantially large excitation intensity even feature-X involves recombination of carriers over a large region since d_{Mott} lies in the quasi-flat band region. It is clear that the recombination at large depth shall give rise to PL signal a low energy. This leads to the rise of FWHM and redshift with excitation intensity. However, 2DEG PL features are expected to show a blueshift due to carrier screening. The two competing mechanisms therefore lead to the observation of relatively small blueshift of feature-X

when compared with E_0 feature. On the other hand, feature E_0 including its low energy tail displays excitonic character at all excitation powers in our measurements.

There is another possibility that the Feature-X might be related to FES. FES transition is already reported in AlGaAs/GaAs HEMT structures which is explained by considering the scattering of electron between Fermi edge and 1st excited state of 2DEG.[204, 205] The criterion for observing a FES transition is that the Fermi edge should be close (<5 meV) to 1st excited state of 2DEG. But the measured energy difference between Feature-X and 1st excited state of 2DEG in our case is ~ 40 meV. Further, it is merged at the high energy tail of E_0 feature at excitation intensity ~ 5 W/cm^2 which also confirms that the feature-X is not associated with FES.

4.7 Conclusion

In summary, Systematic PL and reflectivity measurements are performed on AlGaN/AlN/GaN based HEMT structures. Two broad 2DEG PL feature superimposed with several fine oscillations is also observed. The origin of fine oscillations is probed by performing angle dependent PL and reflectivity measurements. It is confirmed that the fine oscillations, which were assigned as the signature of 2DEG sub-levels by other researchers, are actually interference oscillations. The results of other researchers, who have earlier assigned the fine oscillations as the 2DEG sublevels, are also understood in light of the interference phenomenon. The disappearance of broad features in PL spectra of top AlGaN barrier layer etched sample confirms that they are related to 2DEG. The peculiar temperature and excitation intensity dependence of 2DEG PL features are

explained in terms of thermal shrinkage of GaN bandgap and screening effect by thermal and photo-excited carriers. Specific temperature and intensity dependence of 2DEG features make them highly distinct and these can be easily identified in the presence of band edge excitonic and defect related PL features even without etching the sample. The recombination mechanisms of 2D electrons with photo-excited holes in AlGaN/AlN/GaN HEMT structures are also explored from excitation intensity dependence of 2DEG PL. At low excitation intensity, 2DEG PL features displays an excitonic behaviour. At substantially large excitation intensity, a new feature appears on the high energy tail of the excitonic feature. This feature shows very different characteristics when compared with the excitonic feature. It is assigned as the free carrier recombination of 2D electrons with holes in the quasi-flat region of AlGaN/AlN/GaN HEMT structure. Such a recombination mechanism is found to dominate at high excitation intensity once the 2DEG density exceeds critical Mott density at a certain depth from AlN/GaN interface. The present work shall be helpful in understanding the behaviour of 2DEG states under the influence of external electric field.

Chapter 5

Impact of Mg-doped GaN Buffer on the Optoelectronic Properties of AlGaN/GaN High Electron Mobility Transistors

5.1 Introduction

In spite of a substantial improvement in the performance of nitride-based devices, AlGaN/GaN HEMT design still suffers from several limitations. For example, entrapment of 2-dimensional electron gas (2DEG) on the electrically active defects at surface, AlGaN/GaN interface and in GaN channel layer of AlGaN/GaN HEMT devices lead to the critical issues related to current collapse and DC-to-RF dispersion.[22, 24, 48, 52-56, 211] Though 2D-electrons are strongly confined by AlGaN barrier at one side of the asymmetric triangular potential well, these can easily spread towards the substrate. Such a spillover of carriers is mainly governed by the magnitude of built-in electric field and device temperature. Spillover of carriers from the triangular potential well followed by the trapping at defects in GaN buffer layer leads to current collapse. Additionally, the characteristic time of trapping and de-trapping by defects limit the high frequency performance of device. 2DEG spillover to the buffer layer can be reduced by increasing

the barrier height by including a double heterostructure design[37] while the trapping effect can be supressed by passivating the surface states[25, 26] and by reducing the defect density in GaN buffer layer.[32, 33, 35, 212, 213] In addition to current collapse, unintentional impurities such as silicon and oxygen act as a shallow donors and contribute to substantial background electron density in GaN buffer layer and at the regrowth interface. A parallel conducting channel is usually formed at layer/template interface due to the presence of a large density of impurity states. It results in a poor pinch off characteristics of HEMT devices.[36] In order to improve the performance of HEMT devices, it is therefore essential to reduce defect density in GaN buffer layer and to restrict the background electron concentration to a minimal level. One procedure to minimize the electron density is to compensate the residual donors by shallow and deep acceptor impurities such as carbon (C), iron (Fe) and magnesium (Mg).[35, 36, 60, 179] These acceptor dopants not only reduce background electron density but also enhances the confinement of 2DEG near AlGaN/GaN heterointerface by increasing the barrier height towards the substrate.[34] However, these dopants create deep levels which can capture 2DEG during operating condition of HEMT and can give rise to current collapse. One can suppress the trapping of carriers by doping the initial part of GaN buffer layer with appropriate acceptor atoms and then by leaving the rest of buffer layer unintentionally doped. Acceptor atoms lying in proximity of layer/template interface effectively compensates unintentional donor impurities which helps in improving the pinch off condition. On the other hand, 2DEG density is merely affected by the acceptor atoms since these are located at a reasonable distance from the triangular potential well. In previous chapters, characterization of impurity/defect levels in AlGaN/GaN HEMT structures is discussed where detailed characteristics and origin of the major luminescence bands including blue and yellow

luminescence (YL) bands is reported. A correlation among intensity of YL band, threshold voltage and on-resistance of AlGaN/GaN HEMT structure is already reported by Huber *et al*.[93] It is reported that the dynamic performance of AlGaN/GaN based device is significantly affected by YL related defect states. A comparative analysis of the main defect related optical signatures in HEMT samples with different growth design can help in optimization of HEMT quality. In this chapter, impact of Mg doping during initial part of GaN buffer layer in AlGaN/AlN/GaN heterostructure is investigated by performing PL, PLE and SPS measurements.

5.2 Sample Details

AlGaN/AlN/GaN HEMT samples (Sample-A, B and C) used in the study are grown by using Ammonia molecular beam epitaxy (MBE) system on c-plane Fe-doped GaN/Sapphire templates. Sample-A was used to characterize the defects and presence of 2DEG features in PL spectra in **chapter 3** and **Chapter 4** respectively. The only difference among the samples is related to magnesium doping density which is incorporated during the initial part of GaN buffer layer on Fe-GaN template. The magnesium concentration in the AlGaN/GaN heterostructures is characterized by secondary ion mass spectrometry (SIMS), using O2+ as the primary ion source, and the amount of ejected charged species is mass-resolved detected. Quantification of magnesium in a GaN matrix is achieved by calibrating to a heavily Mg doped p-GaN standard. The SIMS spectra for these samples are shown in Fig. 5.1. The downward arrow is marked at the layer/template interface where SIMS peak related to silicon is observed. The magnesium concentration in Sample-A is below detection limit of SIMS

while Sample-B and C has a magnesium concentration of ~$8x10^{18}$ cm^{-3} and $2x10^{19}$ cm^{-3} in the Mg-doped GaN interlayer respectively. The Al content (x=0.33) of the top $Al_xGa_{1-x}N$ barrier layer is estimated by performing ω-2θ HRXRD scan where the diffraction pattern for Sample-A is shown in inset of Fig. 5.1. The Al content of x=0.28 and x=0.33 is obtained for Sample-B and C respectively. The FWHM of GaN XRD peak is found to be 183 sec for Sample-C as compared to 145 sec for Sample-A and B which is an indication of deterioration of crystalline quality with heavy magnesium doping.

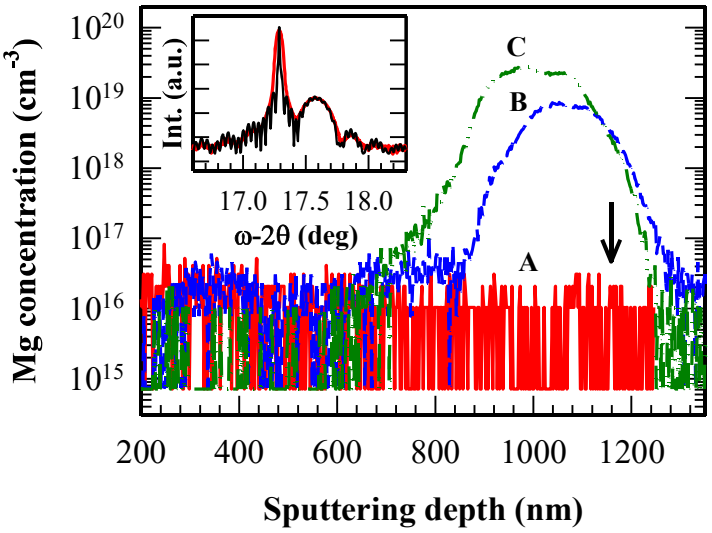

Figure 5.1 SIMS profile of Mg dopant concentration in AlGaN/GaN heterostructures where arrows mark the location of layer/template interface. Inset shows the (0002) HRXRD pattern of sample-A. The fitted data is also shown in the inset.

5.3 Effect of Mg Doping on Compensation of Defects

Figure 5.2 shows the room temperature PLE spectra of the samples where the detection wavelength is set to YL peak of the PL spectra as shown in inset for Sample-A. A free exciton (FX_A) feature and a broad YL band is observed at 3.4 eV and 2.2 eV

respectively in PL spectra. The YL band is reported to be related to the conduction band/ shallow donor to C_N or C_N-O_N deep trap state transition. PLE spectra of both the samples shows that YL feature originates due to band-to-band excitation above 3.43 eV and also due to valence band-to-shallow donor excitation below 3.43 eV which is marked by "h-D".[178] The above bandgap PLE is absorbed with in the penetration depth (~ 100 nm from AlN/GaN interface) and therefore provides YL related defect information in GaN channel layer close to 2DEG. The sub-bandgap PLE is transparent to the heterostructure and therefore can provide YL information form the entire depth. In **chapter 3**, sub-bandgap PLE transition is shown to be dominated from the GaN/Fe-GaN regrowth interface while the donor impurity is correlated to Si. The suppression of h-D PLE feature in case of Sample-B and C indicates the compensation of YL related defects at the regrowth interface. Note that, the intensity of YL band is proportional to $nN_{DS}(1-f_{DS})$, where, n, N_{DS}, and f_{DS} corresponds to background electron density, density of YL related deep state, and occupation probability of deep states respectively. The deep state lies well below the Fermi level. Thus, f_{DS} can be assumed to be same for both the samples. The suppression of PLE intensity indicates that either or both n and N_{DS} are reduced near 2DEG channel region and at the GaN/ template regrowth interface due to magnesium doping. The compensation of unintentional donors is beneficial for low leakage while the reduction of YL related deep trap state near 2DEG accumulation region is beneficial for low current collapse and DC-to-RF dispersion. However, a BL feature appears at ~ 2.9 eV in case of Sample-B and C at room temperature PL spectra. It originates due to conduction band to Mg deep acceptor transition where a gradient Mg doping along the growth direction is inevitable due to the memory effect.[214] Note that

Mg related acceptor states can also trap 2DEG. Thus, an optimization of Mg doping is essential and this needs to be explored.

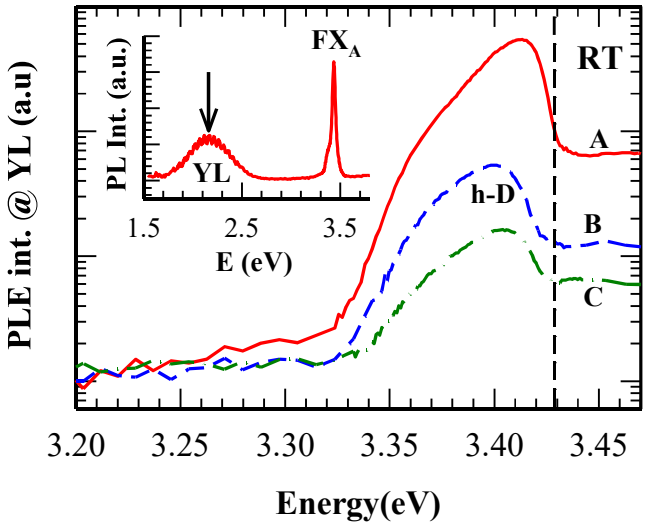

Figure 5.2 Room temperature PLE spectra of AlGaN/AlN/GaN heterostructures where the detection wavelength is set to YL peak of PL spectra. Inset shows the PL spectra of Sample-A which is recorded with 325 nm excitation from a Xe lamp and monochromator assembly. The symbols FX_A, and YL corresponds to free exciton A and yellow band respectively. Valence band to shallow donor transition is marked by holes-to-donor (h-D) while the vertical dashed line is a guide to band edge of GaN.

In order to get further details, systematic SPS measurements are performed on these samples. Room temperature SPS magnitude spectra of these samples are shown in Fig. 5.3 (a). SPS magnitude spectra of Sample-A at room temperature and 10 K is already presented in **Chapter 3**. A low magnitude of above bandgap SPV at room temperature is explained by considering the presence of large background carrier density and traps in the accumulation region. Due to accumulation type band bending, the photo excited minority carriers (hole) move towards the substrate. The presence of strong background electron increases the recombination probability of photo-excited holes. It leads to a loss of spatially separated electron-hole density and therefore reduction in SPS magnitude.

Similarly, capture of photo-excited holes by defects states in the channel layer before the separation also leads to suppression of SPV. In case of Sample-B and C, a strong enhancement of SPV magnitude is observed in the above bandgap of GaN which indicates about lowering of the background electron density (n) as well as trapping of holes. Such an explanation is consistent with the decrease in the intensity of YL band with Mg doping of a part of GaN layer. Note that, h-D feature is present in both the samples. In fact, SPS amplitude corresponding to this particular feature is high in case of Sample-B. However, no conclusion can be made on the relative density of shallow donors at the regrowth interface because SPS amplitude depends on both the density of shallow donor state and band bending at layer/template interface. To evaluate the effect of Mg

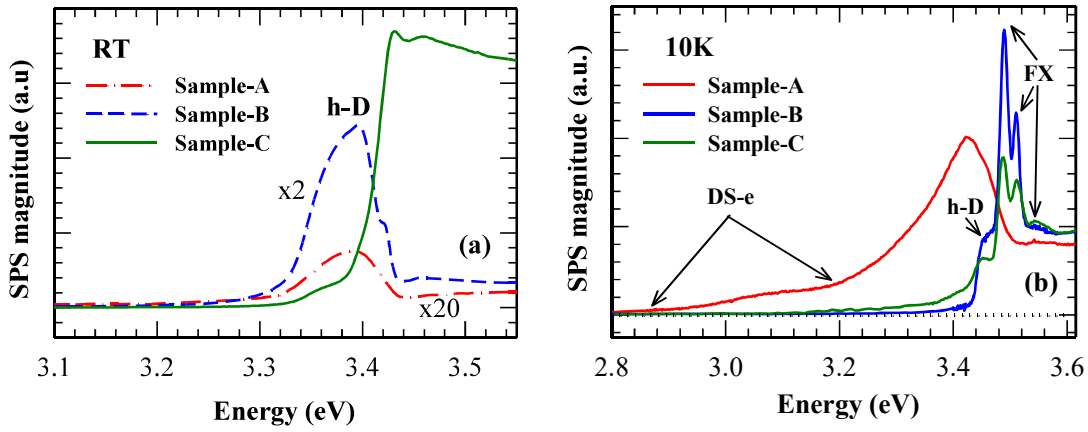

Figure 5.3 (a) Room temperature and (b) 10 K SPS spectra of AlGaN/AlN/GaN heterostructures which are recorded at 28 Hz modulation frequency. The symbols FX, h-D, and DS-e corresponds to free exciton transitions, valence band to shallow donor transition, and resonant transition in YL related deep defect complex respectively. Dotted line shows the background signal in SPS measurements.

doping on deep defects, SPS measurements are performed at 10 K and the spectra are shown in Fig. 5.3 (b). In case of Sample-A, two broad features (DS-e) with onset at 2.8 eV and 3.2 eV are obtained. These features are correlated to the resonant excitation in

YL related defect complex in **Chapter 3**. Further, the particular features are also found to be located near 2DEG accumulation region. At 10 K, SPV component from the accumulation region dominates due to freeze out of background carriers. SPS magnitude due to DS-e transition depends mainly on the density of deep defect states. Disappearance of these features in case of Sample-B therefore indicates the reduction of density of YL related deep defects near 2DEG channel. YL defect density might be reduced due to a rise in formation energy of YL related defect complex which is primarily governed by the movement of Fermi level towards the valence band edge. Clear absorption edges related to free exciton A, B and C are also observed in SPS spectra of Sample-B and C. Valence band to shallow donor transition (h-D) is also observed at ~3.45 eV which is blue shifted due to the thermal increase of the bandgap of GaN. PLE and SPS measurements therefore indicate that both the background carrier density and YL related deep defect reduces with incorporation of magnesium at the regrowth interface. Thus, magnesium doping of part of GaN buffer layer which is expected to be highly beneficial for HEMT performance.

5.4 Impact of Mg Doping on 2DEG Confinement

Finally, 10 K PL measurements are performed on these samples with an overall aim of observing some impact of Mg doping on 2DEG confinement. Fig. 5.4 (a) shows the 10 K PL spectra which are recorded under identical conditions. A weak donor bound exciton (D^0X) feature and strong donor acceptor pair (DAP) feature along with its LO phonon replicas in case of Sample-B indicates the compensation of shallow donors and presence of Mg acceptor near AlN/GaN interface. A broad feature (E_0) related to spatially

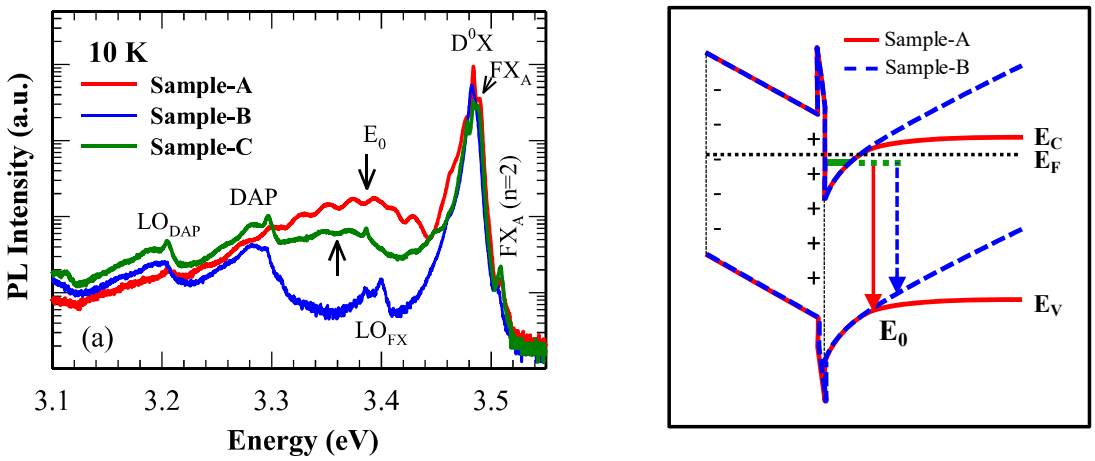

Figure 5.4 (a) 10 K PL spectra of AlGaN/AlN/GaN heterostructures recorded with a moderate optical excitation intensity and (b) schematic band diagram of the two heterostructures and corresponding transition energies. FX_A, D^0X, DAP and LO_{DAP} corresponds to free exciton-A, neutral donor bound exciton, donor-acceptor pair and longitudinal optical phonon replica of DAP respectively. E_0 corresponds to 2DEG-photo-excited hole recombination. E_C, E_V and E_F are conduction band, valence band and Fermi level respectively.

indirect recombination of 2-dimensional electron gas with photo-excited holes is observed for Sample-A and C at an energy lower than the free exciton edge of GaN while it is not visible in case of Sample-B. The E_0 feature is convoluted with several fine interference oscillations, however, the interference contrast is weak in case of Sample-C due to poor interface quality. A low intensity and a large redshift of E_0 feature with respect to the GaN bandgap is a clear indication of the spatially indirect recombination of 2DEG with photo-excited holes in presence of a strong built-in electric field at the heterointerface. Stronger is the electric field at the heterointerface, larger is the redshift and lower is the intensity of 2DEG PL feature. The strong electric field leads to a larger barrier height for the 2DEG towards the substrate and restricts 2DEG spillover towards the substrate as shown in Fig. 5.4 (b). A weaker intensity and larger redshift of E_0 feature

in case of Sample-C when compared to Sample-A as shown in Fig. 5.4 (a) confirms a better confinement of 2DEG at the heterointerface due to partial Mg doping. Magnesium doping moves the conduction band away from the Fermi level which provides large barrier height for 2DEG electrons.[34] The electric field further increases the spatial separation of 2DEG and photo-excited holes. Both the effects lead to low intensity and a large redshift of 2DEG PL feature. The absence of E0 feature in case of Sample-B indicates that the oscillator strength for 2DEG recombination is weakest for Sample-B for which E_0 is merged below the DAP features. Thus, a weak 2DEG PL with large red shift indicates towards better quality HEMT structures.

5.5 Conclusion

The effect of Mg doping during initial growth of GaN buffer layer is investigated by spectroscopic measurements. The Mg doping is found to reduce both background carrier density and YL related deep defects. It further enhances the confinement of 2DEG at the AlN/GaN interface. The results suggest that semi-insulating GaN buffer layer with compensated Mg doping can be a good candidate for AlGaN/AlN/GaN HEMT.

Chapter 6

Summary and Future Scope

6.1 Summary of the Thesis and Conclusion

During the course of this thesis, novel spectroscopic techniques are used to investigate fundamental electronic transitions in nitride epitaxial layers and AlGaN/AlN/GaN HEMT structures in a truly non-destructive manner. First, a new configuration of SPS technique is proposed where an additional cw pump laser beam is used in a conventional chopped light geometry setup under pump-probe scheme. Through a judicious choice of sub-bandgap laser i.e. an apparent pump, the technique is proven to be capable of measuring the bandgap of semiconductor epitaxial layers very accurately even under the strong influence of localized states. On the other hand, pump-probe SPS measurements with an above bandgap pump laser are found to be very useful in the identification of spatial location of defects. Identification of the spatial location of sub-bandgap SPS features is critically important for establishing a firm correlation among SPS features and respective defect levels. In conventional SPS technique, one measures an algebraic sum of all the SPS components that might be generated at different spatial locations inside the sample. Sign of SPS signal therefore depends on the type of band bending which might be present at the generation site of signal. If the spatial location of sub-bandgap SPS feature is not known, then no correlation of SPS signal can

be made with a specific defect level. However, in pump-probe SPS technique, one can selectively pick up SPS signal from a particular depth by choosing an appropriate laser beam. Under such a scenario, it is possible to make an unambiguous identification of defect levels. During the course of this thesis, pump-probe SPS technique is proven to be extremely useful in pinpointing the spatial location of defects inside the sample. Availability of this information is found to play a critical role in identification of defects in p-GaN epitaxial layer and AlGaN/AlN/GaN heterostructures.

Next, the fundamental origin of commonly observed defect related luminescence bands in GaN epitaxial layers and heterostructures is investigated by performing complementary spectroscopic measurements. The most debated defect features in GaN epitaxial layers are the blue luminescence (BL) band in heavily Mg doped p-GaN and yellow luminescence (YL) band in all types of GaN epitaxial layers. Further, an exact correlation of these PL bands to particular defect levels and their spatial location within the sample is not established. It is one of key issues which have been addressed in this thesis. BL band appears in heavily Mg doped p-GaN samples where a self-compensation phenomenon is also observed which is understood to limit the p-doping of GaN layers. There are two school of thoughts regarding the origin of BL band in GaN: i) deep donor to shallow acceptor transition, and ii) conduction band to deep acceptor transition. In this thesis, complementary spectroscopic measurements based on PL and SPS techniques are performed on heavily Mg doped p-GaN samples where model-ii is found to be associated with the origin of BL band. The microscopic origin of YL band in GaN epilayers is found to be equally controversial where several models have been proposed during the last three decades. Very recently, carbon related defect complex is considered to be the main source however it is still being debated whether C_N acceptor or C_N-O_N deep donor complex is

responsible for the formation of YL band. Moreover, spatial location of YL band in GaN epilayers is largely unclear where conflicting reports keep appearing in literature. It is noticed that different parts of the sample are claimed to be associated with the origin of YL band and a generalized understanding is yet to be developed. Spatial location of YL band is specifically addressed in this thesis, where systematic spectroscopic measurements are performed under both the conventional and pump-probe geometry on AlGaN/AlN/GaN heterostructures. YL related deep trap states are found to lie approximately 1 eV above the valence band edge and resonant excitation edges of this defect complex occur at 2.8 and 3.2 eV. The peak energy of YL band and resonant excitation edges measured from SPS spectra closely matches with the values of transition energy associated with C_N-O_N deep donor complex reported in literature. Further, it is found that YL related defects are present throughout the sample whereas a specific dominance appears from the epilayer/template interfacial region. It is also learnt that the dominance of YL band from a particular spatial region depends not only on the density of deep trap states but also on their occupation probability. Depending on the experimental technique, one essentially probes different spatial location of the sample where both the density and occupation function of deep trap states are different. Thus a generalized comment on the spatial location of YL related defect states based on a single characterization technique might be erroneous.

Once the spectroscopic features related to defect states are understood, attention is paid to identify the genuine features of AlGaN/GaN heterostructures. As a special case, an unambiguous identification of 2DEG features in AlGaN/AlN/GaN HEMT structures is obtained by a fast and contactless method. A prior knowledge of true signatures of 2DEG in HEMT structures is technologically important since it can be of immense help

to the device manufactures. Appearance of several fine features in the PL spectra of AlGaN/GaN heterostructures has been correlated with the sub-levels of 2DEG by other researchers. Such a conclusion is drawn on the basis of some peculiar temperature and excitation intensity dependencies. However, it is clearly shown in this thesis that the fine features in PL spectra of AlGaN/AlN/GaN HEMT structure are not at all related to the sub-levels of 2DEG rather these are governed by interference phenomenon. Temperature dependence of the interference oscillations is explained by considering the wavelength and temperature dependence of the refractive index of GaN. On the other hand, a small blue shift of fine oscillations is found be driven mainly by a strong excitation intensity dependence of broad 2DEG features on which interference features are actually superimposed. Further, the dominance of interference oscillations on 2DEG PL features is explained by considering their spatially localized origin within the triangular potential well. A clear disappearance of the two broad features in case of top barrier etched sample confirms that these are essentially related to 2DEG. Furthermore, a numerical self-consistent solution of Schrödinger and Poisson equations for the AlGaN/AlN/GaN heterostructure also predicts existence of only two sub-levels of 2DEG below Fermi level. The broad features are thereafter considered to be related to radiative recombination of 2-Dimensional electrons with photo-excited holes. The temperature and excitation intensity dependent shift of 2DEG PL features are explained by considering the screening of electric field in the triangular potential well by thermal and photo-excited carriers. The values of electric field estimated from the measured peak energy of 2DEG sublevels matches reasonably well with the values obtained from numerical simulations. The recombination mechanism of 2DEG with photo-excited holes is also explained from excitation intensity dependent PL measurements. It is found that

excitonic recombination occurs at low excitation intensity whereas band-to-band recombination of 2D-electrons with photo-excited holes occurs at high excitation intensity. A switchover from excitonic to band-to-band recombination occurs when net 2DEG and photo-excited electron density exceeds critical Mott density in the quasi-flat band region of GaN channel layer where oscillator strength is estimated to be the maximum.

Finally, the understanding developed for the characterization of nitride epitaxial layers is implemented for a qualitative comparison of AlGaN/AlN/GaN HEMT samples. Two such samples are grown where Mg doping with different concentration is done during the initial growth of GaN buffer layer on Fe-GaN/Sapphire template. Here, an ultimate aim is to minimize the parasitic effects and to suppress the current collapse. In design of HEMT structure, it is essential to grow a highly resistive GaN buffer layer and to minimize the density of deep trap states to address the issue of parasitic effect and current collapse respectively. Mg doping during the initial growth of GaN buffer is found to suppress YL band and also in the minimization of associated deep trap density and background electron density throughout the GaN buffer layer. In addition, it is found that Mg doping suppresses the spillover of 2DEG towards the substrate by increasing the effective barrier height. Thus, Mg doping during the initial growth of GaN buffer can be extremely beneficial for improving the performance of the AlGaN/AlN/GaN HEMT devices.

To conclude, novel spectroscopic techniques are implemented to understand the fundamental origin of defect features in nitride epitaxial layers. A new configuration of SPS technique is proposed which is found to be extremely beneficial in pinpointing the spatial location of spectroscopic features within the layer structure. Complementary

spectroscopic techniques are used to address the puzzling issues related to the origin of BL and YL bands which have been lingering for the last few decades. An anomaly related to the association of fine features in the PL spectra of AlGaN/GaN HEMT structure with 2DEG sublevels is resolved where oscillatory features are found to be governed by the interference phenomenon. An unambiguous identification of 2DEG features is thereafter achieved which helps in a qualitative comparison of HEMT samples. Recombination mechanism of 2DEG with photo-excited holes is also discussed. During the course of this thesis, contactless nature of spectroscopic techniques is proven to be especially important for a truly non-destructive characterization of defects and 2DEG features in AlGaN/GaN HEMT structures.

6.2 Scope for Future work

During the characterization of AlGaN/AlN/GaN HEMT structures, it is found that Mg doping during the initial growth of GaN buffer is found to suppress background electron density and YL related deep trap states. However, this information needs to be complemented by some improvements in the device characteristics. Further, a heavy Mg doping is expected to introduce deep defect complexes which can be detrimental to the device performance. To predict an optimum value of Mg doping is therefore of prime importance. It is also necessary to validate the proposed method of 2DEG characterisation by characterizing a set of HEMT samples which might be grown by varying some layer/growth parameter in a systematic manner. Finally, HEMT devices with optimized Mg doping needs to be fabricated for confirming the validity of design methodology by demonstrating some improvement in the operational characteristics.

APPENDIX

APPENDIX A:

Numerical simulations for the wavelength dependence of refractive index of GaN

In case of the reflectivity spectrum of AlGaN/GaN based HEMT structures, an essential condition for observing an interference peak under normal incidence condition is given by,[189]

$$2n(\lambda)d = m\lambda \tag{A1}$$

where n (λ), d and m stand for the refractive index at wavelength λ, thickness of the sample, and integer multiple of the standing wave where constructive interference occurs. Hence, for observing any two interference maxima, i.e., m^{th} maximum (at λ_1) and $(m+p)^{th}$ maximum (at λ_p) are governed by the following equations:

$$2n_1 d = m\lambda_1 \tag{A2}$$

and

$$2n_p d = (m+p)\lambda_p \tag{A3}$$

By rearranging the two equations, we get

$$n_p = p\frac{\lambda_p}{2d} + n_1\frac{\lambda_p}{\lambda_1} \tag{A4}$$

Here, n_1 can be numerically calculated for GaN at longer wavelength (λ_1) by using the second order Sellmeier equation for the transparent medium.[189] Thereafter, the value of layer thickness (d) can be estimated by fitting the reflectivity spectra for the transparent region of GaN. Once, the values of λ_1, n_1, and d are known, the value of refractive index (n_p) can be estimated at any desired wavelength (λ_p) by using Eq. (A4).

APPENDIX B:

Numerical simulations for the temperature dependence of the refractive index of GaN

Let the m^{th} PL peak, which was earlier observed at λ_1, shifts to λ^I due to cooling. Let the value of the refractive index and layer thickness changes from n (d) to n^I (d^I) due to cooling (thermal contraction), respectively. Therefore, Equation (A1) of Appendix A for a given temperature T is modified as follows:

$$2n^I d^I = m\lambda^I \tag{B1}$$

After combining this with Eq. (A1), we have

$$n^I = \frac{\lambda^I}{\lambda_1}\frac{d}{d^I}n_1 \tag{B2}$$

The modified value of layer thickness (d^I) at temperature T can be calculated by using the thermal expansion coefficient of GaN. The values of λ_1, n_1, and d are already known from Appendix A, while the values of λ^I are measured from the temperature dependence

of the interference oscillations in reflectivity spectrum. Therefore, the value of n^{1} can be calculated by using Eq. (B2). Hence, the temperature dependence of refractive index of GaN at any wavelength can be numerically estimated by using Eq. (A4) and (B2).

APPENDIX C:

Numerical analysis for interference contrast in 2DEG PL

The laser beam excites electron-hole pairs in GaN channel layer adjacent to AlGaN/GaN interface since AlGaN barrier is transparent to the excitation laser source. Subsequently, the photo-excited electron-hole pairs decay via GaN excitonic, defect assisted and 2DEG recombination channels. Note that the energy of 2DEG PL feature is expected to be lower than the bandgap of GaN [134]. This makes the GaN channel layer transparent to photons generated via 2DEG related transitions. GaN channel layer therefore acts like a Fabry-Perot cavity for 2DEG PL signal where Air/AlGaN surface and GaN/Sapphire interface act as cavity mirror. Similar interference phenomenon can occur for defect related PL features and LO-phonon replica of band edge features within the cavity where the origin of PL is distributed along the depth of cavity. A systematic numerical analysis is carried out to distinguish the two cases, i.e. 1) PL signal is generated along the entire depth of GaN channel layer, and 2) PL signal is generated at a particular depth in the cavity.

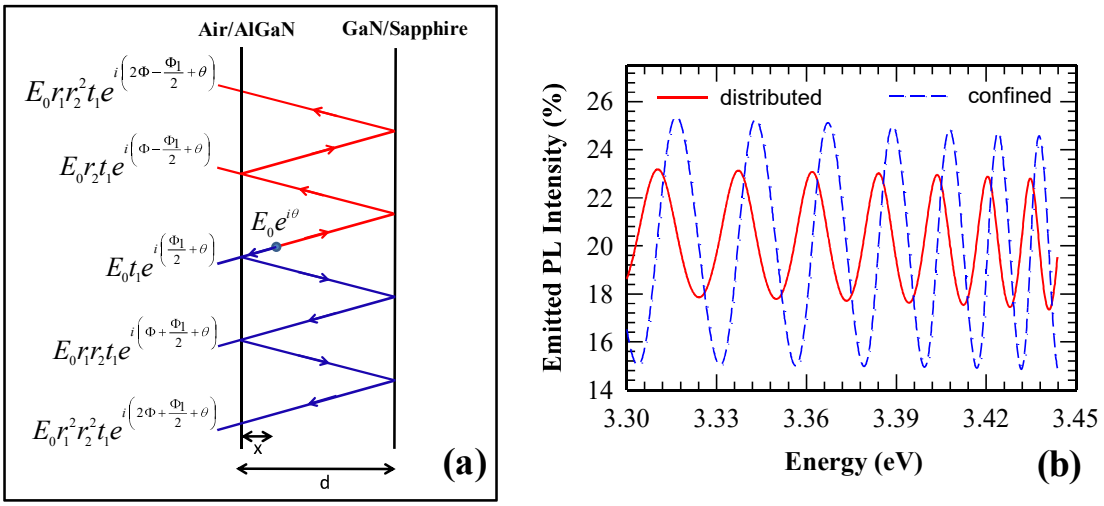

Figure A1 (a) Schematic ray diagram to illustrate the multiple reflections of PL signal within the F-P cavity, (b) Transmitted PL intensity versus energy for distributed (red) PL generation and confined (blue) PL generation along the depth of the sample.

Consider that the PL signal is generated at a distance 'x' μm from one of the F-P cavity mirrors with an initial phase θ as shown in Fig. A1 (a). One part of the PL signal travels in the forward direction (blue beam) while the another part travels in backward direction (red beam). The two components thereafter undergo multiple reflections within the cavity. A few components for the two beams are also shown in Fig. A1 (a). Let r_1 (t_1) and r_2 (t_2) be the reflection (transmission) coefficients of front and back mirror respectively and 'd' be the cavity length in μm. The phase difference introduced due to a complete round trip (2d) travel inside the cavity (for normal incidence) is given as follows,

$$\Phi = 2kd = \frac{4\pi\eta d}{\lambda} \qquad \text{(C1)}$$

where, k is the wave vector, η is the refractive index of GaN, λ is the wavelength of PL signal. Similarly, the phase introduced to traverse a path of 2x distance can be given as follows,

$$\Phi_1 = 2kx = \frac{4\pi\eta x}{\lambda} \tag{C2}$$

Note that the rays are shown to hit the interface at an angle in Fig. 1. It is only for clarity in viewing, we otherwise consider normal incidence since the PL signal is collected normal to the sample surface in our experimental geometry.

Amplitude of the emitted PL signal can be given as follows,

$$E_t = E_t^1 + E_t^2 \tag{C3}$$

where,

$$E_t^1 = E_0 r_2 t_1 e^{i\left(\Phi - \frac{\Phi_1}{2} + \theta\right)} + E_0 r_1 r_2^2 t_1 e^{i\left(2\Phi - \frac{\Phi_1}{2} + \theta\right)} + E_0 r_1^2 r_2^3 t_1 e^{i\left(3\Phi - \frac{\Phi_1}{2} + \theta\right)} + \cdots$$

$$= E_0 r_2 t_1 e^{i\left(\Phi - \frac{\Phi_1}{2} + \theta\right)} \left[1 + r_1 r_2 e^{i\Phi} + r_1^2 r_2^2 e^{i2\Phi} + \cdots\right]$$

$$= \frac{E_0 r_2 t_1 e^{i\left(\Phi - \frac{\Phi_1}{2} + \theta\right)}}{1 - r_1 r_2 e^{i\Phi}}$$

and

$$E_t^2 = E_0 t_1 e^{i\left(\frac{\Phi_1}{2} + \theta\right)} + E_0 r_1 r_2 t_1 e^{i\left(\Phi + \frac{\Phi_1}{2} + \theta\right)} + E_0 r_1^2 r_2^2 t_1 e^{i\left(2\Phi + \frac{\Phi_1}{2} + \theta\right)} + \cdots$$

$$= E_0 t_1 e^{i\left(\frac{\Phi_1}{2} + \theta\right)} \left[1 + r_1 r_2 e^{i\Phi} + r_1^2 r_2^2 e^{i2\Phi} + \cdots\right]$$

$$= \frac{E_0 t_1 e^{i\left(\frac{\Phi_1}{2} + \theta\right)}}{1 - r_1 r_2 e^{i\Phi}}$$

From equation-C3,

$$E_t = \frac{E_0 r_2 t_1 e^{i\left(\Phi - \frac{\Phi_1}{2} + \theta\right)}}{1 - r_1 r_2 e^{i\Phi}} + \frac{E_0 t_1 e^{i\left(\frac{\Phi_1}{2} + \theta\right)}}{1 - r_1 r_2 e^{i\Phi}}$$

$$= \frac{E_0 t_1 e^{i\left(\frac{\Phi_1}{2}+\theta\right)}}{1-r_1 r_2 e^{i\Phi}}\left(r_2 e^{i(\Phi-\Phi_1)}+1\right) \quad \text{(C4)}$$

Therefore, the transmitted intensity (I_t) of PL signal is given by,

$$I_t = |E_t|^2$$

$$= E_0^2 t_1^2 \frac{\left|r_2 e^{i(\Phi-\Phi_1)}+1\right|^2}{\left|1-r_1 r_2 e^{i\Phi}\right|^2}$$

$$= E_0^2 t_1^2 \frac{\{1+r_2^2+2r_2\cos(\Phi-\Phi_1)\}}{\{1+r_1^2 r_2^2-2r_1 r_2\cos\Phi\}} \quad \text{(C5)}$$

Here, experimentally reported values of reflection coefficients of Air/AlGaN (r1=0.41) and GaN/Sapphire (r2=0.20) are taken for the entire spectral range and absorption within the sample is neglected due to the sub-band energy of 2DEG PL. For simplicity, intensity of PL signal is taken to be constant at all wavelength, which is required to develop an understanding of interference oscillations. One can then convolute the interference oscillations with PL spectrum of Gaussian line shape to simulate the actual spectrum.

Case-1

PL is generated throughout the sample along the depth and intensity is also same along the depth. From equation-A5, transmitted intensity is a periodic function of Φ_1 with a period of 2π. If intensity is integrated over 2π, it will provide the line shape of resultant intensity along the sample depth.

From equation-C5, for spatially distributed photo-generation,

$$I_{t\_distributed} = E_0^2 t_1^2 \frac{\left\{2\pi(1+r_2^2)+2r_2\int_0^{2\pi}\cos(\Phi-\Phi_1)d\Phi_1\right\}}{\{1+r_1^2 r_2^2-2r_1 r_2\cos\Phi\}}$$

$$= E_0^2 t_1^2 \frac{2\pi(1+r_2^2)}{(1+r_1^2 r_2^2 - 2r_1 r_2 \cos\Phi)} \quad \text{(C6)}$$

The ratio of transmitted intensity to total photo-generated intensity ($I_0 = 8\pi E_0^2$) can be written as,

$$\frac{I_{t\_distributed}}{I_0} = \frac{1}{4}\frac{t_1^2(1+r_2^2)}{(1+r_1^2 r_2^2 - 2r_1 r_2 \cos\Phi)} \quad \text{(C7)}$$

Case-2

PL is generated at a particular depth inside the cavity. From equation-C5, for PL generation at a particular depth (taking Φ_1 ~ 25 nm),

$$I_{t\_fixed} = 2\pi E_0^2 t_1^2 \frac{(1+r_2^2+2r_2\cos(\Phi-\Phi_1))}{(1+r_1^2 r_2^2 - 2r_1 r_2 \cos\Phi)} \quad \text{(C8)}$$

The ratio of transmitted intensity to total photo-generated intensity can be written as

$$\frac{I_{t\_fixed}}{I_0} = \frac{1}{4}\frac{t_1^2(1+r_2^2+2r_2(\Phi-\Phi_1))}{(1+r_1^2 r_2^2 - 2r_1 r_2 \cos\Phi)} \quad \text{(C9)}$$

Enq. C7, and Eq. C9 are plotted as a function of energy $\left(E = \frac{1.24\Phi}{4\pi\eta d}\right)$ in Fig. A1(b). Here, it is found that the interference contrast is more in case of PL signal generation at a particular depth in the cavity when compared with the generation of PL signal which is distributed along the depth of entire channel layer. This unambiguously suggests that the 2DEG PL feature has a large probability to show interference phenomenon.

Bibliography

1. B. J. Baliga, Semiconductor Science and Technology **28** (7), 074011 (2013).
2. U. K. Mishra, L. Shen, T. E. Kazior and Y. F. Wu, Proceedings of the IEEE **96** (2), 287-305 (2008).
3. L. F. Eastman, V. Tilak, J. Smart, B. M. Green, E. M. Chumbes, R. Dimitrov, H. Kim, O. S. Ambacher, N. Weimann, T. Prunty, M. Murphy, W. J. Schaff and J. R. Shealy, Electron Devices, IEEE Transactions on **48** (3), 479-485 (2001).
4. S. Nakamura, Semiconductor Science and Technology **14** (6), R27 (1999).
5. M. S. Shur and M. A. Khan, MRS Bulletin **22** (02), 44-50 (1997).
6. M. Asif Khan, A. Bhattarai, J. Kuznia and D. Olson, Applied Physics Letters **63** (9), 1214-1215 (1993).
7. F. Ponce and D. Bour, Nature **386** (6623), 351 (1997).
8. S. Rajan, P. Waltereit, C. Poblenz, S. J. Heikman, D. S. Green, J. S. Speck and U. K. Mishra, IEEE Electron Device Letters **25** (5), 247-249 (2004).
9. J. M. Phillips, M. E. Coltrin, M. H. Crawford, A. J. Fischer, M. R. Krames, R. Mueller-Mach, G. O. Mueller, Y. Ohno, L. E. Rohwer and J. A. Simmons, Laser & Photonics Reviews **1** (4), 307-333 (2007).
10. J. Orton and C. Foxon, Reports on progress in physics **61** (1), 1 (1998).
11. S. Nakamura, T. Mukai and M. Senoh, Japanese Journal of Applied Physics **30** (12A), L1998 (1991).
12. K. Joshin, T. Kikkawa, S. Masuda and K. Watanabe, Fujitsu Sci. Tech. J **50** (1), 138-143 (2014).
13. R. S. Pengelly, S. M. Wood, J. W. Milligan, S. T. Sheppard and W. L. Pribble, IEEE Transactions on Microwave Theory and Techniques **60** (6), 1764-1783 (2012).
14. R. Dingle, H. L. Störmer, A. C. Gossard and W. Wiegmann, Applied Physics Letters **33** (7), 665-667 (1978).
15. S. Si, Oki Technical Review **174** (3), 90-93 (2007).

16. J. Millan, P. Godignon, X. Perpina, A. Pérez-Tomás and J. Rebollo, IEEE transactions on Power Electronics **29** (5), 2155-2163 (2014).
17. D. W. Runton, B. Trabert, J. B. Shealy and R. Vetury, IEEE Microwave Magazine **14** (3), 82-93 (2013).
18. M. A. Khan, J. Kuznia, J. Van Hove, N. Pan and J. Carter, Applied Physics Letters **60** (24), 3027-3029 (1992).
19. A. Bykhovski, B. Gelmont and M. Shur, Journal of Applied Physics **74** (11), 6734-6739 (1993).
20. Y.-F. Wu, B. Keller, S. Keller, D. Kapolnek, S. Denbaars and U. Mishra, IEEE Electron Device Letters **17** (9), 455-457 (1996).
21. M. Asif Khan, J. Kuznia, D. Olson, W. Schaff, J. Burm and M. Shur, Applied Physics Letters **65** (9), 1121-1123 (1994).
22. P. Klein, J. Freitas Jr, S. Binari and A. Wickenden, Applied Physics Letters **75** (25), 4016-4018 (1999).
23. P. Klein, S. Binari, K. Ikossi-Anastasiou, A. Wickenden, D. Koleske, R. Henry and D. Katzer, Electronics Letters **37** (10), 661-662 (2001).
24. S. C. Binari, P. Klein and T. E. Kazior, Proceedings of the IEEE **90** (6), 1048-1058 (2002).
25. B. M. Green, K. K. Chu, E. M. Chumbes, J. A. Smart, J. R. Shealy and L. F. Eastman, IEEE Electron Device Letters **21** (6), 268-270 (2000).
26. A. Vertiatchikh, L. Eastman, W. Schaff and T. Prunty, Electronics Letters **38** (8), 388-389 (2002).
27. A. Chini, D. Buttari, R. Coffie, S. Heikman, S. Keller and U. Mishra, Electronics Letters **40** (1), 73-74 (2004).
28. Y. Ando, Y. Okamoto, H. Miyamoto, T. Nakayama, T. Inoue and M. Kuzuhara, IEEE Electron Device Letters **24** (5), 289-291 (2003).
29. J. Lee, J. Kim, J. Lee, C. Kim, J. Oh and M. Shin, Electronics Letters **39** (9), 750-752 (2003).
30. T. Palacios, A. Chakraborty, S. Heikman, S. Keller, S. DenBaars and U. Mishra, IEEE Electron Device Letters **27** (1), 13-15 (2006).
31. M. Micovic, P. Hashimoto, M. Hu, I. Milosavljevic, J. Duvall, P. J. Willadsen, W.-S. Wong, A. M. Conway, A. Kurdoghlian and P. W. Deelman, presented at the

Electron Devices Meeting, 2004. IEDM Technical Digest. IEEE International, 2004 (unpublished).

32. F. Schubert, S. Wirth, F. Zimmermann, J. Heitmann, T. Mikolajick and S. Schmult, Science and technology of advanced materials **17** (1), 239-243 (2016).
33. S. W. Kaun, P. G. Burke, M. Hoi Wong, E. C. H. Kyle, U. K. Mishra and J. S. Speck, Applied Physics Letters **101** (26), 262102 (2012).
34. Y.-J. Lee, Y.-C. Yao, C.-Y. Huang, T.-Y. Lin, L.-L. Cheng, C.-Y. Liu, M.-T. Wang and J.-M. Hwang, Nanoscale Research Letters **9** (1), 433 (2014).
35. K. Kwangse, L. Kyeongjae, S. Byeongchan, H. Cheon, L. Kyungbae, K. Taemyung, H. Sang-Woo, C. Ho-Young and N. Okhyun, Japanese Journal of Applied Physics **56** (1), 015502 (2017).
36. Y. Cordier, M. Azize, N. Baron, Z. Bougrioua, S. Chenot, O. Tottereau, J. Massies and P. Gibart, Journal of Crystal Growth **310** (5), 948-954 (2008).
37. G. Simin, X. Hu, A. Tarakji, J. Zhang, A. Koudymov, S. Saygi, J. Yang, A. Khan, M. S. Shur and R. Gaska, Japanese Journal of Applied Physics **40** (11A), L1142 (2001).
38. T. Hubáček, A. Hospodková, J. Oswald, K. Kuldová and J. Pangrác, Journal of Crystal Growth **464**, 221-225 (2017).
39. M. Magnuson, M. Mattesini, C. Höglund, J. Birch and L. Hultman, Physical Review B **81** (8), 085125 (2010).
40. B. Singh, V. Baghel and K. Baghel, Indian Journal of Pure and Applied Physics **47** 793 (2009).
41. O. Ambacher, J. Smart, J. R. Shealy, N. G. Weimann, K. Chu, M. Murphy, W. J. Schaff, L. F. Eastman, R. Dimitrov, L. Wittmer, M. Stutzmann, W. Rieger and J. Hilsenbeck, Journal of Applied Physics **85** (6), 3222-3233 (1999).
42. F. Bernardini, V. Fiorentini and D. Vanderbilt, Physical Review B **56** (16), R10024 (1997).
43. I. Grzegory, M. Boćkowski, B. Łucznik, S. Krukowski, Z. Romanowski, M. Wroblewski and S. Porowski, Journal of crystal growth **246** (3), 177-186 (2002).
44. M. Stutzmann, O. Ambacher, M. Eickhoff, U. Karrer, A. Lima Pimenta, R. Neuberger, J. Schalwig, R. Dimitrov, P. Schuck and R. Grober, physica status solidi (b) **228** (2), 505-512 (2001).

45. B. Shen, T. Someya, O. Moriwaki and Y. Arakawa, Applied Physics Letters **76** (6), 679-681 (2000).
46. I. P. Smorchkova, L. Chen, T. Mates, L. Shen, S. Heikman, B. Moran, S. Keller, S. P. DenBaars, J. S. Speck and U. K. Mishra, Journal of Applied Physics **90** (10), 5196-5201 (2001).
47. E. S. Koteles and J. Chi, Superlattices and Microstructures **2** (5), 421-423 (1986).
48. R. Vetury, N. Q. Zhang, S. Keller and U. K. Mishra, IEEE Transactions on Electron Devices **48** (3), 560-566 (2001).
49. L. Gordon, M.-S. Miao, S. Chowdhury, M. Higashiwaki, U. K. Mishra and C. G. Van de Walle, Journal of Physics D: Applied Physics **43** (50), 505501 (2010).
50. B. Jogai, Journal of applied physics **93** (3), 1631-1635 (2003).
51. M. A. Khan, M. S. Shur, Q. Chen and J. Kuznia, Electronics Letters **30** (25), 2175-2176 (1994).
52. N. Braga, R. Mickevicius, R. Gaska, M. Shur, M. A. Khan and G. Simin, Applied physics letters **85** (20), 4780-4782 (2004).
53. A. M. Armstrong, A. A. Allerman, A. G. Baca and C. A. Sanchez, Semiconductor Science and Technology **28** (7), 074020 (2013).
54. G. Meneghesso, G. Verzellesi, R. Pierobon, F. Rampazzo, A. Chini, U. K. Mishra, C. Canali and E. Zanoni, IEEE Transactions on Electron Devices **51** (10), 1554-1561 (2004).
55. O. Mitrofanov and M. Manfra, Superlattices and Microstructures **34** (1), 33-53 (2003).
56. J. M. Tirado, J. L. Sanchez-Rojas and J. I. Izpura, IEEE Transactions on Electron Devices **54** (3), 410-417 (2007).
57. K. Gurnett and T. Adams, III-Vs Review **19** (9), 39-41 (2006).
58. S. Kukushkin, A. Osipov, V. Bessolov, B. Medvedev, V. Nevolin and K. Tcarik, Rev. Adv. Mater. Sci **17** (1/2), 1-32 (2008).
59. W. J. Moore, J. A. Freitas, G. C. B. Braga, R. J. Molnar, S. K. Lee, K. Y. Lee and I. J. Song, Applied Physics Letters **79** (16), 2570-2572 (2001).
60. C. Poblenz, P. Waltereit, S. Rajan, S. Heikman, U. Mishra and J. Speck, Journal of Vacuum Science & Technology B: Microelectronics and Nanometer Structures Processing, Measurement, and Phenomena **22** (3), 1145-1149 (2004).

61. L. Ravikiran, K. Radhakrishnan, S. Munawar Basha, N. Dharmarasu, M. Agrawal, C. Manoj kumar, S. Arulkumaran and G. Ng, Journal of Applied Physics **117** (24), 245305 (2015).
62. C. Seager, A. Wright, J. Yu and W. Götz, Journal of Applied Physics **92** (11), 6553-6560 (2002).
63. M. A. Reshchikov and H. Morkoç, Journal of Applied Physics **97** (6), 061301 (2005).
64. L. Kronik and Y. Shapira, Surface Science Reports **37** (1), 1-206 (1999).
65. I. Vurgaftman and J. n. Meyer, Journal of Applied Physics **94** (6), 3675-3696 (2003).
66. A. Shikanai, T. Azuhata, T. Sota, S. Chichibu, A. Kuramata, K. Horino and S. Nakamura, Journal of Applied Physics **81** (1), 417-424 (1997).
67. M. Fox, *Optical Properties of Solids*. (Oxford University Press, 2001).
68. A. K. Viswanath, E.-j. Shin, J. I. Lee, S. Yu, D. Kim, B. Kim, Y. Choi and C.-H. Hong, Journal of Applied Physics **83** (4), 2272-2275 (1998).
69. B. Monemar, P. P. Paskov, G. Pozina, C. Hemmingsson, J. P. Bergman, S. Khromov, V. N. Izyumskaya, V. Avrutin, X. Li, H. Morkoç, H. Amano, M. Iwaya and I. Akasaki, Journal of Applied Physics **115** (5), 053507 (2014).
70. E. Glaser, W. Carlos, G. Braga, J. Freitas Jr, W. Moore, B. Shanabrook, R. Henry, A. Wickenden, D. Koleske and H. Obloh, Physical Review B **65** (8), 085312 (2002).
71. F. Ponce, D. Bour, W. Götz and P. Wright, Applied Physics Letters **68** (1), 57-59 (1996).
72. T. Ogino and M. Aoki, Japanese Journal of Applied Physics **19** (12), 2395 (1980).
73. A. Armstrong, A. Chakraborty, J. Speck, S. DenBaars, U. Mishra and S. Ringel, Applied Physics Letters **89** (26), 262116 (2006).
74. D. Hofmann, D. Kovalev, G. Steude, B. Meyer, A. Hoffmann, L. Eckey, R. Heitz, T. Detchprom, H. Amano and I. Akasaki, Physical Review B **52** (23), 16702 (1995).
75. J. Lyons, A. Janotti and C. Van de Walle, Applied Physics Letters **97** (15), 152108 (2010).
76. M. Smith, G. Chen, J. Lin, H. Jiang, A. Salvador, B. Sverdlov, A. Botchkarev, H. Morkoc and B. Goldenberg, Applied physics letters **68** (14), 1883-1885 (1996).
77. M. A. Reshchikov, D. Demchenko, A. Usikov, H. Helava and Y. Makarov, Physical Review B **90** (23), 235203 (2014).

78. D. Demchenko, I. Diallo and M. Reshchikov, Physical Review Letters **110** (8), 087404 (2013).
79. S. G. Christenson, W. Xie, Y. Sun and S. Zhang, Journal of Applied Physics **118** (13), 135708 (2015).
80. M. Reshchikov, J. McNamara, F. Zhang, M. Monavarian, A. Usikov, H. Helava, Y. Makarov and H. Morkoç, Physical Review B **94** (3), 035201 (2016).
81. M. Julkarnain, T. Fukuda, N. Kamata and Y. Arakawa, Applied Physics Letters **107** (21), 212102 (2015).
82. T. S. Kang, Y.-H. Lin, S. Ahn, F. Ren, B. P. Gila, S. J. Pearton and D. J. Cheney, Journal of Vacuum Science & Technology B, Nanotechnology and Microelectronics: Materials, Processing, Measurement, and Phenomena **34** (1), 011203 (2016).
83. F. Kaess, P. Reddy, D. Alden, A. Klump, L. H. Hernandez-Balderrama, A. Franke, R. Kirste, A. Hoffmann, R. Collazo and Z. Sitar, Journal of Applied Physics **120** (23), 235705 (2016).
84. M. Matys and B. Adamowicz, Journal of Applied Physics **121** (6), 065104 (2017).
85. J. Neugebauer and C. G. Van de Walle, Applied Physics Letters **69** (4), 503-505 (1996).
86. K. Saarinen, T. Laine, S. Kuisma, J. Nissilä, P. Hautojärvi, L. Dobrzynski, J. Baranowski, K. Pakula, R. Stepniewski and M. Wojdak, MRS Online Proceedings Library Archive **482** (1997).
87. J. Elsner, R. Jones, M. Heggie, P. Sitch, M. Haugk, T. Frauenheim, S. Öberg and P. Briddon, Physical Review B **58** (19), 12571 (1998).
88. X. Li, P. Bohn and J. Coleman, Applied Physics Letters **75** (26), 4049-4051 (1999).
89. C. Soh, S. Chua, H. Lim, D. Chi, S. Tripathy and W. Liu, Journal of Applied Physics **96** (3), 1341-1347 (2004).
90. A. Hoffmann, L. Eckey, P. Maxim, J.-C. Holst, R. Heitz, D. Hofmann, D. Kovalev, G. Stevde, D. Volm and B. Meyer, Solid-State Electronics **41** (2), 275-278 (1997).
91. W. Götz, N. Johnson, R. Street, H. Amano and I. Akasaki, Applied Physics Letters **66** (11), 1340-1342 (1995).
92. C. G. Van de Walle, C. Stampfl and J. Neugebauer, Journal of Crystal Growth **189**, 505-510 (1998).

93. M. Huber, M. Silvestri, L. Knuuttila, G. Pozzovivo, A. Andreev, A. Kadashchuk, A. Bonanni and A. Lundskog, Applied Physics Letters **107** (3), 032106 (2015).
94. I. Shalish, L. Kronik, G. Segal, Y. Rosenwaks, Y. Shapira, U. Tisch and J. Salzman, Physical Review B **59** (15), 9748 (1999).
95. M. Reshchikov, M. Foussekis and A. Baski, Journal of Applied Physics **107** (11), 113535 (2010).
96. M. Foussekis, J. Ferguson, A. Baski, H. Morkoc and M. Reshchikov, Physica B: Condensed Matter **404** (23), 4892-4895 (2009).
97. M. Foussekis, A. Baski and M. Reshchikov, Journal of Vacuum Science & Technology B, Nanotechnology and Microelectronics: Materials, Processing, Measurement, and Phenomena **29** (4), 041205 (2011).
98. J. D. McNamara, M. Foussekis, A. A. Baski and M. A. Reshchikov, Journal of Vacuum Science & Technology B, Nanotechnology and Microelectronics: Materials, Processing, Measurement, and Phenomena **32** (1), 011209 (2014).
99. J. McNamara, K. Phumisithikul, A. Baski, J. Marini, F. Shahedipour-Sandvik, S. Das and M. Reshchikov, Journal of Applied Physics **120** (15), 155304 (2016).
100. M. Godlewski, E. Goldys, M. Phillips, R. Langer and A. Barski, Applied Physics Letters **73** (25), 3686-3688 (1998).
101. X. Li and J. Coleman, Applied Physics Letters **70** (4), 438-440 (1997).
102. C. Trager-Cowan, K. O'Donnell, S. Hooper and C. Foxon, Applied Physics Letters **68** (3), 355-357 (1996).
103. X. Qiu, Y. Segawa, Q. Xue, Q. Xue and T. Sakurai, Applied Physics Letters **77** (9), 1316-1318 (2000).
104. L. Macht, J. Weyher, A. Grzegorczyk and P. Larsen, Physical Review B **71** (7), 073309 (2005).
105. C. Lee, J.-E. Kim, H. Y. Park, S. Kim and H. Lim, Journal of Physics: Condensed Matter **10** (48), 11103 (1998).
106. E. Oh, H. Park and Y. Park, Applied Physics Letters **72** (1), 70-72 (1998).
107. J. Myoung, K. Shim, C. Kim, O. Gluschenkov, K. Kim, S. Kim, D. Turnbull and S. Bishop, Applied Physics Letters **69** (18), 2722-2724 (1996).
108. J.-K. Sheu, Y.-K. Su, G. Chi, B. Pong, C. Chen, C. Huang and W. Chen, Journal of Applied Physics **84** (8), 4590-4594 (1998).

109. F. Shahedipour and B. Wessels, Applied Physics Letters **76** (21), 3011-3013 (2000).
110. T. Jeong, C. Youn, M. Han, J. Yang and K. Lim, Journal of crystal growth **259** (3), 267-272 (2003).
111. J. L. Lyons, A. Janotti and C. G. Van de Walle, Physical Review Letters **108** (15), 156403 (2012).
112. G. Callsen, M. Wagner, T. Kure, J. Reparaz, M. Bügler, J. Brunnmeier, C. Nenstiel, A. Hoffmann, M. Hoffmann and J. Tweedie, Physical Review B **86** (7), 075207 (2012).
113. G. Namkoong, E. Trybus, K. K. Lee, M. Moseley, W. A. Doolittle and D. C. Look, Applied Physics Letters **93** (17), 172112 (2008).
114. S. Brochen, J. Brault, S. Chenot, A. Dussaigne, M. Leroux and B. Damilano, Applied Physics Letters **103** (3), 032102 (2013).
115. B. P. Gunning, C. A. Fabien, J. J. Merola, E. A. Clinton, W. A. Doolittle, S. Wang, A. M. Fischer and F. A. Ponce, Journal of Applied Physics **117** (4), 045710 (2015).
116. Z. Liu, X. Yi, Z. Yu, G. Yuan, Y. Liu, J. Wang, J. Li, N. Lu, I. Ferguson and Y. Zhang, Scientific Reports **6** (2016).
117. H. Okumura, D. Martin, M. Malinverni and N. Grandjean, Applied Physics Letters **108** (7), 072102 (2016).
118. P. Kozodoy, H. Xing, S. P. DenBaars, U. K. Mishra, A. Saxler, R. Perrin, S. Elhamri and W. Mitchel, Journal of Applied Physics **87** (4), 1832-1835 (2000).
119. H. Obloh, K. Bachem, U. Kaufmann, M. Kunzer, M. Maier, A. Ramakrishnan and P. Schlotter, Journal of Crystal Growth **195** (1), 270-273 (1998).
120. S. Nakamura, N. Iwasa, M. Senoh and T. Mukai, Japanese Journal of Applied Physics **31** (5R), 1258 (1992).
121. G. Miceli and A. Pasquarello, Physical Review B **93** (16), 165207 (2016).
122. Y.-H. Kwon, S. Shee, G. Gainer, G. Park, S. Hwang and J. Song, Applied Physics Letters **76** (7), 840-842 (2000).
123. L. Eckey, U. Von Gfug, J. Holst, A. Hoffmann, A. Kaschner, H. Siegle, C. Thomsen, B. Schineller, K. Heime and M. Heuken, Journal of Applied Physics **84** (10), 5828-5830 (1998).
124. M. Reshchikov, G.-C. Yi and B. Wessels, Physical Review B **59** (20), 13176 (1999).
125. C. Park and D. Chadi, Physical Review B **55** (19), 12995 (1997).

126. R. Kirste, M. P. Hoffmann, J. Tweedie, Z. Bryan, G. Callsen, T. Kure, C. Nenstiel, M. R. Wagner, R. Collazo and A. Hoffmann, Journal of Applied Physics **113** (10), 103504 (2013).
127. J. Buckeridge, C. R. A. Catlow, D. Scanlon, T. Keal, P. Sherwood, M. Miskufova, A. Walsh, S. Woodley and A. Sokol, Physical Review Letters **114** (1), 016405 (2015).
128. U. Wahl, L. Amorim, V. Augustyns, A. Costa, E. David-Bosne, T. Lima, G. Lippertz, J. Correia, M. da Silva and M. Kappers, Physical Review Letters **118** (9), 095501 (2017).
129. D. Cavalcoli and A. Cavallini, Physica Status Solidi (c) **7** (5), 1293-1300 (2010).
130. H.-S. Kwack, Y.-H. Cho, G. H. Kim, M. R. Park, D. H. Youn, S. B. Bae, K.-S. Lee, J.-H. Lee, J.-H. Lee, T. W. Kim, T. W. Kang and K. L. Wang, Applied Physics Letters **87** (4), 041909 (2005).
131. Z. Zheng, B. Shen, R. Zhang, Y. Gui, C. Jiang, Z. Ma, G. Zheng, S. Guo, Y. Shi, P. Han, Y. Zheng, T. Someya and Y. Arakawa, Physical Review B **62** (12), R7739-R7742 (2000).
132. N. Biyikli, X. Ni, Y. Fu, J. Xie, H. Morkoç, H. Cheng, Ç. Kurdak, I. Vurgaftman and J. Meyer, Journal of Applied Physics **101** (11), 113710 (2007).
133. J. P. Bergman, T. Lundström, B. Monemar, H. Amano and I. Akasaki, Applied Physics Letters **69** (23), 3456-3458 (1996).
134. G. Martínez-Criado, C. Miskys, U. Karrer, O. Ambacher and M. Stutzmann, Japanese Journal of Applied Physics **43** (6R), 3360 (2004).
135. C. Y. Fang, C. F. Lin, E. Y. Chang and M. S. Feng, Applied Physics Letters **80** (24), 4558-4560 (2002).
136. K. B. Nam, J. Li, M. L. Nakarmi, J. Y. Lin and H. X. Jiang, Applied Physics Letters **81** (10), 1809-1811 (2002).
137. T. Wang, J. Bai and S. Sakai, Physical Review B **63** (20), 205320 (2001).
138. H. K. Kwon, C. J. Eiting, D. J. H. Lambert, B. S. Shelton, M. M. Wong, T. G. Zhu and R. D. Dupuis, Journal of Crystal Growth **221** (1–4), 362-367 (2000).
139. R. M. Chu, Y. G. Zhou, Y. D. Zheng, P. Han, B. Shen and S. L. Gu, Applied Physics Letters **79** (14), 2270-2272 (2001).
140. J. I. Pankove, *Optical processes in semiconductors*. (Courier Corporation, 2012).

141. J. Singh, *Electronic and optoelectronic properties of semiconductor structures*. (Cambridge University Press, 2007).
142. W. Shan, R. Hauenstein, A. Fischer, J. Song, W. Perry, M. Bremser, R. Davis and B. Goldenberg, Physical Review B **54** (19), 13460 (1996).
143. B. Monemar, Physical Review B **10** (2), 676 (1974).
144. T. K. Sharma, S. D. Singh, S. Porwal and A. K. Nath, Journal of Crystal Growth **298**, 527-530 (2007).
145. D. Cavalcoli, S. Pandey, B. Fraboni and A. Cavallini, Applied Physics Letters **98** (14), 142111 (2011).
146. S. Pandey, D. Cavalcoli, A. Minj, B. Fraboni, A. Cavallini, P. Gamarra and M. Poisson, Journal of Applied Physics **112** (12), 123721 (2012).
147. S. Pandey, D. Cavalcoli and A. Cavallini, Applied Physics Letters **102** (14), 142101 (2013).
148. A. Minj, D. Skuridina, D. Cavalcoli, A. Cros, P. Vogt, M. Kneissl, C. Giesen and M. Heuken, Materials Science in Semiconductor Processing **55**, 26-31 (2016).
149. S. Datta, S. Ghosh and B. Arora, Review of Scientific Instruments **72** (1), 177-183 (2001).
150. G. Vashisht, V. Dixit, S. Porwal, R. Kumar, T. Sharma and S. Oak, Journal of Applied Physics **119** (9), 095708 (2016).
151. S. Singh, S. Porwal, T. Sharma and S. Oak, Journal of Applied Physics **112** (9), 093505 (2012).
152. T. Sharma, S. Kumar and K. Rustagi, Journal of Applied Physics **92** (10), 5959-5965 (2002).
153. P. Blood, Journal of Applied Physics **58** (6), 2288-2295 (1985).
154. D. Sell and H. Casey Jr, Journal of Applied Physics **45** (2), 800-807 (1974).
155. D. Cavalcoli, B. Fraboni and A. Cavallini, Journal of Applied Physics **103** (4), 043713 (2008).
156. Q. Liu, C. Chen and H. Ruda, Journal of applied physics **74** (12), 7492-7496 (1993).
157. T. Sharma, S. Porwal, R. Kumar and S. Kumar, Review of Scientific Instruments **73** (4), 1835-1840 (2002).
158. H. Casey Jr, D. Sell and K. Wecht, Journal of Applied Physics **46** (1), 250-257 (1975).

159. S. Pal, A. Ingale, V. Dixit, T. Sharma, S. Porwal, P. Tiwari and A. Nath, Journal of Applied Physics **101** (4), 044311 (2007).
160. M. Grundmann, see http://my.ece.ucsb.edu/mgrundmann/bandeng.htm for a self-consistent solution of Schrödinger-Poisson equations.
161. Y. Nakano, Y. Irokawa, Y. Sumida, S. Yagi and H. Kawai, Journal of Applied Physics **112** (10), 106103 (2012).
162. S. Nakamura, Science **281** (5379), 956-961 (1998).
163. P. Klein and S. Binari, Journal of Physics: Condensed Matter **15** (44), R1641 (2003).
164. A. Armstrong, A. Arehart, D. Green, U. Mishra, J. Speck and S. Ringel, Journal of Applied Physics **98** (5), 053704 (2005).
165. J. Neugebauer and C. G. Van de Walle, Physical Review B **50** (11), 8067 (1994).
166. P. Bogusl, E. Briggs and J. Bernholc, Physical Review B **51** (23), 17255 (1995).
167. D. Jana, S. Porwal, A. Jain, S. Oak and T. Sharma, Journal of Applied Physics **118** (16), 164502 (2015).
168. D. Jana and T. Sharma, Journal of Applied Physics **122** (3), 035101 (2017).
169. D. Bimberg, M. Sondergeld and E. Grobe, Physical Review B **4** (10), 3451 (1971).
170. T. Lu, Z. Ma, C. Du, Y. Fang, H. Wu, Y. Jiang, L. Wang, L. Dai, H. Jia and W. Liu, Scientific Reports **4**, 6131 (2014).
171. V. Donchev, K. Kirilov, T. Ivanov and K. Germanova, Materials Science and Engineering: B **129** (1), 186-192 (2006).
172. A. Armstrong, J. Caudill, A. Corrion, C. Poblenz, U. Mishra, J. Speck and S. Ringel, Journal of Applied Physics **103** (6), 063722 (2008).
173. A. Billeb, W. Grieshaber, D. Stocker, E. F. Schubert and R. F. Karlicek, Applied Physics Letters **70** (21), 2790-2792 (1997).
174. Q. Zhang, D. Wang, X. Wei, T. Xie, Z. Li, Y. Lin and M. Yang, Thin Solid Films **491** (1), 242-248 (2005).
175. D. Jana and T. Sharma, Journal of Physics D: Applied Physics **49** (26), 265107 (2016).
176. M. Gladysiewicz, L. Janicki, J. Misiewicz, M. Sobanska, K. Klosek, Z. Zytkiewicz and R. Kudrawiec, Journal of Physics D: Applied Physics **49** (34), 345106 (2016).
177. D. Jana, S. Porwal, T. Sharma, S. Kumar and S. Oak, Review of Scientific Instruments **85** (4), 043909 (2014).

178. R. Kudrawiec, M. Syperek, J. Misiewicz, M. Rudziński, A. Grezegorczyk, P. Hageman and P. Larsen, Applied Physics Letters **87** (15), 153502 (2005).
179. N. Killat, M. Uren, D. Wallis, T. Martin and M. Kuball, Applied Physics Letters **101** (15), 153505 (2012).
180. T. Wang, Y. Ohno, M. Lachab, D. Nakagawa, T. Shirahama, S. Sakai and H. Ohno, Applied Physics Letters **74** (23), 3531-3533 (1999).
181. K.-W. Kim, D.-S. Kim, K.-S. Im, J.-H. Lee, B.-J. Kwon, H.-S. Kwack, S. Beck and Y.-H. Cho, Applied Physics Letters **98** (14), 141917 (2011).
182. A. E. Belyaev, A. V. Naumov, G. G. Tarasov, A. V. Komarov, M. Tacano, S. V. Danylyuk and S. A. Vitusevich, Journal of Applied Physics **101** (3), 033709 (2007).
183. M. Leroux, B. Beaumont, N. Grandjean, P. Lorenzini, S. Haffouz, P. Vennéguès, J. Massies and P. Gibart, Materials Science and Engineering: B **50** (1–3), 97-104 (1997).
184. A. K. Viswanath, J. I. Lee, D. Kim, C. R. Lee and J. Y. Leem, Physical Review B **58** (24), 16333-16339 (1998).
185. S. Chichibu, H. Okumura, S. Nakamura, G. Feuillet, T. Azuhata, T. Sota and S. Yoshida, Japanese Journal of applied physics **36** (3S), 1976 (1997).
186. M. Gladysiewicz, L. Janicki, R. Kudrawiec, J. Misiewicz, M. Wosko, R. Paszkiewicz, B. Paszkiewicz and M. Tłaczała, Journal of Applied Physics **115** (13), 133504 (2014).
187. K. Korona, A. Wysmol/ek, K. Pakul/a, R. Stepniewski, J. Baranowski, I. Grzegory, B. L/ucznik, M. Wroblewski and S. Porowski, Applied Physics Letters **69** (6), 788-790 (1996).
188. A. S. Barker and M. Ilegems, Physical Review B **7** (2), 743-750 (1973).
189. C. Prall, M. Ruebesam, C. Weber, M. Reufer and D. Rueter, Journal of Crystal Growth **397** (0), 24-28 (2014).
190. N. Antoine-Vincent, F. Natali, M. Mihailovic, P. Disseix, A. Vasson, J. Leymarie, D. Byrne, F. Semond and J. Massies, Physica Status Solidi (a) **195** (3), 543-550 (2003).
191. N. A. Sanford, L. H. Robins, A. V. Davydov, A. Shapiro, D. V. Tsvetkov, A. V. Dmitriev, S. Keller, U. K. Mishra and S. P. DenBaars, Journal of Applied Physics **94** (5), 2980-2991 (2003).

192. H.-S. Kwack, Y.-H. Cho, G. Kim, M. Park, D. Youn, S. Bae, K.-S. Lee, J.-H. Lee, J.-H. Lee and T. Kim, Applied Physics Letters **87** (4), 041909 (2005).
193. N. Akopian, A. Vardi, G. Bahir, V. Garber, E. Ehrenfreund, D. Gershoni, C. Poblenz, C. R. Elsass, I. P. Smorchkova and J. S. Speck, Applied Physics Letters **94** (22), 223502 (2009).
194. J.-P. Zhang, D.-Z. Sun, X.-L. Wang, M.-Y. Kong, Y.-P. Zeng, J.-M. Li and L.-Y. Lin, Applied physics letters **73** (17), 2471-2472 (1998).
195. C. Wood and D. Jena, *Polarization effects in semiconductors: from ab initio theory to device applications*. (Springer Science & Business Media, 2007).
196. Y. Fang, L. Wang, Q. Sun, T. Lu, Z. Deng, Z. Ma, Y. Jiang, H. Jia, W. Wang and J. Zhou, Scientific Reports **5** (2015).
197. I. Smorchkova, C. Elsass, J. Ibbetson, R. Vetury, B. Heying, P. Fini, E. Haus, S. DenBaars, J. Speck and U. Mishra, Journal of Applied Physics **86** (8), 4520-4526 (1999).
198. N. B. Sedrine, T. Esteves, J. Rodrigues, L. Rino, M. Correia, M. Sequeira, A. Neves, E. Alves, M. Bockowski and P. Edwards, Scientific Reports **5** (2015).
199. I. Kukushkin, K. v. Klitzing and K. Ploog, Physical Review B **37** (14), 8509 (1988).
200. Y. Yuan, M. Pudensi, G. Vawter and J. Merz, Journal of Applied Physics **58** (1), 397-403 (1985).
201. M. Ciorga, M. Kubisa, K. Ryczko, L. Bryja, J. Misiewicz and O. Hansen, Microelectronic Engineering **51**, 235-240 (2000).
202. D. Reynolds, D. C. Look, B. Jogai, P. W. Yu, K. Evans, C. Stutz and L. Radomsky, Physical Review B **50** (11), 7461 (1994).
203. G. Gilliland, D. Wolford, T. Kuech and J. Bradley, Physical Review B **49** (12), 8113 (1994).
204. W. Chen, M. Fritze, A. Nurmikko, M. Hong and L. Chang, Physical Review B **43** (18), 14738 (1991).
205. Q. Zhao, P. Holtz, B. Monemar, E. Sörman, W. Chen, C. Hallin, M. Sundaram, J. Merz and A. Gossard, Physical Review B **46** (7), 4352 (1992).
206. J. Fouquet and A. Siegman, Applied Physics Letters **46** (3), 280-282 (1985).

207. J. Tignon, O. Heller, P. Roussignol, J. Martinez-Pastor, P. Lelong, G. Bastard, R. C. Iotti, L. Andreani, V. Thierry-Mieg and R. Planel, Physical Review B **58** (11), 7076 (1998).
208. N. Mott, Philosophical Magazine **6** (62), 287-309 (1961).
209. T. Nagai, T. J. Inagaki and Y. Kanemitsu, Applied Physics Letters **84** (8), 1284-1286 (2004).
210. H. Reinholz, Solid State Communications **123** (11), 489-494 (2002).
211. W. Hu, X. Chen, F. Yin, J. Zhang and W. Lu, Journal of Applied Physics **105** (8), 084502 (2009).
212. S. W. Kaun, M. H. Wong, U. K. Mishra and J. S. Speck, Applied Physics Letters **100** (26), 262102 (2012).
213. S. Hashimoto, Y. Yoshizumi, T. Tanabe and M. Kiyama, Journal of Crystal Growth **298**, 871-874 (2007).
214. J. Ran, X. Wang, G. Hu, J. Wang, J. Li, C. Wang, Y. Zeng and J. Li, Microelectronics Journal **37** (7), 583-585 (2006).